

Deciphering the molecular events leading to the global  
restoration of the chromatin landscape during mitotic exit

Présentée le 3 novembre 2023

Faculté des sciences de la vie  
Unité du Prof. Suter  
Programme doctoral en approches moléculaires du vivant

pour l'obtention du grade de Docteur ès Sciences

par

**Silja Michelle PLACZEK**

Acceptée sur proposition du jury

Prof. J. Lingner, président du jury  
Prof. D. M. Suter, directeur de thèse  
Prof. N. Vastenhouw, rapporteuse  
Prof. M. Lagha, rapporteuse  
Prof. B. Deplancke, rapporteur

# Acknowledgements

The journey is itself the destination. I went through many ups and downs during my PhD, which helped me to become the person I am today. I had the great opportunity to meet many people who changed me as a scientist and friend.

First of all, I am very grateful for the support of my PhD supervisor David Suter. Although we had a rough start, I could not imagine a better PI in the end, and without him, I would not have become the thoughtful scientist I am today. I am very grateful for my colleague Ludovica Vanzan, who always supported me with scientific advice and her friendship. Although we could not be more different in what we like or dislike, you were my pillar throughout several years, and it made my day when I saw you in the lab. I also want to thank Michael (Shoujie) Sun and Cédric Deluz, who were in the lab with me from the beginning, and I spent several good years with them. Moreover, I would like to thank the current members of the Suter lab: Almut Eisele, Armelle Tollenaere, Benjamin Martin, Joanna Dembska, Romane Mizeret, Sim Sakong, and Stella Krämer. I also thank Christine Skaletzka and Laura Bischoff for organizing my start and departure and everything in between of my PhD. I want to thank former Suter lab member Elias Friman who I always looked up to since I started in the lab, and every time we see each other, it is a pleasure to catch up. I would also like to thank Alexandre Mayran and Chase Bolt for their kind support during the first year of my PhD when I tried to set up CUT&RUN.

I am grateful for the critical reading and evaluation of my PhD by my jury members Bart Deplancke, Mounia Lagha, Nadine Vastenhouw, and Joachim Lingner. Furthermore, I like to thank my mentor Micki De Palma, and the members of my candidacy jury Viesturs Simanis, Jean-Yves Roignant, and Bart Deplancke allowing me to resume my PhD and helping me push my intellect to a definitely needed level.

During my PhD journey, I had the opportunity to meet many companions at EPFL, and I apologize to those that I am not mentioning in this paragraph. I still like you! First of all, I would like to thank Alex Lederer, Umair Anwar, Rita Sarkis, and Aspasia Gkasti. Right from the hiring days, you were my main connection, and without you, my PhD would not have been as good. Alex and Umair, you are amazing people, and our coffee breaks, game nights, dinners, and lunches were the highlight on some days. You were there to cheer me up if things did not go well in the lab and one of the first people I want to share if great things happened. Rita, you are the most enthusiastic person I know, and I was delighted to share the wakeboard experience, visit your country, hear about the craziest stories, and cheer each other up. Aspasia, whenever we met, it was memorable. I am very grateful to my Chai buddy Divyanshu Srivastava for all the great memories we collected in the last years, from hiking to Via Ferrata,

from Chai to the shooting star night, and our great conversions. I would also like to thank Ilia Igashov for his support and friendship.

Not only EPFL has great people, but also UNIL. First of all, I would like to thank my bouldering buddy Lennard Wendlinger for his patience during the climbing, his kindness, sometimes funny jokes, support, and for introducing me to a strange way of eating Weißwurst. I would also like to thank my eternal Schafkopf buddy Leon Potgeter for many enjoyable times like hiking, card games, and founding our “band”. I also thank Calvin Nugraha for his amazing stories, kindness, and the “band”.

Before starting my PhD, I found an amazing group of friends in Tübingen. I am sad that we mostly went in different ways, but it makes me grateful that we are still in touch. The first person I met in Tübingen, and I want to thank is Gabriel Germann. You are one of the most amazing people I have met throughout my life. I am very thankful to have met you, for all the long and funny evenings we spent together and our meet-up in Japan. One of my biggest motivations to obtain a good master's degree was Leon Kleemann. I want to thank you for our playful competitions, your support, and the many good hours we spent together. I would also like to thank my westside buddy Johanna Geiger and my Mandelto buddy Sinja Kieninger for your kindness, support, hospitality, and great evenings. I want to thank Alberto Moreno and Przemysław Olejnik for their support and all the funny days. I have never laughed as much in my life as with them.

I also want to thank Lucas Jamar for being supportive during my PhD and enabling me to travel to many places.

Moreover, I want to thank my potentially longest group of friends. It is always a pleasure to meet up with you in Biberach, and it feels like time has stopped (in a good way). First of all, I would like to thank one of my biggest supporters over the last 13 years, my best friend Jonatan Kramer. You are an amazing person, and I still have a lot to learn from you. I want to thank you for all the hours you listened to my complaints, my happiness, and all my moods, you always helped me to get back up on my legs, all the great moments at McDonalds, and so many other things. There are no words that could describe my gratefulness to you. Moreover, I want to thank Mathias Kersten who I spent many great hours with. Thank you for your support, for always cheering me up, great dinners and evenings. I also want to thank Oliver Remke for his friendship, we had amazing moments together that will always stay in my mind, ratatatata...

Some of my most recent friends are also the ones that went through one of the bumpiest phases with me. Your support was my biggest pillar, and I hope that I can give you back at least a bit of the support that you gave me. You are very dear to my heart, like family. I would like to thank Ahmad ElRouby, Cátia Pereira, Dixit Sabharwal, and Ilja Shapiro. I do not know where to start thanking Ruby. You are my rock, my foundation. I want to thank you for

everything. Your boundless support, your amazing stories, the funniest and most profound talks we had, the dinners, all the memories, your kindness, honesty, just everything. No words can describe how grateful I am to have met you, and I hope I can be as good a friend as you are to me one day. Cátia, you are maybe the strongest person I know, and I want to thank you for your huge support, amazing evenings together, your care, the best dinner parties, and so many other things. Dixit and Ilja, I want to thank you for your support, calmness, and our great evenings. I hope one day I will reach your level of relaxation. You are amazing.

Moreover, I like to thank my family. I am grateful for my grandmother Eleonora Placzek, who keeps telling me that there is always hope if I am having a bad day. I want to thank you for always being there for me, supporting me throughout my whole life, and cheering me up whenever I was sad. I want to thank my parents Gisela and Herbert Placzek, who were very understanding and supportive when I needed it, for helping me achieve my goals and offering me a place to hide from the world. Last but not least, I want to thank my sister Desirée Placzek and her fiancé Tobias Esswein for the good times we spent together.

# Abstract

Two fundamental properties of embryonic stem cells (ESCs) are their ability to self-renew and differentiate into all somatic cell types. Maintenance of their identity faces major challenges when transitioning through mitosis, as most DNA-binding proteins are evicted from the DNA, enhancer-promoter connections are lost, and transcription is considerably reduced. It is unclear how ESCs maintain their cell identity and faithfully re-initiate pluripotent gene expression during mitotic exit. Previous studies on synchronized mitotic cells suggested that enhancer loops are reformed and gene expression is re-initiated during anaphase-telophase. Moreover, a specific ordering of transcription factor (TF) binding was proposed to take place after mitotic exit, but thus far, it has not been studied without the application of synthetic drugs. This thesis aims at studying the sequence of events leading to the global restoration of the chromatin landscape during mitotic exit in mouse ESCs using a cell cycle synchronization-free approach. We engineered a novel reporter cell line combining the oscillatory fluorescence of two cell cycle reporters to allow for precise separation of different temporal windows during mitotic exit. This cell line allows sorting mouse ESCs into an anaphase-telophase-enriched population and four temporal bins of early G1 separated by less than 30 minutes. We then used quantitative ChIP-seq to determine the sequential binding changes of OCT4, SOX2, and NANOG (OSN), ATAC-seq to quantify chromatin accessibility changes, and nuclear RNA-seq to quantify transcriptional reactivation in these temporal windows. We found that most genes involved in basic cellular processes and pluripotency were already highly expressed very early after mitotic exit, while genes involved in cell fate commitment were less expressed and likely regulated through transcriptional and post-transcriptional mechanisms. Moreover, we demonstrate that OSN does not bind to mitotic chromatin, re-binding is initiated in anaphase-telophase and completely restored at most regulatory regions within 40 minutes after cytokinesis. However, OSN exhibit distinct quantitative binding changes that differ in their dependency on chromatin accessibility. Although NANOG can bind to inaccessible chromatin at loci poorly enriched for OS, we found that OS directs NANOG binding genome-wide during mitotic exit. On the other hand, NANOG stabilizes OS binding. Interestingly, during the transition from naïve pluripotent stem cells to a more advanced developmental stage, the interaction between OCT4 and SN becomes more decisive to maintain the pluripotent regulatory landscape. Overall, our study suggests that OSN dynamically regulates genome reactivation during mitotic exit, and it emphasizes the importance of using unperturbed cells to study the sequential molecular changes occurring on chromatin during mitotic exit.

## Keywords

Mitotic exit, mouse embryonic stem cells, genome reactivation, transcription factor re-binding, restoration of chromatin accessibility, transcriptional reactivation, pioneer TFs, interaction, cell synchronization

## Résumé

Deux propriétés fondamentales des cellules souches embryonnaires (CSE) sont leur capacité à s'auto-renouveler et à se différencier en tous les types de cellules somatiques. Le maintien de leur identité est confronté à des défis majeurs lors du passage à la mitose, car la plupart des protéines de liaison à l'ADN sont expulsées de l'ADN, les connexions des promoteurs aux enhancers sont perdues et la transcription est considérablement réduite. La manière dont les CSE conservent leur identité cellulaire et réinitialisent fidèlement l'expression des gènes pluripotents pendant la sortie de la mitose n'est pas claire. Des études antérieures sur des cellules mitotiques synchronisées ont suggéré que les connexions des enhancers avec les promoteurs sont reformées et que l'expression des gènes est réinitialisée lors de la transition anaphase-télophase. De plus, il a été proposé qu'il existe un ordre spécifique de liaison des facteurs de transcription (TF), mais jusqu'à présent, cela n'a pas été étudié sans l'application de médicaments synthétiques.

Par conséquent, cette thèse vise à étudier la séquence d'événements menant à la restauration globale du paysage chromatinien pendant la sortie mitotique dans les CSE de souris, dans un système non perturbé. Nous avons utilisé une nouvelle lignée de cellules rapporteuses combinant la fluorescence oscillatoire de deux rapporteurs publiés, permettant une discrimination précise de différentes fenêtres temporelles lors de la sortie mitotique. Elle permet de trier les CSE de souris en une population enrichie en anaphase et en télophase et en quatre tranches temporelles de la partie précoce de la phase G1, séparées par moins de 30 minutes. Nous avons utilisé l'immunoprécipitation de la chromatine suivie de séquençage (ChIP-seq) pour quantifier les changements de liaison séquentielle entre OCT4, SOX2 et NANOG (OSN), la technique ATAC-seq pour étudier les changements d'accessibilité à la chromatine et le séquençage d'ARN nucléaires pour quantifier la réactivation transcriptionnelle. Nous avons constaté que la plupart des gènes impliqués dans les processus cellulaires de base et la pluripotence étaient déjà fortement exprimés dans les 40 minutes après cytokinèse, tandis que les gènes impliqués dans l'engagement du destin cellulaire étaient moins exprimés et probablement régulés par des mécanismes transcriptionnels et post-transcriptionnels. De plus, nous avons démontré que OSN ne se lient pas à la chromatine mitotique, que leur re-liaison est initiée en anaphase-télophase et qu'elle est complètement restaurée dans la plupart des régions régulatrices 40 minutes après cytokinèse. Cependant, OSN présentent des changements quantitatifs de liaison à leurs sites spécifiques qui diffèrent dans leur dépendance à l'accessibilité de la chromatine. Bien que NANOG puisse se lier à la chromatine inaccessible à des loci peu enrichis en OS, nous avons constaté que OS dirigent la liaison de NANOG à l'échelle du génome pendant la sortie de la

mitose. D'autre part, NANOG stabilise la liaison de OS à leurs sites spécifiques. Il est intéressant de noter qu'au cours de la transition de cellules souches pluripotentes naïves vers un stade développemental plus avancé, l'interaction entre OCT4 et SN devient plus décisive pour le maintien de SN à des régions régulatrices de la pluripotence. En résumé, notre étude suggère que OSN régulent dynamiquement la réactivation du génome pendant la sortie de la mitose, et souligne l'importance d'utiliser des cellules non perturbées pour étudier les changements moléculaires séquentiels sur la chromatine de cellules sortant de mitose.

## Mots-clés

Sortie mitotique, cellules souches embryonnaires de souris, réactivation du génome, re-liaison des facteurs de transcription, restauration de l'accessibilité de la chromatine, réactivation transcriptionnelle, TF pionniers, interaction, synchronisation cellulaire



# Table of Contents

<b>Acknowledgements</b> .....	<b>2</b>
<b>Abstract</b> .....	<b>5</b>
<b>Keywords</b> .....	<b>6</b>
<b>Résumé</b> .....	<b>7</b>
<b>Mots-clés</b> .....	<b>8</b>
<b>List of Figures</b> .....	<b>11</b>
<b>List of Tables</b> .....	<b>12</b>
<b>Chapter 1: Introduction</b> .....	<b>13</b>
<b>1.1 The molecular basis of pluripotent embryonic stem cell identity</b> .....	<b>13</b>
1.1.1 Embryonic stem cells.....	13
1.1.2 Expression of pluripotency-determining transcription factors .....	13
1.1.3 Interaction between OCT4, SOX2 and NANOG .....	14
1.1.4 Pioneer transcription factors .....	15
<b>1.2 Cell cycle in mouse embryonic stem cells</b> .....	<b>16</b>
1.2.1 Cell cycle and pluripotency .....	16
1.2.2 Mitosis is a challenge for the maintenance of cell identity .....	17
1.2.3 Transcription factors determine cell fate during mitotic exit.....	18
1.2.4 Mechanistic basis of cell identity maintenance through mitosis.....	19
1.2.5 The sequence of molecular events leading to genome reactivation during mitotic exit is unclear .....	20
1.2.6 Drug synchronization to study mitosis and mitotic exit .....	21
1.2.7 Fluorescent dyes and reporters to visualize cell cycle dynamics .....	21
<b>1.3 Aim of the thesis</b> .....	<b>22</b>
<b>Chapter 2: Orchestration of pluripotent stem cell genome reactivation during mitotic exit</b> .....	<b>24</b>
<b>2.1 Summary</b> .....	<b>24</b>
<b>2.2 Introduction</b> .....	<b>24</b>
<b>2.3 Results</b> .....	<b>26</b>
2.3.1 Generation of a reporter system to dissect mitotic exit without drug-mediated synchronization .....	26
2.3.2 Transcriptional reactivation of the genome during mitotic exit.....	27
2.3.3 Restoration of the chromatin landscape during mitotic exit .....	29

2.3.4 Post-mitotic binding dynamics of OSN display distinct relationships to local chromatin accessibility.....	33
2.3.5 OCT4 and SOX2 orchestrate genome-wide NANOG occupancy during mitotic exit.....	34
2.3.6 NANOG stabilizes OCT4 and SOX2 binding.....	37
2.3.7 OCT4 becomes increasingly important to maintain NANOG and SOX2 at pluripotency loci during naïve pluripotency exit.....	38
<b>2.4 Discussion .....</b>	<b>40</b>
<b>2.5 Limitations of the study .....</b>	<b>41</b>
<b>2.6 Acknowledgement.....</b>	<b>42</b>
<b>2.7 Author contributions.....</b>	<b>42</b>
<b>2.8 Material and Methods.....</b>	<b>42</b>
2.8.1 Cell culture.....	42
2.8.2 Plasmid construction.....	43
2.8.3 Lentiviral vector production and stable cell line generation .....	43
2.8.4 Sorting of different cell cycle phases .....	44
2.8.5 ATAC-seq .....	44
2.8.6 ChIP-seq.....	45
2.8.7 Nuclear RNA-seq.....	46
2.8.8 Immunofluorescence microscopy .....	47
2.8.9 Time-lapse imaging .....	48
2.8.10 Calculation of the post-cytokinesis time in the different temporal bins of eG1 .....	48
2.8.11 Sequencing data analysis.....	48
2.8.12 Motif and gene ontology analysis .....	50
2.8.13 TMM normalization .....	50
2.8.14 Published datasets .....	50
<b>2.8 Supplementary figures.....</b>	<b>51</b>
<b>2.9 Supplementary tables .....</b>	<b>56</b>
<b>Chapter 3: Conclusion .....</b>	<b>71</b>
<b>3.1 Discussion of the results.....</b>	<b>71</b>
<b>3.2 Future research .....</b>	<b>73</b>
<b>References .....</b>	<b>75</b>
<b>Curriculum vitae – Silja Placzek.....</b>	<b>88</b>

# List of Figures

Figure 1 Comparison between genome organization during mitosis and interphase.....	18
Figure 2 Characterization of mESCs expressing the Cdt1-MD reporter by single-cell tracking and flow cytometry analysis.....	27
Figure 3 Genome reactivation of unsynchronized cells in eG1.....	29
Figure 4 TF binding and chromatin accessibility changes throughout mitotic exit.....	32
Figure 5 OSN are redistributed through eG1.....	34
Figure 6 The interaction between OCT4 and SOX2 with NANOG is locus-dependent.....	36
Figure 7 NANOG loss redistributes OCT4 and SOX2.....	38
Figure 8 OCT4 is required to maintain NANOG at pluripotency regulatory elements in PSCs cultured in serum + LIF.....	39
Figure 9 Model for OSN rebinding during mitotic exit.....	41
Figure S 1 – related to Figure 2: Measurements of mESCs expressing the Cdt1-MD reporter in early G1 and quantification of the H3S10p signal in mitotic cells.....	51
Figure S 2 – related to Figure 4: TMM-normalization of ChIP-seq data and signal quantification of track-subtracted loci.....	52
Figure S 3 – related to Figure 5 and 6: Additional characterization of OSN binding upon mitotic exit and Nanog cluster 1-3.....	53
Figure S 4 – related to Figure 6: Additional characterization of significantly affected loci in the absence of OCT4 or SOX2.....	54
Figure S 5 – related to Figure 7: Additional characterization of significantly affected loci in the absence of NANOG.....	55

## List of Tables

Table S 1 Genes of RNA-seq clusters 1 and 3.....	56
Table S 2 DICE analysis of RNA-seq clusters 1, 2, and 3.....	63
Table S 3 Overview of total peak numbers, assignment to regulatory elements and number of peaks containing one of the indicated motifs.....	66
Table S 4 Total number of peaks in each classified region based on differential binding analysis.....	67
Table S 5 Total number of peaks on the Venn diagrams in each classified region based on differential binding analysis and the area crossed between the indicated samples. .	68

# Chapter 1: Introduction

## 1.1 The molecular basis of pluripotent embryonic stem cell identity

### 1.1.1 Embryonic stem cells

Upon fertilization of the egg, the embryo undergoes a series of cell divisions until a hollow cavity named blastocoel is formed, demarcating the formation of the blastocyst. Initially, the blastocyst is comprised of the blastocoele, the inner cell mass, and a surrounding trophoblast. On day 4, the blastocyst is composed of the epiblast, hypoblast, and trophectoderm (Shahbazi, 2020). Mouse embryonic stem cells (mESCs) are derived from the inner cell mass of the blastocyst, and their capacity to self-renew and give rise to all three germ layers makes them an important model to study pluripotency and cell differentiation (Chambers and Tomlinson, 2009). To maintain mESCs in culture in a pluripotent state, different supplements need to be added to the medium. When mESCs are grown in a medium containing serum and leukemia inhibitory factor (LIF), they resemble pluripotent cells from the post-implantation embryonic stage (ter Huurne et al., 2017). This is mainly due to the activation of the STAT3, PI3K, and MEK/ERK pathways by the cytokine LIF. The STAT3 pathway is involved in the regulation of pluripotent stem cell self-renewal, while the PI3K and MEK/ERK cascades regulate basic cellular processes and the inactivation of GSK3 $\beta$ , a regulator of cell differentiation (Graf et al., 2011). Alternatively, mESCs can be maintained in a more naïve pluripotent state that resembles pluripotent ESCs from the inner cell mass by culturing them in LIF with the addition of the two small molecules PD0325901 and CHIR99021 and without serum (ter Huurne et al., 2017). These two molecules, also referred to together as 2i, target the MEK and WNT pathways, respectively, to suppress cell differentiation (Ohtsuka et al., 2015). Besides culturing mESCs in a ground state of pluripotency, it is also possible to mimic more specified pluripotent states by adjusting the culture medium composition. Like this, mESCs can also resemble an intermediate formative pluripotency or primed pluripotency called epiblast stem cells, the latter resembling pluripotent cells of the implanted blastocyst (Takahashi et al., 2018). Thus, using different culture media allows the study of gradual changes in the transition between various pluripotency states.

### 1.1.2 Expression of pluripotency-determining transcription factors

The maintenance of ESC identity is centered around the three transcription factors (TFs) OCT4, SOX2, and NANOG (OSN) (Chambers and Tomlinson, 2009). Previously, it was

demonstrated through kinetic modeling that the expression of Oct4, Sox2, and Nanog is regulated through the dimerization of OCT4 and SOX2. Moreover, NANOG was found to induce Oct4 and Sox2 and to autoregulate its expression (Chickarmane et al., 2005). OSN bind together to several genes promoting self-renewal and thereby regulating their expression, making them the core of a larger network of TFs (Chen et al., 2008). Besides OSN, it was suggested that there are at least 9-14 candidate genes in mESCs whose depletion led to self-renewal defects (Cinghu et al., 2014; Dunn et al., 2014), and there are many other putative markers for pluripotency (Mallon et al., 2013). In the absence of LIF and 2i, the mRNA of the pluripotency factors Nanog and Klf4 were found to be reduced already 6 h after removal, while Oct4 and Sox2 levels persisted over 24h (Dhaliwal et al., 2018). Furthermore, LIF withdrawal in the absence of 2i for more than 24 h leads to an irreversible commitment to cell differentiation (Trouillas et al., 2009). Although the three core pluripotency TFs OSN contribute to pluripotency maintenance, they have different roles during development, and the impact of their loss on cell fate differs in its severity. The depletion of Oct4 in ESCs leads to trophoblast formation (Kunath et al., 2004), while Oct4 overexpression and its presence during embryo development promote mesendodermal differentiation (Niwa et al., 2000; Thomson et al., 2011). In the absence of Sox2, ESCs differentiate towards trophectoderm-like cells (Masui et al., 2007). Additionally, Sox2 overexpression promotes ectoderm differentiation, which is however first accompanied by a decrease in Sox2 (Thomson et al., 2011). Other than OCT4 and SOX2, ESCs are still able to sustain self-renewal capacities upon the complete depletion of Nanog. However, reduced Nanog levels in ESCs are associated with an increased differentiation potential (Chambers et al., 2007). Recently, it was shown that during epiblast formation, NANOG co-occupies initially several sites together with GATA6 and SOX2. Subsequently, NANOG and SOX2 are relocated to genes associated with primitive endoderm before being progressively silenced (Thompson et al., 2022). Oct4 expression remains stable in the epiblast (Thompson et al., 2022), and previous studies suggested that it might be required for the activation of primitive endoderm genes such as Gata6 and pathways essential for epiblast formation (Frum et al., 2013). Overall, OSN are at the very core of pluripotency by regulating a network of genes involved in self-renewal, and their disruption interferes with cell fate maintenance.

### 1.1.3 Interaction between OCT4, SOX2 and NANOG

The interaction between OCT4 and SOX2 has been extensively studied, and it was shown that they can bind either alone to their respective consensus motif or cooperatively to a common OCT4-SOX2 motif (Chen et al., 2008). In the latter case, the search for the target motif takes place before the formation of a heterodimer and is thus DNA-dependent (Lam et

al., 2012). This naturally suggests that there might be an intrinsic ordering of their binding. This was first described *in vivo* in a 2014 paper, in which the authors used single-molecule imaging in ESCs to demonstrate that SOX2 engages the DNA before OCT4 in about 75% of the cases (Chen et al., 2014). However, it was found that their data was not conclusive for binding order but for energy expenditure for assisted genomic binding (Biddle et al., 2019). Furthermore, an *in vitro* study suggested that OCT4 assists SOX2 binding but not vice versa (Li et al., 2019). However, it seems clear that OCT4-SOX2 binding depends on spatial motif orientation (Li et al., 2019) and that their interaction is mainly mediated indirectly through chromatin accessibility (Friman et al., 2019). Furthermore, when ectopically expressed, SOX2 was shown to markedly enhance OCT4 binding to the genome (Raccaud et al., 2019). Furthermore, OCT4 and SOX2 frequently co-localize on multiple sites in the ESC genome with NANOG (Chambers and Tomlinson, 2009). Previously, it was demonstrated that SOX2 interacts physically with NANOG and that this interaction is required for SOX2 function and therefore, to maintain ESC pluripotency (Gagliardi et al., 2013). However, whether OCT4 and NANOG also interact physically is unclear. More recently, the binding preferences between NANOG and SOX2, and OCT4 were investigated. It was suggested that although NANOG interacts with itself, SOX2, and OCT4, fluorescence cross-correlation spectroscopy showed that the binding strength of NANOG to a partner protein follows the order of SOX2, NANOG, OCT4 (Mistri et al., 2022). Further studies hint at an interdependency between OSN binding events. The absence of OCT4 was associated with a major reduction in the genome-wide binding of SOX2 and NANOG (King and Klose, 2017), and similar effects were observed in the absence of NANOG (Heurtier et al., 2019) and SOX2 (Friman et al., 2019). However, these studies did not investigate the causal relationships between the interactions of OSN during mitotic exit. Overall, OSN exhibit different degrees of interaction, and the loss of either of the TFs leads to dysregulation of its partners.

#### 1.1.4 Pioneer transcription factors

Pioneer transcription factors are a specialized class of TFs that can engage with their DNA target site on nucleosomal DNA and bind to the genome before other factors (Zaret and Carroll, 2011). Upon chromatin binding, pioneer TFs can actively open inaccessible chromatin alone or through recruiting remodeling proteins to facilitate the binding of other DNA-binding proteins (Soufi et al., 2012; Zaret and Carroll, 2011). One challenge that TFs are facing and pioneer TFs can overcome during chromatin binding is that nucleosome occupation is associated with masking the full-length DNA binding motif. Thus, they can recognize partial motifs (Soufi et al., 2015). The ability of nucleosome binding and chromatin activation was demonstrated for FOXA1, GATA4 (Cirillo et al., 2002), KLF4, OCT4, and SOX2 (Soufi et al.,

2015) in humans and mice (Lai et al., 2018). For some TFs, only species-specific pioneering functions were demonstrated, such as NANOG in zebrafish (Lee et al., 2013) or GAF in *Drosophila* (Moshe and Kaplan, 2017). However, many other TFs exhibit features of pioneer TFs, such as cell fate reprogramming or heterochromatin binding (Mayran and Drouin, 2018). The chromatin opening abilities and transcriptional activation of pioneer TFs make them central for cell development and reprogramming (Cirillo et al., 2002; Soufi et al., 2015, 2012; Zaret and Carroll, 2011). Previously, it was found that the overexpression of OCT4, SOX2, and KLF4 (OSK) together with c-Myc is sufficient to reprogram fibroblasts to establish induced pluripotent stem cells (Takahashi and Yamanaka, 2006). While c-Myc enhanced the binding of OSK, OSK bind to pluripotency-associated enhancers to re-activate the expression of characteristic ESC markers (Soufi et al., 2012). Recently, the pioneering activity of OCT4 was also found to be required to remodel pluripotency enhancer accessibility throughout the cell cycle (Friman et al., 2019). Moreover, the chromatin opening activity of OCT4 (King and Klose, 2017) and SOX2 (Friman et al., 2019; King and Klose, 2017) was shown to involve the recruitment of the chromatin remodeler BRG1 to establish accessible chromatin in mESCs. In contrast, the pioneer TF FOXA1 can open the chromatin without the help of a chromatin remodeler (Cirillo et al., 2002) by displacing linker histones and thereby generating chromatin accessibility (Iwafuchi-Doi et al., 2016). Collectively, pioneer TFs enable chromatin remodeling to foster cell fate changes and help maintain cell identity throughout the cell cycle.

## 1.2 Cell cycle in mouse embryonic stem cells

### 1.2.1 Cell cycle and pluripotency

The cell cycle of somatic cells is tightly regulated by a cell cycle control system whose main regulatory proteins are the cyclin-dependent kinases (CDKs). The interplay between CDK and cyclin activity fosters or prevents cell cycle progression depending on cell-internal sensors that detect malfunctions (Alberts et al., 2002). However, the cell cycle of mESCs displays several peculiarities that were suggested to contribute to their capacity for self-renewal and pluripotency. In mESCs, the activity of most cyclin-CDK complexes is strongly reduced, and the mitotic cyclin B exhibits the only oscillatory behavior similar to somatic cells (Zaveri and Dhawan, 2018). Another difference lies in the presence of a restriction point, which is controlled in somatic cells by the retinoblastoma protein (RB), permitting or hindering cells from entering the S phase. Specifically, the phosphorylation state of RB is decisive for cell cycle progression. In an unphosphorylated state, cells stay in the G1 phase, and once phosphorylated by CDKs, cells can progress further to the S phase (Lundberg and Weinberg, 1998; Weinberg, 1995). In mESCs, RB exists in a hyperphosphorylated state, allowing the



unfettered transit rapidly after cell division from G1 to S (Savatier P et al., 1994), making the G1 phase of mESCs shorter than for most other cell types. Indeed, it was demonstrated that the duration of the G1 phase in naïve mESCs is less than 2 h (Sakaue-Sawano et al., 2017; Savatier P et al., 1994) and that upon transition to the primed state, this duration gradually increases (Coronado et al., 2013). Several studies tried to elucidate the connection between a short G1 phase and pluripotency. The overexpression of cyclin E, which promotes G1/S transition with CDK2, accelerates G1 progression in ESCs and delays cell differentiation (Coronado et al., 2013). Conversely, the inhibition and knockdown of CDK2 were found to lengthen the G1 phase without increasing the differentiation potential of ESCs (Li et al., 2012). A recent study showed that G1 lengthening by inhibiting CDK4, another regulator of the G1/S progression, fostered differentiation (Roccio et al., 2013). However, it was also shown that naïve ESCs grown in 2i conditions exhibit an elongated G1 phase compared to serum-grown ESCs (ter Huurne et al., 2017). Hence, further studies that use short-term inhibition or overexpression of specific cell cycle regulators are required to address whether a short G1 phase is indeed decisive for pluripotency maintenance.

### 1.2.2 Mitosis is a challenge for the maintenance of cell identity

Dividing cells face major challenges for their cell identity when they advance through the cell cycle. One of these challenges is mitosis. During mitosis, the chromatin condenses on average 2-3 fold compared to interphase chromatin (Vagnarelli, 2012). Chromatin compaction is accompanied by interference in gene regulation. Importantly, this cannot be explained by a reconfiguration of transcription start sites since it was previously shown that promoters gain chromatin accessibility during mitosis. However, enhancers are less accessible and become more occupied by nucleosomes during mitosis (Festuccia et al., 2019). Long-range interactions governing promoter-enhancer contacts, the formation of topologically associating domains (TADs), and the separation in active (A-type) and inactive compartments (B-type) are lost during mitosis (Zhang et al., 2019). This suggests that the structure of mitotic chromatin fosters an environment that hinders TF binding. Although many TFs lose binding, it has been shown that others remain associated with mitotic chromatin, even though most TFs are colocalizing to a smaller extent with mitotic chromosomes (Deluz et al., 2016; Raccaud et al., 2019). Many TFs enriched on mitotic chromatin have pioneer properties (Mayran and Drouin, 2018), such as SOX2 and FOXA1, but this does not constitute a decisive characteristic for mitotic chromatin binding as other TFs, like OCT4, are less enriched (Raccaud et al., 2019). In the same study, it was found that the electrostatic properties of TFs are the main driver of mitotic chromatin association and that the type of DNA binding domain had a lower influence on mitotic chromatin binding (Raccaud et al., 2019). However, since the formation of TF-DNA

complexes scales with its local concentration, it was hypothesized that the reduced space that mitotic chromatin occupies in comparison to interphase chromatin leads to a competition for chromatin binding, favoring high-affinity TFs (Martin and Cardoso, 2010). Besides chromatin condensation, several TFs undergo phosphorylation during prophase, which was shown to reduce the binding affinity for zinc finger proteins (Rizkallah et al., 2011). Also, OCT4 was found to dissociate from chromatin due to mitotic phosphorylation (Shin et al., 2016). However, although SOX2 is phosphorylated during mitosis (Qi et al., 2016) and NANOG phosphorylation stabilizes its activity in interphase (Moretto-Zita et al., 2010), it is unclear whether their phosphorylation affects mitotic chromatin binding. Both structural and molecular changes in the chromatin environment during mitosis are detectable at the level of transcription. It was found that RNA Pol II binding is lost during prometaphase (C-S Hsiung et al., 2016) and that the difference in gene expression is reduced by fivefold during mitosis compared to asynchronous cells (Palozola et al., 2017). In summary, gene regulation during mitosis is strongly perturbed by loss of long-range DNA interactions, chromatin condensation, loss of TF binding, and as a consequence reduced transcriptional activity.

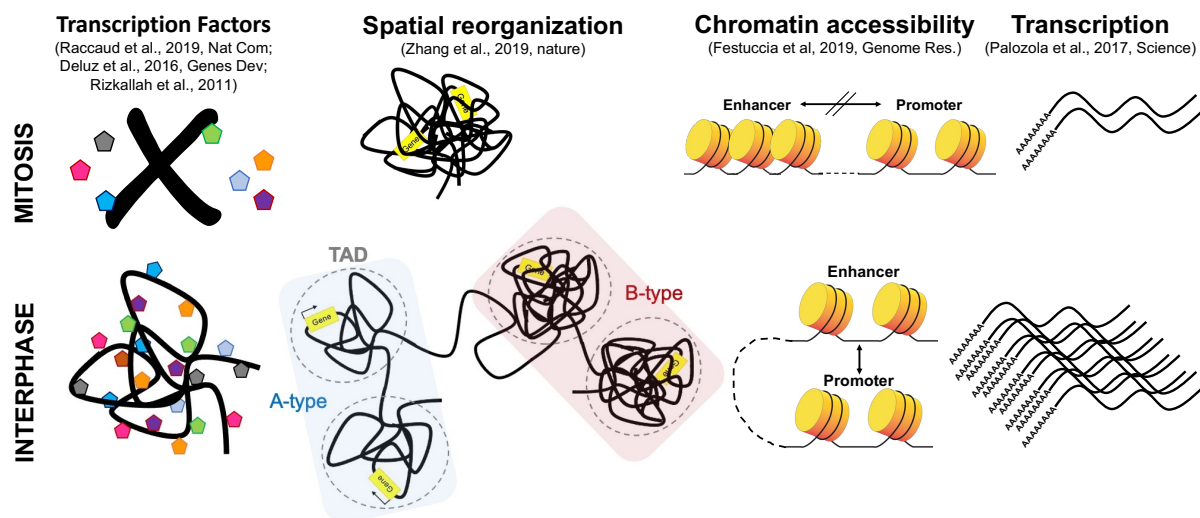


**Figure 1 Comparison between genome organization during mitosis and interphase.**

The mitotic chromatin becomes more condensed compared to interphase, many TFs lose binding, the genome loses its organization and distinction between A- and B-type compartments, TADs are dissolved, enhancers become less accessible, and lose promoter contacts. All these changes during mitosis result in a reduced transcriptional outcome.

### 1.2.3 Transcription factors determine cell fate during mitotic exit

The impaired gene regulation during mitosis constitutes a window of opportunity for cell identity changes. ESCs in the G1 phase of the cell cycle have higher capacities to differentiate into endoderm, mesoderm, or neuroectoderm lineage (Coronado et al., 2013; Pauklin and Vallier, 2013). In a reprogramming experiment, differentiated amphibian oocytes were sorted

into various cell cycle phases. Upon the introduction of reprogramming factors, mitotic cells had a higher expression of Nanog, Oct4, and Sox2, suggesting better responsiveness to cell fate reprogramming (Halley-Stott et al., 2014). On the other hand, mitosis constitutes a major challenge for ESC self-renewal. To maintain their cell identity, mESCs need the presence of cell type-specific proteins during mitotic exit. The transient depletion of SOX2 (Deluz et al., 2016) and OCT4 (Liu et al., 2017) during mitotic exit is associated with pluripotency loss and OCT4 is required to modulate enhancer accessibility (Friman et al., 2019). However, the presence of these TFs is not sufficient to maintain ESC pluripotency as their protein level is tightly linked to cell fate decisions. OCT4 and SOX2 levels fluctuate 2-3 fold over the cell cycle. Furthermore, an elevation of SOX2 levels is associated with an increase in neuroectodermal commitment in G1 (Strebinger et al., 2019). Lower than WT levels of SOX2 are associated with an increased ability to differentiate towards embryonic and extraembryonic lineages upon removal of self-renewing cues (Tremble et al., 2021). Higher OCT4 levels are linked to higher commitment towards mesendoderm and neuroectoderm in G1 (Strebinger et al., 2019), but on the contrary, reduced Oct4 levels cause delayed differentiation and pluripotency exit (Karwacki-Neisius et al., 2013). Aside from Oct4 and Sox2, NANOG levels fluctuate within ESC cultures containing cells with high to undetectable NANOG. However, despite the absence of NANOG in some cells, they were still able to self-renew but had a higher propensity to differentiate (Chambers et al., 2007). In summary, mitosis represents a particular time window in cell fate regulation by both interfering with cell identity maintenance and promoting cell fate transitions.

#### 1.2.4 Mechanistic basis of cell identity maintenance through mitosis

Despite major perturbations in gene regulation during ESC mitosis, ESCs can maintain their cell identity throughout cell division. It was suggested that mitotic bookmarking could serve as a mechanism for the maintenance of cellular identity. Mitotic bookmarking refers to the site-specific interaction of DNA-binding proteins with the genome or the maintenance of histone modification patterns throughout mitosis (Raccaud and Suter, 2018). This specific mitotic retention was proposed to allow the propagation of regulatory information to the next cell cycle and to enable rapid recruitment of co-factors during mitotic exit for swift genome reactivation (Festuccia et al., 2016). Mitotic bookmarking was reported for several DNA-binding proteins such as FoxA1 (Caravaca et al., 2013), GATA1 (Kadauke et al., 2012), CTCF (Burke et al., 2005; Owens et al., 2019), and TBP (Teves et al., 2018; Xing et al., 2008). Recently, it was suggested that the site-specific retention of TBP allows the recruitment of the anaphase-promoting complex (APC/C) during mitosis to transcription start sites (TSSs). This results in histone polyubiquitylation, allowing early post-mitotic gene expression (Oh et al., 2020), and

provides the first functional evidence of the role of mitotic bookmarking in genome reactivation. However, in the case of CTCF, transcriptional reactivation kinetics during mitotic exit displays similar dynamics in the presence or absence of CTCF (Chervova et al., 2023). Additionally, also the pluripotency regulators SOX2 (Deluz et al., 2016; Liu et al., 2017), OCT4 (Liu et al., 2017), and ESRRB (Festuccia et al., 2016) were suggested to remain bound to specific loci during mitosis. However, later studies on the mitotic retention of OCT4 demonstrated that it is mainly excluded from mitotic chromosomes and associated in a sequence-independent manner with mitotic chromatin (Festuccia et al., 2019; Raccaud et al., 2019). On the other hand, SOX2 was globally retained on mitotic chromatin (Deluz et al., 2016; Raccaud et al., 2019), but later studies do not agree on whether this interaction is site-specific (Liu et al., 2017) or sequence-independent (Festuccia et al., 2019). Nevertheless, both specific and nonspecific mitotic binding to the genome were proposed to contribute to the transcriptional reactivation in G1 (Caravaca et al., 2013). This suggests that the mitotic chromatin association of OCT4 and SOX2 might contribute to pluripotency gene reactivation during mitotic exit by increasing their local protein concentration. Taken together, while the contribution of both site-specific and nonspecific retention of DNA-binding factors may play a role in genome reactivation upon mitotic exit, how cells maintain their identity through mitosis remains poorly understood.

### 1.2.5 The sequence of molecular events leading to genome reactivation during mitotic exit is unclear

When cells complete the cell cycle by exiting mitosis, the chromatin landscape needs to be restored and the genome reactivated. Nascent RNA-seq of mitotically-arrested hepatoma cells showed that most genes exhibit an early increase in transcription already during anaphase-telophase (Palozola et al., 2017). However, these genes exhibit higher gene expression as compared to genes that are reactivated later in the cell cycle (C-S Hsiung et al., 2016; Palozola et al., 2017; Pelham-Webb et al., 2021). Hence, it is unclear if the early spike in gene expression is due to better detection of highly expressed genes or if gene expression follows indeed a hierarchical order. At the same time as transcription is reinitiated, enhancer-promoter loops and A-/B-type compartments are formed (Pelham-Webb et al., 2021; Zhang et al., 2019). Although this is in agreement with the conceptual idea of genome reactivation, only a low correlation between the speed of enhancer-promoter loop formation and gene reactivation was observed (Zhang et al., 2019). This suggests that other mechanisms, such as TF search efficiency and concentration, might play a role in fast genome reactivation. Recently, a bioinformatic model to predict TF activities during mitotic exit was developed based on published RNA-seq data (Palozola et al., 2017). TF activities have similar dynamics during

mitotic exit compared to transcriptional initiation, suggesting a hierarchy of intrinsic TF ordering (Sarnataro et al., 2021). However, this model is based exclusively on correlative analysis and thus does not shed light on the functional role of TF ordering in genome reactivation. Aside from that, previous studies found that phosphorylation of zinc finger proteins is reversed in telophase (Rizkallah et al., 2011) and for OCT4 at the M/G1 transition (Shin et al., 2016). This suggests that TF re-binding is likely re-initiated during telophase or cytokinesis. Overall, time-resolved data on TF binding during mitotic exit is still missing and would improve our understanding of the molecular mechanisms leading to genome reactivation.

### 1.2.6 Drug synchronization to study mitosis and mitotic exit

Mitosis in mESCs takes roughly 40 min (Phillips et al., 2019) and is the shortest cell cycle phase. This makes collecting a high enough cell number for genomics experiments very challenging. Therefore, most of the mentioned studies that investigated the molecular events during mitosis and mitotic exit employ drug synchronization to arrest cells in a specific cell cycle phase. The most commonly used drug is nocodazole, which is a microtubule-depolymerizing agent and arrests cells in prometaphase. Upon nocodazole washout, cells are gradually released from the block and can progress through mitosis (Matsui et al., 2012). Using this approach, genome reactivation (C-S Hsiung et al., 2016; Palozola et al., 2017), TF binding, and histone marks (Deluz et al., 2016; Festuccia et al., 2019; Liu et al., 2017), as well as enhancer-promoter loop formation (Pelham-Webb et al., 2021; Zhang et al., 2019) were studied in different mitotic phases. However, it was found that nocodazole synchronization results in substantial changes in gene expression, chromatin accessibility, and reduced colony formation upon release (Shlyueva et al., 2022). Another drug that can be used to synchronize cells in G2 is RO-3306, a CDK1 inhibitor, which has a weaker effect on chromatin accessibility, and cells are still able to form colonies upon drug washout (Shlyueva et al., 2022). However, besides the intracellular effects of drug synchronization, intercellular variability in post-drug-washout progression through the cell cycle makes it challenging to interpret the results from these experiments. Once released from the effect of the drug, cells start to cycle at different speeds, which leads to the gradual contamination of different cell cycle phases within different populations (Sarnataro et al., 2021). Thus, studying genome reactivation and TF binding in an unperturbed system would allow to make more reliable conclusions.

### 1.2.7 Fluorescent dyes and reporters to visualize cell cycle dynamics

The visualization of cell cycle phases and their transitions is crucial to improve the understanding of the molecular changes underlying cell fate decisions. The most common way to visualize the cell cycle is by using fluorescent dyes. These include propidium iodide, which

allows the detection of total DNA, and BrdU, to identify newly synthesized DNA in fixed cells (Cecchini et al., 2012). Another frequently used dye is Hoechst for staining the DNA content. It has the advantage of being membrane-permeable, which makes it suitable for live-cell imaging (Darzynkiewicz et al., 2010). However, the sharp demarcation of the fluorescent signal between different cell cycle phases hinders the distinction of minute changes in cell cycle progression, and hence, they cannot map cell cycle phase transitions. Therefore, the study of cell cycle phase transitions requires internal fluorescent markers that oscillate based on cell cycle progression. Previously, this was achieved using the ubiquitination-based cell cycle indicator FUCCI (SA), which combines two fluorescent reporters fused to specific degradation sequences of hCdt1 and geminin. The degradation of hCdt1 is conducted by the E3 ubiquitin ligase SCF<sup>Skp2</sup> targeting the cyclin-dependent motif (Cy motif) in S/G2/M (Sakaue-Sawano et al., 2008). The E3 ubiquitin ligase APC<sup>Cdh1</sup> is active from anaphase to G1 (Zhou et al., 2016) and degrades geminin in M/G1. Thus, the two fluorescent reporters oscillate reciprocally, highlighting the G1-S transition by labeling cells in S/G2/M and M/G1 with distinct fluorescence signatures (Sakaue-Sawano et al., 2008). The same lab introduced FUCCI (CA), which similarly to FUCCI (SA), combines the degradation of geminin and hCdt1. However, due to the loss of the Cy motif, hCdt1 is targeted by CUL<sup>Dbp1</sup> at the PCNA interaction protein motif in S phase. This allows the distinction between cells in G1, S, and G2 and highlights the M-G1 transition (Sakaue-Sawano et al., 2017). Although the M-G1 transition can be monitored, FUCCI (CA) is not precise enough to distinguish different temporal bins of mitotic exit. Another fluorescent reporter system takes advantage of the mitosis-specific degradation domain (MD) of cyclin B1. The MD is degraded by APC<sup>Cdc20</sup>, which is active during early and mid-mitosis (Zhou et al., 2016). This allows distinguishing cells in early G1, late G1, S, and G2/M when combined with Hoechst staining (Kadauke et al., 2012).

### 1.3 Aim of the thesis

Previous studies identified mitotic exit as a key cell fate-determining time window, enabled by the genome-wide reorganization of the gene regulatory machinery during mitosis. However, the sequence of molecular events leading to the global restoration of the chromatin landscape in mESCs is unclear. Thus, in the frame of this thesis, we aim to address the sequence of molecular events occurring during mitotic exit with a high temporal resolution and without drug-mediated cell synchronization. We mainly focus on OCT4 and SOX2, which were found to be decisive for the maintenance of ESC identity, and on NANOG, which frequently co-occupies similar sites in the genome, to decipher the sequence of their re-binding during mitotic exit. Since the current fluorescent reporter strategies do not have the time resolution allowing to sort sub-hour temporal bins during mitotic exit, we first aimed at engineering a new reporter

system. Subsequently, we used CHIP-seq, ATAC-seq, and nucRNA-seq to address the following questions:

- What is the dynamics of transcriptional reactivation in eG1?
- What are the dynamics of OSN rebinding during mitotic exit?
- How does the genome-wide binding distribution of OSN and chromatin accessibility change during mitotic exit?
- How do OCT4 and SOX2 regulate NANOG binding during mitotic exit?
- How does NANOG regulate OCT4 and SOX2 binding?

## Chapter 2: Orchestration of pluripotent stem cell genome reactivation during mitotic exit

In this chapter, the following pre-print publication was added and formatted to fit with the style of the thesis. This manuscript was submitted to *Developmental Cell*.

Placzek S, Vanzan L and Suter DM (2023) Orchestration of pluripotent stem cell genome reactivation during mitotic exit.

### 2.1 Summary

The maintenance of cell identity faces many challenges during mitosis, as most DNA-binding proteins are evicted from DNA and transcription is virtually abolished. How cells maintain their identity through cell division and faithfully re-initiate gene expression during mitotic exit is unclear. Here, we developed a novel reporter system enabling cell cycle synchronization-free separation of pluripotent stem cells in temporal bins of < 30 minutes during mitotic exit. This allowed us to quantify genome-wide reactivation of transcription, sequential changes in chromatin accessibility, and re-binding of the pluripotency transcription factors OCT4, SOX2, and NANOG (OSN). We found that transcriptional activity progressively ramped up after mitosis and that OSN rapidly reoccupied the genome during the anaphase-telophase transition. We also demonstrate transcription factor-specific, dynamic relocation patterns and a hierarchical reorganization of the OSN binding landscape governed by OCT4 and SOX2. Our study sheds light on the dynamic orchestration of transcriptional reactivation after mitosis.

### 2.2 Introduction

During mitosis, chromatin is reorganized into a condensed state that disrupts the three-dimensional architecture of the genome (Gibcus et al., 2018), impairs transcription factor (TF) binding (Deluz et al., 2016; Raccaud et al., 2019) and transcriptional activity (Palozola et al., 2017). When cells exit mitosis, the whole gene regulatory landscape needs to be re-established to allow for transcriptional reactivation.

A major limitation in the field is the systematic use of cell cycle-synchronizing drugs. The vast majority of studies on mammalian gene regulation during and immediately after mitosis use nocodazole to arrest cells in prometaphase (Jordan et al., 1992; Matsui et al., 2012), followed by nocodazole wash-out to allow cells to resume progression through the cell cycle (C-S Hsiung et al., 2016; Festuccia et al., 2016; Liu et al., 2017; Palozola et al., 2017). Several hours to overnight treatment with nocodazole are used to obtain enough cells in mitosis or



mitotic exit. This leads to a strong enrichment of cells in prometaphase and distorts the timing of cell cycle progression, as cells typically pass through all mitotic phases within less than 1 hour (Phillips et al., 2019). Furthermore, nocodazole treatment alters chromatin compaction and transcriptional activity beyond what can be explained by the enrichment of cells in mitosis (Shlyueva et al., 2022). Upon drug washout, individual cells display substantial variability in the timing of mitotic exit (Sarnataro et al., 2021), which blurs the dissection of genome reactivation dynamics. This raises important concerns on the physiological relevance of genome reactivation upon release from drug-mediated cell cycle synchronization.

The temporal sequence in which regulatory events involved in genome reactivation occur is mostly unknown. Promoter-enhancer contact re-establishment initiates at the anaphase to telophase transition and follows locus-specific kinetics (Zhang et al., 2019), but whether distinct TF re-binding dynamics orchestrate these changes is unclear. TF activities inferred from RNA-seq data were reported to display a TF-specific temporal ordering during mitotic exit (Sarnataro et al., 2021). However, the sequence of TF rebinding to specific sites after mitosis awaits to be dissected to shed light on the mechanistic basis of this temporal organization.

In self-renewing cells such as pluripotent stem cells (PSCs), gene regulation needs to be robustly controlled throughout the cell cycle to maintain their identity over a large number of cell divisions. The core pluripotency TFs OCT4 and SOX2 play a central role in regulating PSC self-renewal during mitotic exit (Deluz et al., 2016; Friman et al., 2019; Liu et al., 2017). OCT4 and SOX2 form heterodimers and frequently co-occupy loci genome-wide with NANOG (Chambers and Tomlinson, 2009). The pioneer properties of OCT4 and SOX2 (Soufi et al., 2015) allow them to make chromatin accessible for the binding of non-pioneer TFs. NANOG was demonstrated to have a strong physical interaction with SOX2 and a weak one with OCT4 (Gagliardi et al., 2013; Mistri et al., 2022), suggesting distinct interaction patterns between these three TFs. How OCT4, SOX2 and NANOG orchestrate their temporal pattern of rebinding during mitotic exit remains unexplored.

Here we describe a new strategy to dissect genome reactivation during mitotic exit in unsynchronized PSCs, allowing us to decipher transcriptional reactivation dynamics and acute temporal changes in the binding of pluripotency TFs and chromatin accessibility. In combination with loss-of-function studies of each individual TF, our study reveals how TF interactions regulate their binding landscape during mitotic exit.

## 2.3 Results

### 2.3.1 Generation of a reporter system to dissect mitotic exit without drug-mediated synchronization

To overcome the limitations of drug-mediated arrest of cells in mitosis, we designed a cell cycle synchronization-free strategy to study mitotic exit under physiological conditions. Our approach is based on a fluorescent reporter system that allows us to discriminate cells at different time points just before and within 2 h after cytokinesis. Briefly, we expressed two E3 ligase substrates, the mitotic destruction domain (MD) of cyclin B1 (Kadauke et al., 2012) and hCdt1(1/100)Cy(-) (Sakaue-Sawano et al., 2017) in fusion to YPet and mCherry, respectively. This allows for the degradation of YPet and mCherry at the metaphase-anaphase transition and in S phase, respectively, in a cell cycle-controlled manner. We inserted these two constructs downstream of the PGK and EF1 $\alpha$  constitutively active promoters, respectively, into a lentiviral vector and established a clonal mouse embryonic stem cell (mESC) line stably expressing both reporters (Cdt1-MD cell line). We then performed time-lapse fluorescence microscopy and tracked YPet and mCherry fluorescence intensities of individual cells during mitotic exit. YPet fluorescence decreased during late mitosis and started to slowly increase 1h after cell division. In contrast, mCherry fluorescence was high at the beginning of G1 (early G1) and was lost 2 h after cell division (late G1), in line with the activity of CUL4<sup>Ddb1</sup> (Nishitani et al., 2006) (Figure 2A). The distinct temporal changes of YPet and mCherry signals resulted in characteristic cellular trajectories in a two-dimensional fluorescence space (Figure 2B and S1A), allowing to assign cells to different time windows after mitotic exit by measuring their YPet and mCherry fluorescence signals. Focusing on the first 2 h after cytokinesis, we then classified cells into four equal bins of fluorescence progression (Figure 2C). We next stained this cell line with Hoechst and determined mCherry and YPet intensities of individual cells in G1 phase by flow cytometry. The fluorescence intensities acquired by microscopy could thus be correlated to those acquired by flow cytometry. This allowed us to assign cells analyzed by flow cytometry to a given temporal bin, thus enabling us to physically separate cells at different time points after cytokinesis by FACS (Figure 2D, Figure S1B and STAR Methods). We then allocated the cells from each fluorescence bin to their respective temporal position relative to cytokinesis. We found that the four fluorescence bins corresponded to cells that advanced past cytokinesis for an average of 42, 63, 87, and 110 minutes, respectively (Figure 2E). We also reasoned that this reporter system should allow sorting for cells in anaphase and telophase. We established an enrichment strategy based on their high mCherry, intermediate YPet intensities, and high DNA content (Figure 2F). Furthermore, staining against the mitotic-specific marker H3S10p allows to select for mitotic cells (Wen et al., 2005), which we could

also observe in mESCs at all stages of mitosis (Figure S1C, D). Thus, we additionally stained our reporter cell line with an antibody against H3S10p to prevent contamination with interphase cells. Upon examination by microscopy, we found that 19.9 % of the cells were in anaphase and 12.4 % in telophase (Figure S1C-E).

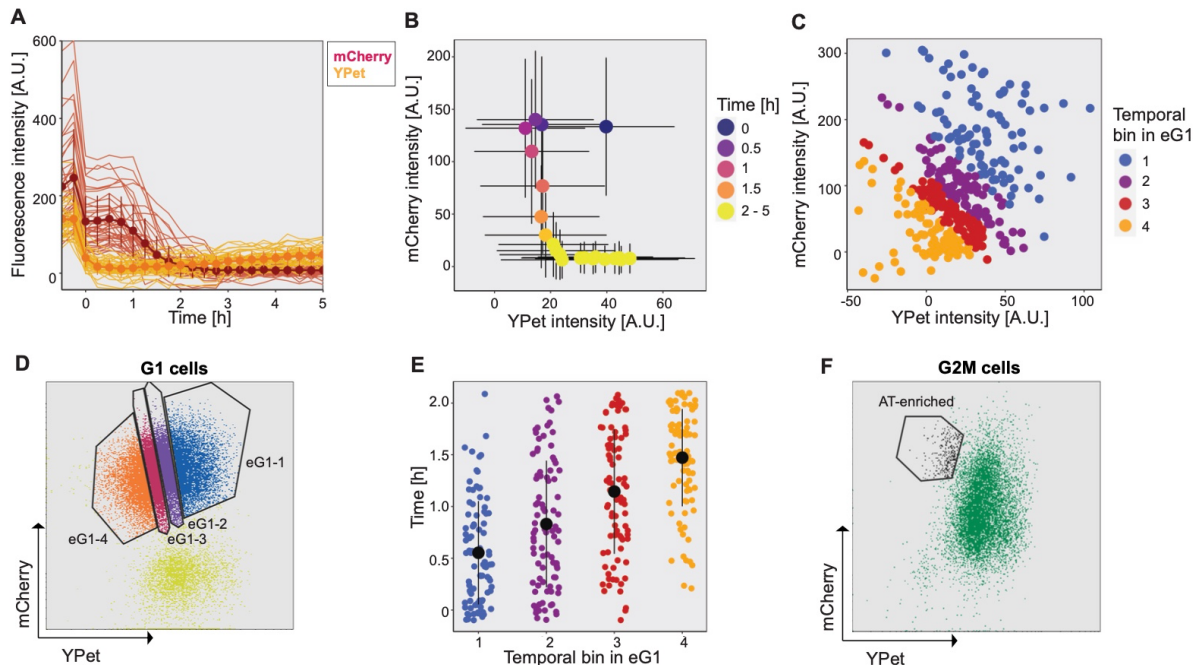


**Figure 2 Characterization of mESCs expressing the Cdt1-MD reporter by single-cell tracking and flow cytometry analysis.**

(A) Temporal profile of the integrated fluorescence intensity of mCherry and YPet spanning M-G1. N=40 cells measured before cell division (time point -0.25). One sister cell was followed for 20 frames with a time interval of 15 min (5h). Dots: fluorescence mean intensity. Error bars: standard deviation (SD). Lines: single-cell traces. (B) Average integrated fluorescence intensity of mCherry and YPet for each time point of 40 cells measured over 5h after cytokinesis. Error bars: SD. (C) The first 9 time points after mitotic exit were extracted, and four temporal bins of eG1 containing an equal number of cells (as in Fig. 1D) were gated based on the reporter expression. (D) YPet and mCherry fluorescence of G1-gated cells based on Hoechst staining. Temporal bins of eG1 were gated to select an equal number of cells for each time point in eG1. Blue: eG1-1 cells; Purple: eG1-2 cells; Red: eG1-3 cells; Orange: eG1-4 cells; Yellow: late G1 cells. (E) Flow cytometry and microscopy data (Fig. 1C) were used to calculate the average time that has passed since cytokinesis in the eG1 bins. The cells left cytokinesis on average for 42 min (eG1-1, blue), 63 min (eG1-2, purple), 87 min (eG1-3, red), and 110 min (eG1-4, orange), respectively. Black dots: median; Black lines: SD. (F) YPet and mCherry fluorescence of G2M-gated cells. The gated cell population is enriched in anaphase-telophase cells, which are mCherry-high and YPet-low, and were further selected based on positive H3S10p staining.

### 2.3.2 Transcriptional reactivation of the genome during mitotic exit

While previous studies have reported an early spike in transcriptional activity within the first hour of G1 phase, these used nocodazole-released cells blocked for several hours in prometaphase, raising the possibility that this observation may not fully reflect physiological

reactivation of transcription (Chervova et al., 2023; C-S Hsiung et al., 2016; Palozola et al., 2017). We thus took advantage of the Cdt1-MD cell line to sort cells into four temporal bins of eG1 to quantify changes in transcriptional activity over time in eG1 using nuclear RNA-seq. In contrast to these earlier studies, we found that on average, intronic and exonic reads progressively increased and decreased, respectively, from eG1-1 to eG1-4 (Figure 3A, B). This suggests that transcriptional activity ramps up over at least 2 h after cytokinesis, while the decrease in exonic reads might be caused by a progressive increase in nuclear mRNA decay, in line with the previously reported mitosis-G1 wave of mRNA decay (Krenning et al., 2022). We then classified the dynamics of transcriptional reactivation of different genes in three clusters according to their temporal changes in unspliced (introns and intron-exon junctions) and exonic read counts (see STAR Methods). We found that most genes were already highly expressed in eG1-1 and maintained their expression at a high level throughout eG1 (Figure 3C, cluster 2). These genes are mainly involved in basic cellular processes but are also strongly enriched for the pluripotency GO term (Figure 3D). Cluster 1 genes displayed increasing unspliced and sharply decreasing exonic reads over time, suggesting transcriptional reactivation but destabilization of the mature mRNA. Cluster 3 genes displayed an opposite pattern compared to cluster 1, with a decrease in unspliced mRNAs from eG1-1 to eG1-2 but an increase in exonic reads, suggesting transcriptional shutdown and stabilization of spliced mRNAs (Figure 3C). Both clusters 1 and 3 were depleted in pluripotency terms and enriched in genes involved in cell fate commitment (Figure 3D and Table S1 and S2), suggesting that PSCs use both transcriptional and post-transcriptional mechanisms to keep the activity of genes involved in differentiation in check.

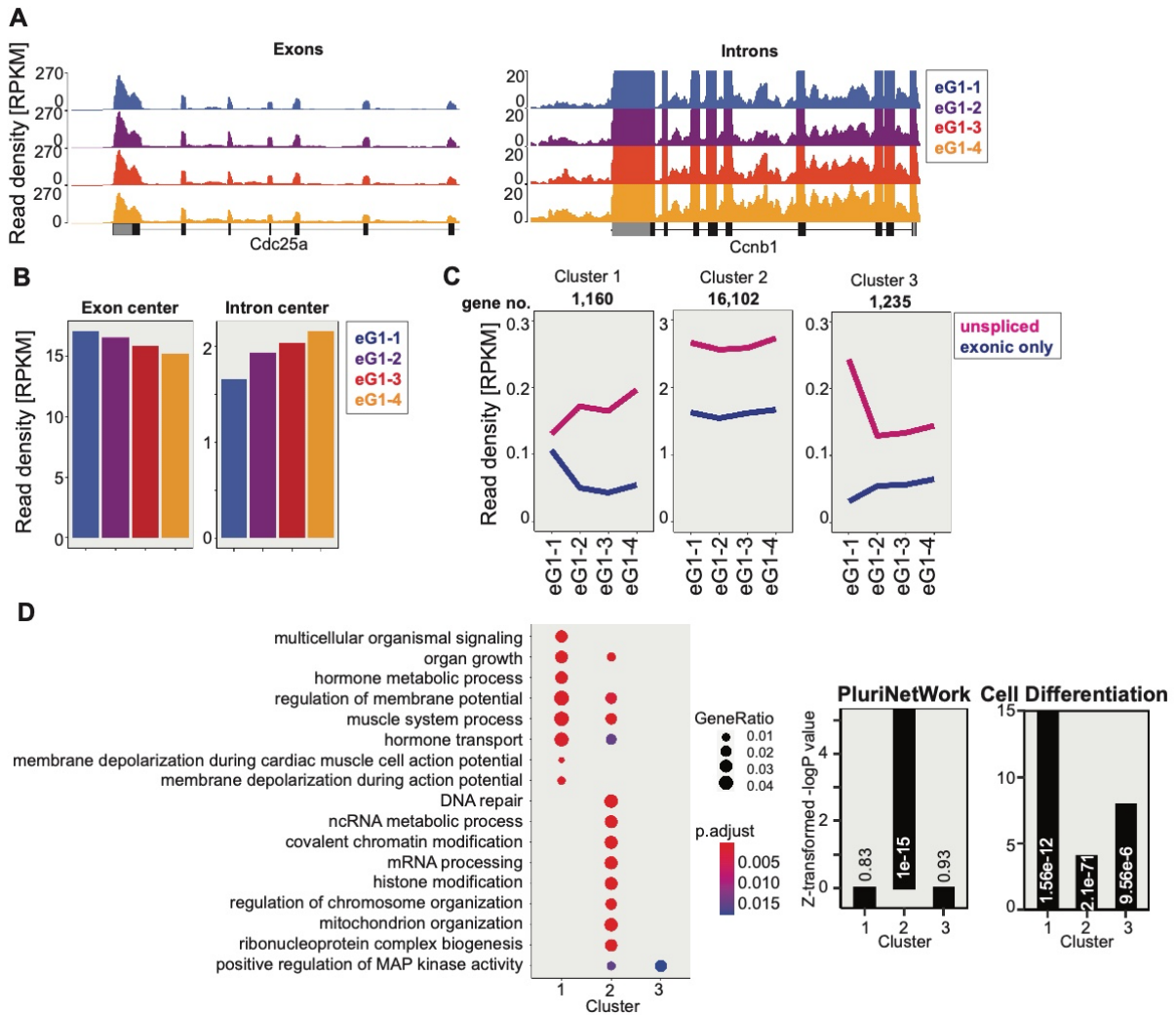


**Figure 3 Genome reactivation of unsynchronized cells in eG1.**

(A) Representative examples of genome browser tracks of RNA-seq signal decreasing at exons (left) or increasing at introns (right). (B) Mean of total RNA-seq signal in different temporal bins of eG1 at the center of all exons or introns, respectively. (C) Temporal changes in read density for unspliced and exonic reads in the three clusters. The number of genes in each cluster is indicated. Lines: median. (D) GO term enrichment for the clusters shown in panel C (left) and relative enrichment values plotted as Z-transformed  $-\log P$  value and p-values (digits) of GO terms PluriNetWork and Cell differentiation for the different clusters (right).

### 2.3.3 Restoration of the chromatin landscape during mitotic exit

We then used the *Cdt1*-MD cell line to map genome-wide binding of the pluripotency transcription factors OCT4, SOX2, and NANOG (OSN) in unsynchronized mitotic, anaphase-telophase-enriched (AT-enriched) cells and four temporal bins of eG1 (eG1-1 to eG1-4). We sorted roughly 1 million cells for eG1-1 to eG1-4, allowing us to use 3.5  $\mu\text{g}$  of chromatin for ChIP-seq. Because of the challenge to obtain large numbers of unsynchronized mitotic and AT-enriched cells, we optimized a ChIP-seq procedure using only 50,000 cells for these populations (see STAR Methods). We also acquired OSN ChIP-seq samples of eG1-1 cells with 50,000 cells to compare these three phases. This also allowed us to rescale the reads of

the mitotic and AT-enriched samples to the eG1-1 to eG1-4 datasets obtained with 1 million cells, and thus to seamlessly compare all time points (see STAR Methods). All ChIP-seq data was spike-in-normalized using *Drosophila* chromatin (Bonhoure et al., 2014; Orlando et al., 2014) for quantitative comparisons between samples.

OSN bound to very few sites in mitosis (Table S3) but markedly increased their genome occupancy in AT-enriched cells to reach similar levels over the whole genome in eG1-1 (Figure 4A and Figure S2B). Importantly, we also generated an OCT4 ChIP-seq dataset from 1 million unsynchronized mitotic cells, which confirmed the very low mitotic occupancy of OCT4. This suggests that the low number of peaks found in the 50,000-cells mitotic samples cannot be simply explained by the lower chromatin input (Figure S2A). To dissect locus-specific changes in TF binding during mitosis, we next performed a Trimmed Mean of M-values (TMM)-normalization (Robinson and Oshlack, 2010) on the ChIP-seq data, which allows for normalization of technical variation during sample preparation (Figure S2C-D). We then quantified temporal changes in OSN binding to regulatory elements. We found that all three TFs were mainly occupying promoters and active enhancers before progressively spreading to other genomic regions during AT and eG1 (Figure 4B). To quantify locus-specific temporal changes in TF binding during mitotic exit, we next performed a track subtraction (see STAR Methods) between each two consecutive timepoints for each TF, and quantified changes in peak intensities at all bound loci. Genomic loci were ordered according to quantitative changes between mitosis and AT-enriched cells (Figure 4C). TF occupancy increased from mitosis to AT-enriched cells at all loci, while changes in TF occupancy were more bidirectional between later time points. Interestingly, loci that most strongly increased their binding occupancy from mitosis to AT-enriched cells tended to further increase their binding in eG1-1, and conversely for those that lost binding (Figure 4C), suggesting a progressive and consistent TF relocation from mitosis to eG1. For better visualization, we also quantified the magnitude of these changes from eG1-1 to eG1-4 in violin plots and their standard deviation, which show that OCT4 and NANOG relocalization occurred throughout eG1-1 while SOX2 was mainly redistributed between eG1-1 and eG1-2 (Figure 4C). As OSN colocalize at many loci in the genome (Chen et al., 2008), we next asked how the co-binding behavior between OSN changes over time by performing a track subtraction between each consecutive time point for each TF pair. Using this metric on the TMM-normalized data, a perfect co-localization at a given locus will result in a value of 0, while any deviation from this value means that one TF binds more than the other relative to its genome-wide binding. As expected, we found that OCT4 and SOX2 were more co-localized together than with NANOG, in line with their binding as a heterodimer at most genomic loci (Chen et al., 2008; Rodda et al., 2005). While the co-binding of SOX2 with NANOG and OCT4 stayed constant, the co-binding of OCT4 with NANOG slightly decreased over time (Figure 4D).

Next, we quantified chromatin accessibility changes throughout eG1 using ATAC-seq. We found that global chromatin accessibility was already mostly restored in eG1-1 (Figure 4E, Figure S2E-F). We then quantified changes in accessibility of promoters and active enhancers throughout eG1. To do so, we performed a track subtraction between consecutive time points (Figure 4F) and extracted loci that increased or decreased in accessibility over time. We found that the largest changes in accessibility occurred between eG1-1 and eG1-2, and that a majority of active promoters and enhancers increased in accessibility over time (Figure S2G). The loci increasing accessibility between two consecutive time points were mostly the same throughout eG1, in contrast to loci losing accessibility (Figure 4G, Table S5). Therefore, a large fraction of regulatory regions display a consistent, gradual re-establishment of chromatin accessibility throughout eG1, while the closing of regulatory regions during eG1 is less coordinated in time.

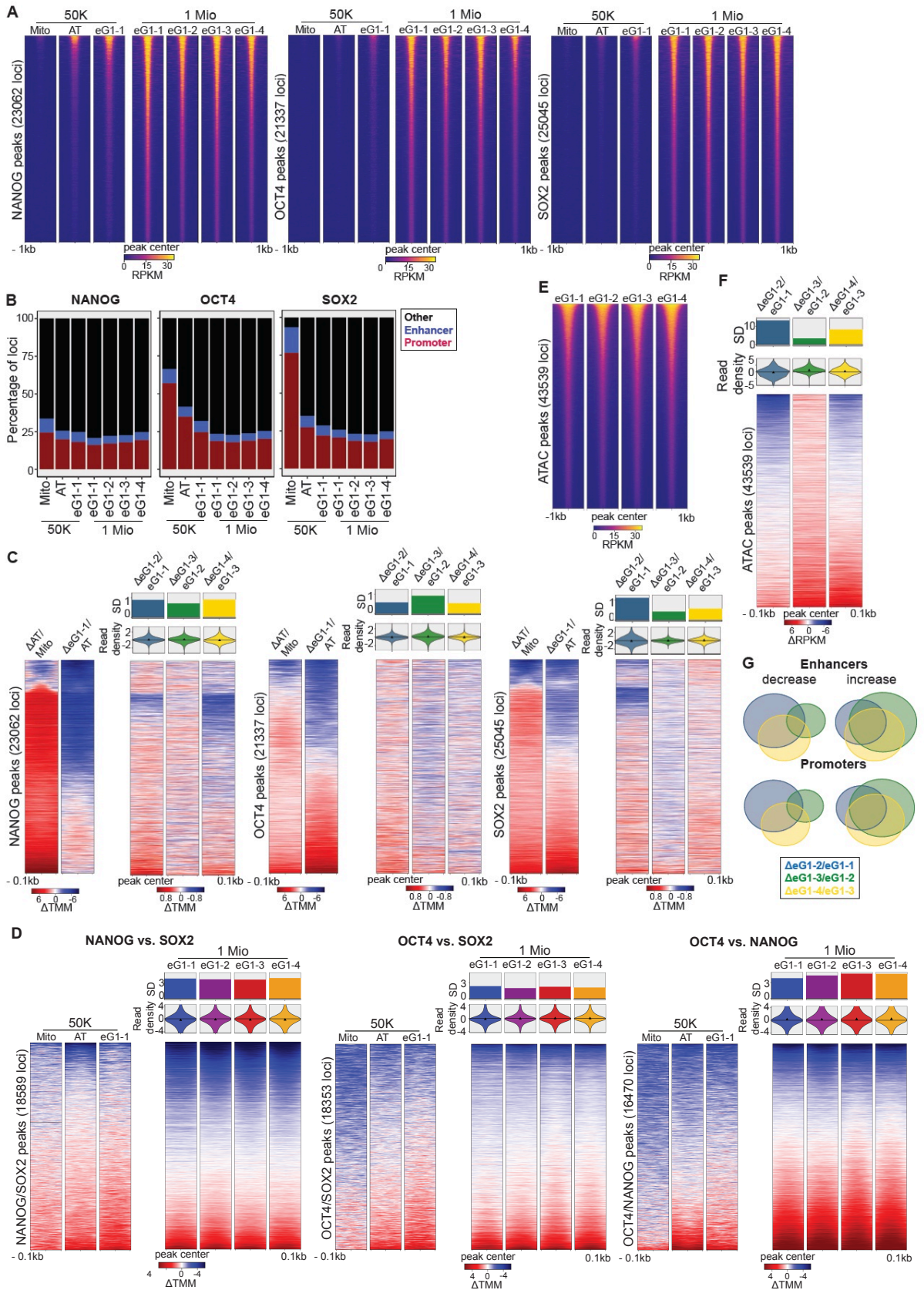


**Figure 4 TF binding and chromatin accessibility changes throughout mitotic exit.**

(A) Heatmaps of spike-in and RPKM-normalized ChIP-seq binding of OSN in mitosis (Mito), AT-enriched cells (AT), and different temporal bins of eG1. Signals are ranked by intensity, and each row represents one locus. (B) Overlap of OSN binding sites with active enhancer and promoter peaks at different time points. (C) Heatmaps of  $\Delta$ TMM



track-subtracted reads between different timepoints for OSN on all peaks. Positive (red) and negative (blue) values: increase and decrease in signal, respectively. SD of the values plotted in the heatmaps and violin plots. Triangles: median. (D) Heatmaps of  $\Delta$ TMM track-subtracted read density between the indicated TFs 100bp around their common peaks. Positive (red) and negative (blue) values: increase and decrease in overlap, respectively. SD of the values plotted in the heatmaps and violin plots. Triangles: median. (E) Heatmaps of RPKM-normalized ATAC-seq data on different temporal bins of eG1. (F) Heatmaps of the  $\Delta$ RPKM track subtracted ATAC-seq reads between each subsequent timepoint of the ATAC-seq data. Positive (red) and negative (blue) values: increase and decrease in signal, respectively. SD of the values plotted in the heatmaps and violin plots. Triangles: median. (G) Overlap between active enhancers and promoters that decrease or increase in accessibility between different time points in eG1.

### 2.3.4 Post-mitotic binding dynamics of OSN display distinct relationships to local chromatin accessibility

We next classified OSN binding sites into clusters characterized by distinct dynamic changes in occupancy (see STAR Methods) and related these to local chromatin accessibility. We identified three clusters that displayed increased, stable, or decreased TF enrichment throughout eG1. For NANOG, clusters 1 and 2 displayed high chromatin accessibility, in contrast to cluster 3 that was less accessible (Figure 5A). We then quantified the overlap of these clusters with loci that depend on the pioneer activity of OCT4 and SOX2. These regions were defined by measuring changes in chromatin accessibility after acute depletion of either OCT4 or SOX2, allowing us to determine which loci depend only on the pioneering activity of OCT4 (OCT4-dependent), only on the pioneering activity of SOX2 (SOX2-dependent) or required the pioneering activity of both OCT4 and SOX2 (Co-dependent) to maintain their accessibility (Friman et al., 2019). We found that clusters 1 and 2 were more enriched in OCT4-dependent and Co-dependent regions than cluster 3 (Figure S3A). In contrast, cluster 3 was more enriched in SOX2-dependent regions (Figure S3A), less enriched in pluripotency terms, and more in differentiation terms (Figure 5A). Therefore, NANOG initially scans regions that are both less accessible and less related to pluripotency maintenance, to later relocate to pluripotency regulatory regions made accessible by the activity of OCT4 alone or OCT4 and SOX2 together. In the case of OCT4, regions increasing its enrichment from eG1-1 to eG1-4 were the most accessible, while those decreasing OCT4 binding were the least accessible. This suggests that pre-existing chromatin accessibility fosters and sustains robust OCT4 binding during eG1. Interestingly, pluripotency and differentiation terms were both most enriched in regions increasing or maintaining high OCT4 binding (Figure 5B). Finally, SOX2 binding displayed a strong preference for accessible regions during eG1-1 before relocating to less accessible regions in eG1-2 (Figure 5C). Overall, these results indicate that different pluripotency TFs exhibit distinct relocalization dynamics upon mitotic exit, associated with TF-specific chromatin accessibility profiles and functional gene categories.

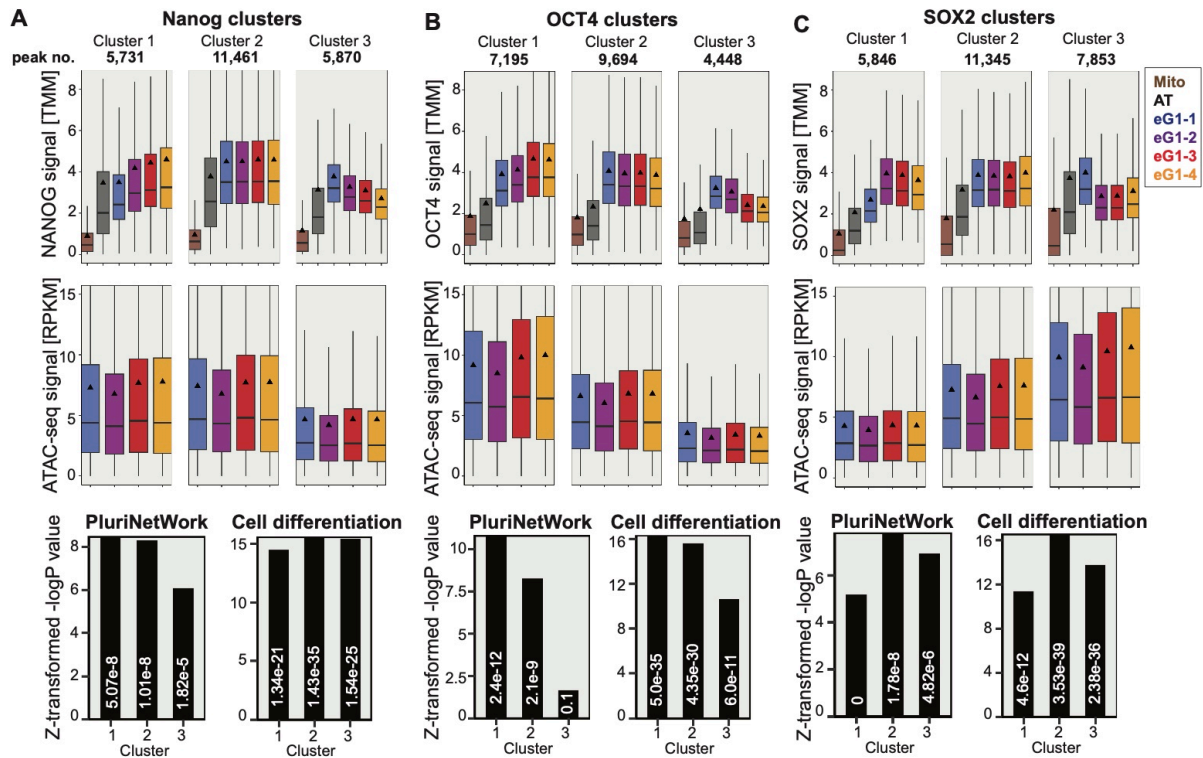


**Figure 5 OSN are redistributed through eG1.**

(A-C) Boxplots of the TMM-signal after clustering of NANOG (A), OCT4 (B), or SOX2 (C) binding. Boxes: intervals between the 25th and 75th percentile. Horizontal lines: median; Triangles: mean; Error bars: 1.5-fold the interquartile range or the closest data point when the data point is outside this range. RPKM-signal of ATAC-seq data underneath. Last row: relative enrichment values of the Z-transformed -logP value and p-value (digits) of GO term enrichment of PluriNetWork and Cell differentiation.

### 2.3.5 OCT4 and SOX2 orchestrate genome-wide NANOG occupancy during mitotic exit

To further dissect the orchestration of TF re-binding during mitotic exit, we probed how OSN binding depend on the presence of each other. To do so, we used the ZHBTc4 and 2TS22C cell lines, in which OCT4 (Niwa et al., 2000) or SOX2 (Masui et al., 2007), respectively, can be depleted using a doxycycline-inducible Tet-off system. In addition, we used the 44iN (Festuccia et al., 2012) cell line, in which NANOG is controlled by a Tet-on system and can be depleted by doxycycline removal. While OCT4 and SOX2 loss had a strong impact on the binding of the two other respective TFs and on chromatin accessibility at their binding sites, NANOG loss had only a mild impact on these (Figure 6A). We thus focused on how NANOG binding dynamics correlated with OCT4 and SOX2 binding dynamics during mitotic exit.

OCT4 and SOX2 were almost maximally enriched in eG1-1 in NANOG cluster 1, where NANOG binding increases over time (Figure 6B). Cluster 1 was also most highly enriched in the OCT4::SOX2 motif (Figure S3B-C). This is compatible with the progressive relocalization of NANOG to cluster 1 being dependent on the strong and early binding of OCT4 and SOX2

to these loci. We next used the datasets in which OCT4 (this study) or SOX2 (this study and Friman et al., 2019) were depleted to interrogate how NANOG binding changes at the three NANOG clusters. While the loss of OCT4 and SOX2 led to a decrease in NANOG enrichment at all clusters (Figure 6C-D), The impact of SOX2 loss and OCT4 loss were strongest and weakest, respectively, on both NANOG binding and chromatin accessibility in cluster 3 as compared to cluster 1 and 2. This suggests that SOX2 plays a stronger role than OCT4 for NANOG to bind in cluster 3 loci.

We then further dissected how OCT4 and SOX2 impact NANOG binding using a differential binding analysis on NANOG ChIP-seq in the presence or absence of OCT4 or SOX2. We found that 17 % and 13 % of loci decreased NANOG binding in the absence of OCT4 and SOX2, respectively, and 1.4 % of loci increased NANOG binding in the absence of OCT4 (Figure 6E-F, Table S4). We next performed ChIP-seq on SOX2 and OCT4 in the presence or absence of OCT4 or SOX2, respectively, and using a published ATAC-seq dataset acquired in the same conditions (Friman et al., 2019). Upon loss of OCT4 or SOX2, the loci that significantly decreased NANOG binding also lost the binding of SOX2 or OCT4, respectively, and became inaccessible (Figure 6E-F). Loci that significantly increased NANOG binding in the absence of OCT4 were accompanied by an increase in SOX2 binding and chromatin accessibility (Figure 6E). This indicates that in the absence of OCT4, SOX2 and NANOG are redirected to new sites that become accessible.

We then quantified how OCT4 or SOX2 depletion impact NANOG binding at loci that change NANOG binding in the absence of SOX2 or OCT4, respectively. Upon loss of either TF, sites that decreased NANOG binding in the absence of one TF also decreased NANOG binding in the absence of the other TF and became less accessible (Figure 6G-H). This indicates that both OCT4 and SOX2 are required to maintain chromatin accessibility and allow NANOG binding at these sites. We next identified the loci that increased, stayed stable, or decreased SOX2 or OCT4 binding in the absence of OCT4 or SOX2, respectively, and quantified TF binding changes and chromatin accessibility in these regions. Interestingly, loss of OCT4 resulted in an increased SOX2 binding at 1.8% of loci (Figure S4A), while very few loci increased OCT4 binding upon loss of SOX2 (Figure S4B). Changes in OCT4 and SOX2 binding were always accompanied by corresponding changes in NANOG enrichment and chromatin accessibility (Figure S4A and Figure S4B), and loci that decreased NANOG binding broadly overlapped with the ones that decreased SOX2 or OCT4 binding (Figure S4C, Table S5). Moreover, regions losing NANOG binding highly overlapped with regions depending on OCT4, SOX2 or both for their accessibility (Figure S4D) and were highly enriched in OCT4, SOX2, and OCT4::SOX2 motifs (Figure S4E-F). Regions where NANOG binding increased upon OCT4 loss had strong NANOG and SOX2 motifs but weak OCT4 and OCT4::SOX2 motifs (Figure S4G-H) and were depleted in GO terms involved in pluripotency (Figure S4I-J).

Furthermore, these regions lost NANOG binding upon SOX2 loss (Figure 6G), indicating that SOX2 is required for NANOG binding to those loci.

Taken together, these results indicate that OCT4 and SOX2 broadly cooperate to facilitate NANOG binding at pluripotency regulatory elements and that in the absence of OCT4, SOX2 redirects NANOG to loci that are not involved in pluripotency maintenance. These results echo the lower and higher dependency of NANOG on the pioneering activity of OCT4 and SOX2, respectively, during eG1-1 (cluster 3 in Figure S3A), leading to its binding to loci less enriched for pluripotency terms (cluster 3 in Figure 5A), and subsequent NANOG relocation to loci that are OCT4-dependent or Co-dependent and more enriched for pluripotency terms (clusters 1 and 2 in Figure S3A and Figure 5A, respectively).

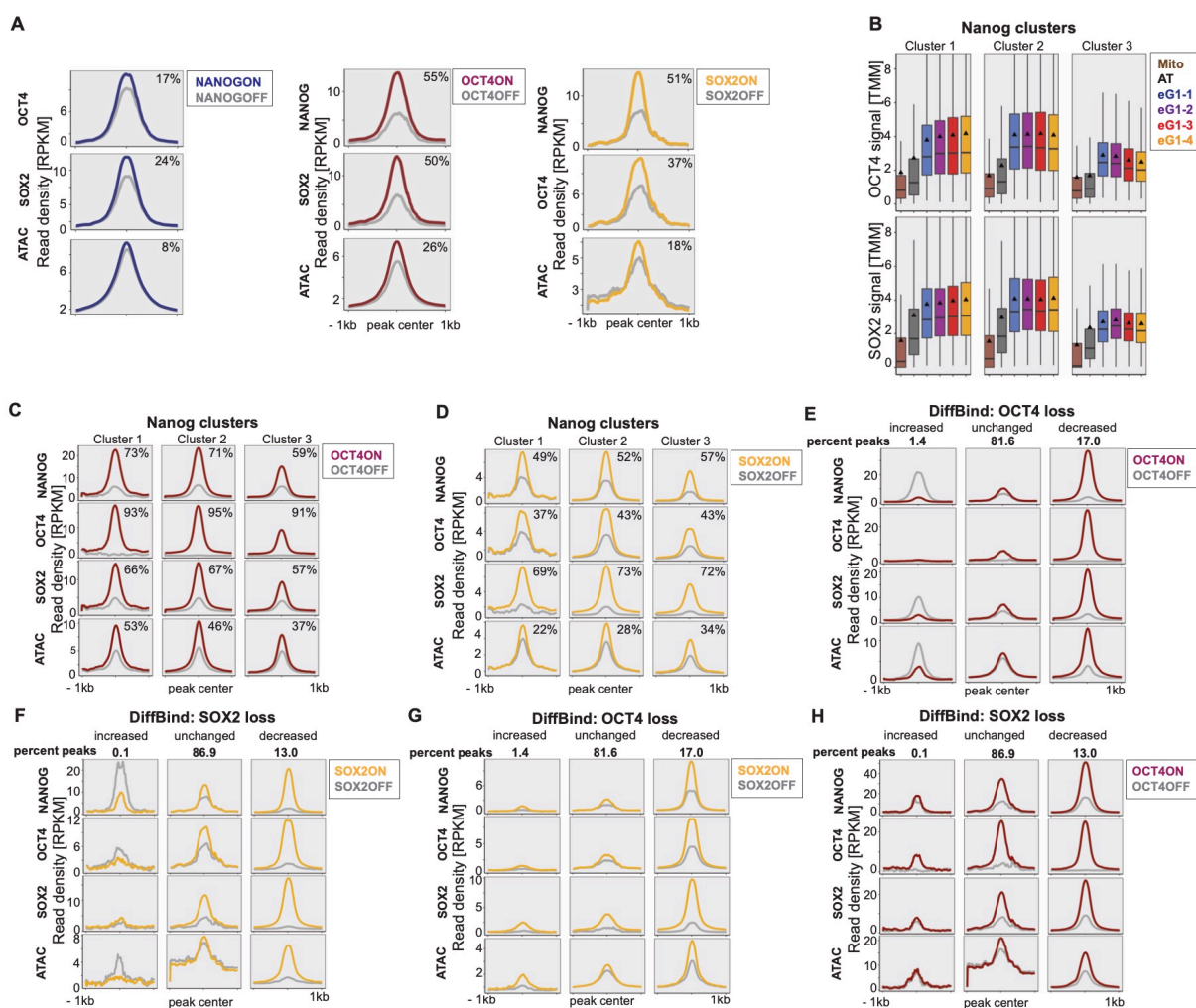


**Figure 6 The interaction between OCT4 and SOX2 with NANOG is locus-dependent.**

(A) RPKM-normalized read density of OSN and chromatin accessibility in NANOG<sup>cond</sup>, OCT4<sup>cond</sup>, or SOX2<sup>cond</sup> mESCs before and after 24 h doxycycline removal or treatment, or 26 h, respectively, centered around all OSN or merged peaks of the two TFs above (ATAC-seq). The percentage in the top right corner indicates the fold change between read enrichment in the presence or absence of the indicated TFs. (B) Boxplots of TMM-signal of OCT4 or SOX2 from mitosis to eG1-4 across all NANOG binding sites in Nanog clusters 1-3. Boxes: intervals between the 25th and 75th percentile. Horizontal lines: median; Triangles: mean; Error bars: 1.5-fold the interquartile range or

the closest data point when the data point is outside this range. (C-D) RPKM-normalized read density of OSN and chromatin accessibility in OCT4<sup>cond</sup> (C) or SOX2<sup>cond</sup> mESCs (D) before and after doxycycline treatment, centered around all NANOG sites of clusters 1, 2, or 3. Percentage in the top right corner: fold change between read enrichment in the presence or absence of the indicated TFs. (E-H) RPKM-normalized read density of OSN and chromatin accessibility in OCT4<sup>cond</sup> (E, H) or SOX2<sup>cond</sup> mESCs (F, G) before and after doxycycline treatment, centered around all NANOG loci that increase, maintain, or decrease NANOG binding upon OCT4 (E, G) or SOX2 loss (F, H). Percentage of loci that increase, maintain, or decrease binding from the total number of sites is indicated on top.

### 2.3.6 NANOG stabilizes OCT4 and SOX2 binding

While near-complete NANOG loss (Figure S5A) had only a mild effect on chromatin accessibility and on OCT4 and SOX2 binding (Figure 6A), we reasoned that NANOG may still strengthen OCT4 and SOX2 binding in naive PSCs. We found that 10.3 % and 12.9 % of loci only moderately decreased OCT4 or SOX2 binding in the absence of NANOG, respectively, and that a majority of these were common between for OCT4 and SOX2 (Figure 7A-B, Figure S5B, Table S4-5). Furthermore, the loci that increased OCT4 binding in the absence of NANOG decreased OCT4 binding in the absence of SOX2, whereas loci that increased SOX2 binding in the absence of NANOG remained unchanged in the absence of OCT4 (Figure 7C-D). Loci with increased OCT4 and SOX2 binding in the absence of NANOG also had a higher abundance of the SOX2 motif compared to those with decreased OCT4 and SOX2 binding (Figure S5C-D). This indicates that in the absence of NANOG, SOX2 redirects OCT4 to new loci and not the other way around. Loci that significantly decreased OCT4 or SOX2 binding upon NANOG loss were enriched for all four pluripotency motifs (Figure S5C-D), as well as for the GO terms pluripotency and embryo development (Figure S5E-F), consistent with the sustained self-renewal and increased susceptibility to differentiation resulting from NANOG depletion (Chambers et al., 2007). In summary, NANOG mainly stabilizes the binding of OCT4 and SOX2, and in its absence OCT4 is partially redirected by SOX2 to other loci.

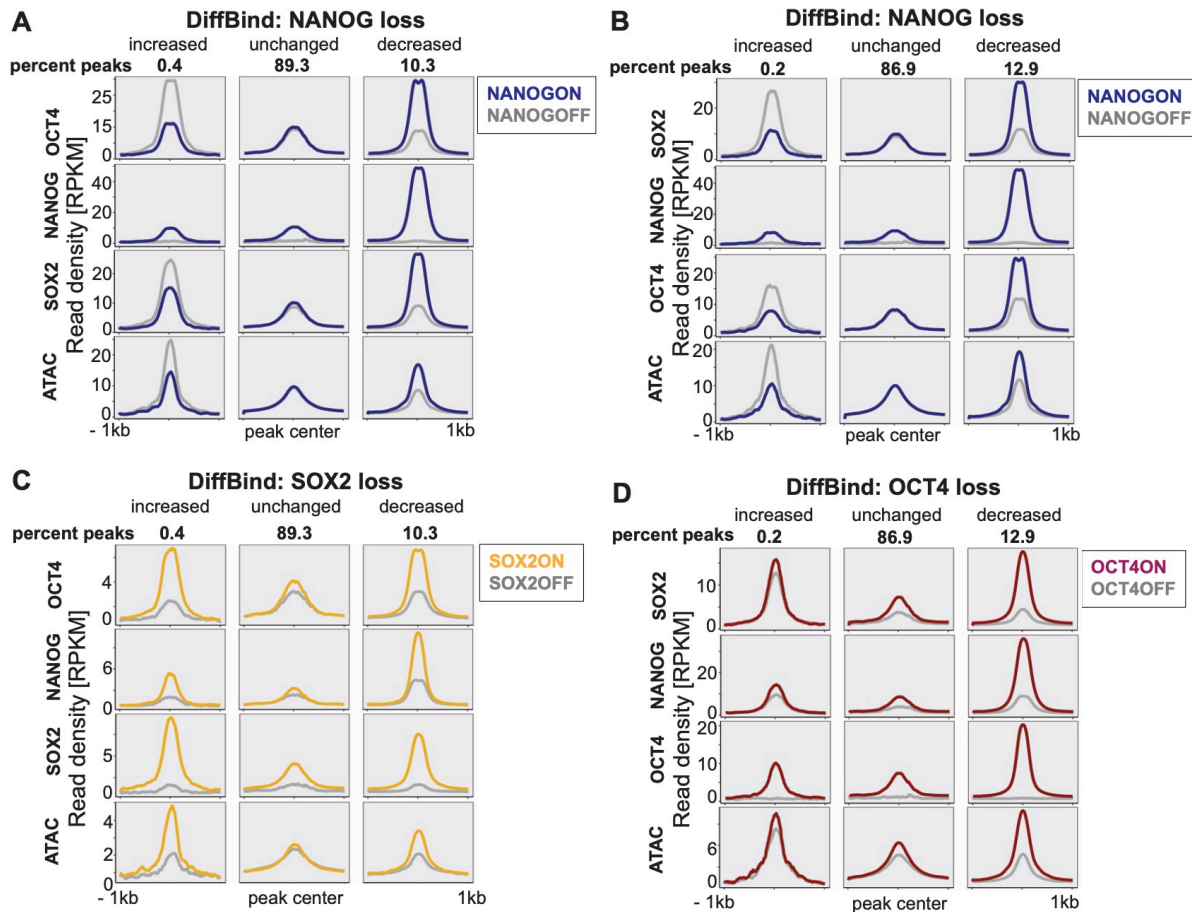


**Figure 7 NANOG loss redistributes OCT4 and SOX2.**

(A-D) RPKM-normalized read density of OSN and chromatin accessibility in NANOG<sup>cond</sup> (A, B), SOX2<sup>cond</sup> (C), and OCT4<sup>cond</sup> mESCs before and after 24 h doxycycline removal or treatment, or 26 h treatment, respectively, centered around all OCT4 (A, C) or SOX2 (B, D) loci that increase, maintain, or decrease NANOG binding.

### 2.3.7 OCT4 becomes increasingly important to maintain NANOG and SOX2 at pluripotency loci during naïve pluripotency exit

Finally, we asked whether the capacity of SOX2 to redirect NANOG binding in the absence of OCT4 is strengthened during exit of naïve pluripotency, during which SOX2 and NANOG may start to display functions more related to differentiation. To do so, we took advantage of a published dataset in which OCT4 was depleted in PSCs cultured in serum + LIF (SL) (King and Klose, 2017). Upon loss of OCT4, NANOG significantly gained and lost binding at 25 % and 8 % of its binding sites (Figure 8A, Table S4), respectively (Figure 6E). Most loci were common between different medium conditions (Figure 8B, Table S5), and increased NANOG binding was accompanied by an increase in SOX2 binding and chromatin accessibility (Figure 8A). Many loci that increased NANOG binding also significantly increased SOX2 binding (Figure 8C, Table S5) and were highly enriched in SOX2 motifs (Figure 8D). During development of the early blastocyst (E3.5), NANOG and SOX2 co-occupy sites with GATA6

at pre-endoderm and epiblast cis-regulatory elements (Thompson et al., 2022). We asked whether this co-occupancy is fostered in the absence of OCT4. Loci that significantly increased binding upon OCT4 loss were enriched for the GATA6 motif (Figure 8D) and in embryo development GO terms, while they were depleted in pluripotency GO terms (Figure 8E). Furthermore, using published GATA6 ChIP-seq (Wamaitha et al., 2015) acquired 36 h after Gata6 expression in mESCs, we found that GATA6 was more enriched at loci that increased compared to loci that decreased NANOG binding in the absence of OCT4 (Figure 8F-G). Altogether, our results suggest that during progression from naive to primed pluripotency, OCT4 plays an increasingly important role in maintaining NANOG and SOX2 binding at pluripotency regulatory elements and preventing their binding to loci involved in fostering further developmental stages.

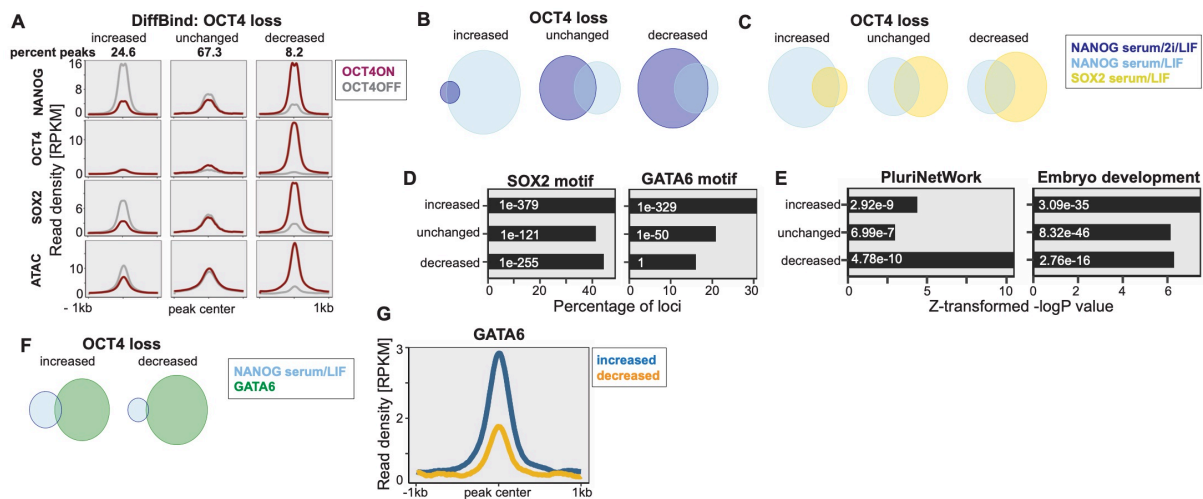


**Figure 8 OCT4 is required to maintain NANOG at pluripotency regulatory elements in PSCs cultured in serum + LIF.**

(A) RPKM-normalized read density of OSN and chromatin accessibility in OCT4<sup>cond</sup> mESCs grown in serum + LIF before and after 24 h doxycycline treatment centered around all NANOG loci that increase, maintain, or decrease NANOG binding. (B) Venn diagrams show the overlap between loci that significantly change NANOG binding upon OCT4 loss in serum/2i/LIF or serum/LIF. (C) Venn diagrams show the overlap between loci that significantly change NANOG or SOX2 binding upon OCT4 loss. (D) SOX2 and GATA6 motif enrichment and p-values (digits) at loci that significantly increase, maintain, or decrease NANOG in the absence of OCT4. (E) Relative enrichment values plotted as Z-transformed -logP value and p-values (digits) of GO terms PluriNetWork and Embryo development for loci that significantly increase, maintain, or decrease NANOG binding in the absence of OCT4. (F) Venn diagrams show the overlap between loci that significantly increase or decrease NANOG binding upon OCT4 loss with all GATA6 binding sites. (G) RPKM-normalized read density of the GATA6 signal centered around loci that increase or decrease NANOG binding in the absence of OCT4.

## 2.4 Discussion

Here we describe a drug synchronization-free approach to dissect the orchestration of TF binding, chromatin accessibility and transcriptional activity during mitotic exit. We show that the pluripotency network is quickly consolidated during mitotic exit, while TF binding events and mRNAs involved in differentiation are rapidly turned off.

Several studies using nocodazole-release approaches have reported a major spike in transcriptional activity when cells exit mitosis (Chervova et al., 2023; C-S Hsiung et al., 2016; Palozola et al., 2017). Here in contrast, we report that transcription is progressively ramping up during eG1. While we cannot exclude that cell type-specific differences contribute to these discrepancies, this raises the possibility of unphysiological transcriptional reactivation upon nocodazole release.

The decrease in site-specific binding of most TFs during mitosis is well-documented, but it was so far unclear how they dynamically re-establish their occupancy landscape during mitotic exit. Using unsynchronized cells, we confirmed that OSN are mostly evicted from specific binding sites during mitosis, as reported before in nocodazole-treated cells (Deluz et al., 2016; Festuccia et al., 2019). The rapid re-initiation of their genome-wide site-specific binding at the anaphase-telophase transition is consistent with the re-establishment of promoter-enhancer loops in this time window (Pelham-Webb et al., 2021; Zhang et al., 2019). We also found that OSN exhibit markedly distinct temporal rebinding patterns to the accessible genome. The pioneer TF SOX2 first explores accessible regions before relocating to more closed sites. In contrast, OCT4 becomes progressively relocated to more accessible regions of the genome during eG1. Since OCT4 has a strong, genome-wide pioneering activity in PSCs (Friman et al., 2019; King and Klose, 2017) this suggests that OCT4 is the main driver in re-establishing full post-mitotic chromatin accessibility at its binding sites. Like OCT4, NANOG also first explores inaccessible sites before being relocated to more accessible regions (Figure 9). However, NANOG depletion had only a minor impact on chromatin accessibility, in line with its lack of pioneering activity in mouse PSCs.

We also demonstrate the distinct roles of OCT4 and SOX2 in guiding NANOG and each other's binding. SOX2 can redirect NANOG or OCT4 to different genomic loci in the absence of OCT4 or NANOG, respectively. In contrast, OCT4 plays an invariable role in attracting SOX2 and NANOG towards pluripotency regulatory regions, independently of their respective expression. Our study thus reveals the diversity in which TFs adapt their binding landscape or recruit other TFs depending on the availability of their binding partners. Importantly, this also illuminates the temporal orchestration of TF binding during mitotic exit. In eG1-1, NANOG binding is biased towards differentiation-associated loci compared to later time points, with a higher dependence on the pioneering activities of SOX2 alone than OCT4 or both together.



This suggests that SOX2 has a larger impact on NANOG binding than OCT4 early during mitotic exit, which could be partly mediated by its stronger physical interaction with NANOG (Gagliardi et al., 2013; Mistri et al., 2022). In contrast, OCT4 alone and in cooperation with SOX2 progressively shifts the NANOG binding landscape towards globally more accessible and pluripotency-related regions (Figure 9). Since the co-localization of OSN does not substantially vary during eG1, the temporal changes in NANOG binding related to OCT4 and SOX2 are likely to be mostly indirectly mediated by their pioneering activity. These findings shed light on a brief post-mitotic temporal window during which the pluripotent TF binding landscape is not fully re-established yet, which may be involved in the increased sensitivity to differentiation during the mitosis-G1 transition (Coronado et al., 2013; Halley-Stott et al., 2014; Pauklin and Vallier, 2013).

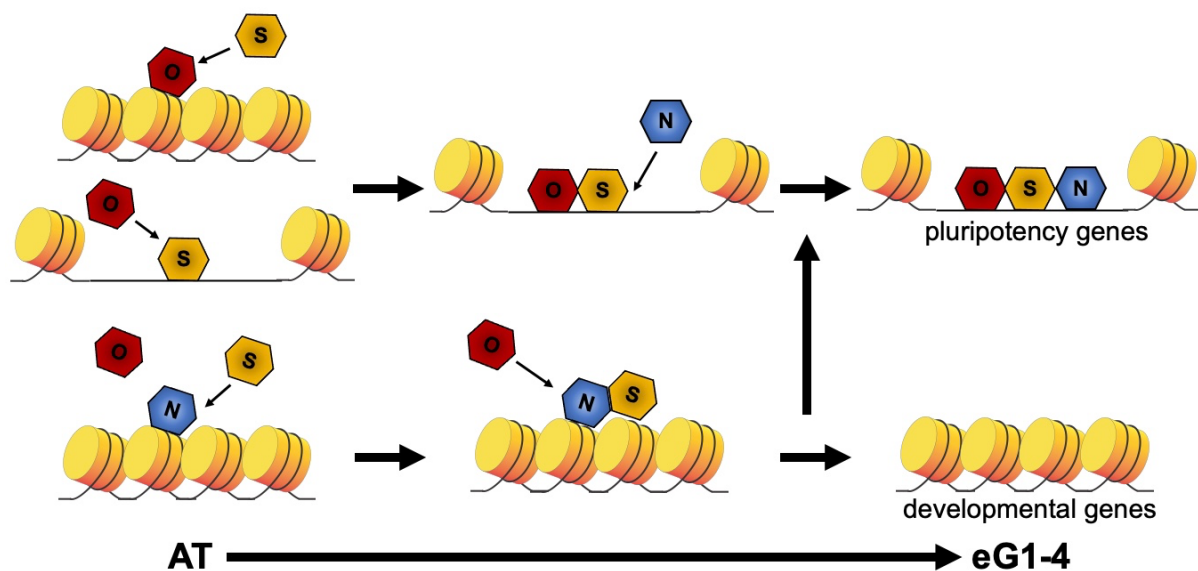


**Figure 9 Model for OSN rebinding during mitotic exit.**

Top: OCT4 binds during mitotic exit to inaccessible chromatin, while SOX2 initially prefers binding to accessible pluripotency genes. Bottom: During mitotic exit, when genome-wide TF binding is not fully reestablished yet, NANOG binds in the absence of OCT4 to inaccessible loci that are involved in development and more dependent on SOX2 to generate accessible chromatin before being relocated to pluripotency loci by OCT4.

## 2.5 Limitations of the study

Although the Cdt1-MD reporter system allowed us to efficiently distinguish between different temporal windows of eG1, the gate size had to be adjusted for each cell sorting experiment. Together with variability in ChIP-seq efficiency between each replicate this may contribute to the sawtooth aspect of the ChIP-seq signal in (Figure S2B). Thus, we decided to rely on TMM-normalized data for most of our quantitative analysis, focusing on relative, locus-specific changes in TF binding. However, although TMM allows us to overcome the technical limitation

of sample preparation, we cannot rule out that normalization masks some true changes in global TF occupancy. Furthermore, our AT-enriched cell population was only enriched for 32% of anaphase-telophase cells, and thus the overall signal from this population is likely to not truly reflect the full extent of OSN occupancy.

## 2.6 Acknowledgement

This study was funded by the Swiss National Science Foundation (grant# 310030\_184782). We thank the whole Gene Expression Core Facility from EPFL, especially Bastien Mangeat, Elisa Cora, and Lionel Ponsonnet, for next-generation sequencing and library preparation of the RNA-seq samples. We thank the Flow Cytometry Core Facility at EPFL, especially Miguel Garcia, Valérie Glutz, Francesco Palumbo, and André Mozes (former member) for cell sorting and provision of flow cytometry equipment. We thank the Bioimaging and Optics Platform and Biomolecular Screening Facility at EPFL for assistance with microscopes, SCITAS for cluster computing, Pablo Navarro for sharing 44iN cells with us, Armelle Tollenaere for helping with the collection of mitotic cells and for critical reading of the manuscript, and Lucas Jamar for helping with the linear regression.

## 2.7 Author contributions

Conceptualization, S.P. and D.S.; methodology, S.P. and D.S.; investigation, S.P. and L.V.; formal analysis, S.P. and D.S.; resources, D.S.; data curation, S.P.; writing – original draft, D.S. and S.P.; writing – review & editing, S.P., L.V. and D.S.; supervision, D.S.; funding acquisition, D.S.

## 2.8 Material and Methods

### 2.8.1 Cell culture

The CGR8 (ECACC 07032901), ZHBTc4 (Niwa et al., 2000), 2TS22C (Masui et al., 2007), and 44iN mouse embryonic stem cells lines (Festuccia et al., 2012) were routinely cultured on 0.1% gelatin-coated (Sigma, G9391) 100mm Petri dishes at 37°C and 5% CO<sub>2</sub> in GMEM (Sigma, G5154) supplemented with 10% inactivated ESC qualified fetal bovine serum (Gibco, 16141–079), 1% nonessential amino acids (Gibco, 11140–050), 2 mM L-glutamine (Gibco, 25030–024), 2 mM sodium pyruvate (Sigma, S8636-100ML), 100µM 2-mercaptoethanol (Sigma, M3148), 1% penicillin and streptomycin (BioConcept, 4–01F00-H), leukemia inhibitory factor (made in-house), 3 µM CHIR99021 (Merck, 361559) and 0.8 µM PD184352 (Sigma, PZ0181). Cells were split every 2-3 days based on their confluency by trypsinization (Sigma,

T4049). 44iN cells were kept in a medium containing 1 µg/ml doxycycline (Sigma, D3447). For ChIP-seq, ATAC-seq and RNA-seq experiments on the sorted cell populations of the Cdt1-MD cell line, cells were cultured for at least one week in a 1:1 mix of Neurobasal Medium (Gibco, 21103049) and DMEM/F-12 (Gibco, 21331020), supplemented with B-27 (Gibco, 17504044), N-2 (Gibco, 17502048), 2 mM L-glutamine (Gibco, 25030-024), 1% penicillin and streptomycin (BioConcept, 4-01F00-H), 100µM 2-mercaptoethanol (Sigma, 63689), 3 µM CHIR99021 (Merck, 361559), 1 µM PD184352 (Sigma, PZ0181), and leukemia inhibitory factor (in-house produced and validated for its capacity to maintain pluripotency). HEK 293T cells were cultured in DMEM with GlutaMAX (Gibco, 31966021) supplemented with 10% fetal bovine serum (Gibco, 10270106) and 1% penicillin and streptomycin (BioConcept, 4-01F00-H). To deplete OCT4 and SOX2 in the ZHBTc4 and 2TS22C cell lines, respectively, 10<sup>6</sup> cells were seeded in a 10cm dish and the next day, ZHBTc4 and 2TS22C cells were treated with 1 µg/ml doxycycline for 24 h or 26 h, respectively, before fixation. To deplete NANOG from 44iN cells, 10<sup>6</sup> cells were seeded in a 10cm dish in the presence of 1 µg/ml doxycycline, and the next day the medium was changed to leave cells in doxycycline-free medium for 24 h.

## 2.8.2 Plasmid construction

The lentiviral vector pLV-PGK-YPet-MD was previously generated in the Suter laboratory (Friman et al., 2019). For the construction of pLV-EF1a-mCherry-hCdt1(1/100)(Cy-), we inserted hCdt1(1/100)(Cy-) (Invitrogen, GeneArt Gene Synthesis) in fusion to mCherry in a pLV-EF1a-mCherry/PGK-Hygromycin vector by in-fusion cloning (Takara Bio, 639648).

## 2.8.3 Lentiviral vector production and stable cell line generation

HEK 293T cells were transfected with the psPAX2 (Addgene, 12260) envelope plasmid, the pMD2.G (Addgene, 12259) packaging plasmid (Dull et al., 1998), and pLV-PGK-YPet-MD or pLV-EF1a-mCherry-hCdt1(1/100)(Cy-) using calcium phosphate transfection (Suter et al., 2006). Two days after transfection, lentiviral vectors were concentrated by ultracentrifugation for 2 h at 20'000 g and 4°C. Subsequently, 50,000 mESCs plated in a 24-well plate in 1 ml of medium were transduced with 50 µl of concentrated pLV-EF1a-mCherry-hCdt1(1/100)(Cy-) lentiviral particles. mCherry-positive cells were selected with 200 µg/ml hygromycin B (Gibco, 10687010) for 10 days, and were subsequently transduced with pLV-PGK-YPet-MD viral particles. To generate a clonal cell line, single mCherry and YPet double-positive cells were sorted in individual wells of a 96-well plate and kept under selection with hygromycin. After clonal outgrowth, clones were further passages and one clone with high mCherry and YPet expression levels was selected as the final Cdt1-MD cell line.

## 2.8.4 Sorting of different cell cycle phases

Cells were stained in suspension with 40.5  $\mu$ M Hoechst 33342 (Thermo Fisher Scientific, H3570), and incubated for 20 min on a rotating platform at room temperature. The tube was filled with PBS + 1% FBS and spun down at 600 g for 5 min. For the sorting of different temporal bins in eG1, cells were fixed as described in the section “ChIP-seq”, resuspended in cold PBS + 1% FBS and sorted at 4°C based on their mCherry and YPet intensity in G1. Flow cytometry and FACS were performed on a LSR Fortessa (BD Biosciences) and on a FASCARIA Fusion (BD Biosciences), respectively. The gates were adjusted to obtain the same number of cells for each temporal bin. To obtain mitotic or telophase-anaphase enriched cells, cells were spun down at 450 g for 5 min at 4°C following fixation and Hoechst staining. Subsequently, cells were resuspended in 225  $\mu$ l PBS and permeabilized by adding 4.5 ml cold 70% EtOH (Fisher Scientific, 10342652) in PBS under vortex agitation and incubated for 15 min on ice with frequent inversion. Cells were then washed twice by resuspending them in PBS + 1% FBS, followed by centrifugation at 450 g for 5 min at 4°C. Following the second washing step, cells were resuspended in PBS + 10% FBS ES and the primary anti-H3S10p antibody (Millipore, 05-1336) was added at a dilution of 1:1000 and incubated for 90 min at 4°C in the dark. Cells were then washed twice with PBS + 1% FBS and centrifuged at 450 g for 5 min at 4°C. Subsequently, cells were resuspended in PBS + 10% FBS, the secondary antibody donkey anti-mouse IgG-AF647 (Invitrogen, A31571) was added at a dilution of 1:80, and cells were incubated for 45 min at 4°C in the dark. Finally, cells were washed twice with PBS + 1% FBS, centrifuged at 450 g for 5 min at 4°C, and resuspended in PBS + 1% FBS for FACS. The anaphase-telophase-enriched population was selected by gating for H3S10p+, mCherry-high, YPet-intermediate, and Hoechst-high cells. Mitotic cells were selected by gating for Hoechst-high and H3S10p+ cells. The data was analyzed using the FlowJo software (version 10.8.1). To obtain 1 million mitotic cells for OCT4 ChIP-seq from unsynchronized populations (Figure S2A), 580 Mio of CGR8 cells were plated into 145 T75 flasks. The next day, we used mitotic shake-off followed by sorting of H3S10p+ cells using FACS to purify mitotic cells.

## 2.8.5 ATAC-seq

ATAC-seq experiments were performed in biological duplicates for all sorted and unsorted cell populations. The experimental procedures were followed as previously described (Buenrostro et al., 2013). Briefly, 50,000 cells were sorted or collected after trypsinization. Cells were then pelleted at 800g for 5min at 4°C, washed once with cold PBS, and kept on ice. Subsequently, cells were resuspended in 50  $\mu$ l cold lysis buffer (10 mM Tris-HCl pH 7.4, 10 mM NaCl, 3 mM MgCl<sub>2</sub>, 0.1% NP-40), and centrifuged at 800g for 10min at 4°C. For the transposition reaction,

pelleted nuclei were resuspended in 50  $\mu$ l of 0.5  $\mu$ M Tn5 (in-house produced according to (Chen et al., 2017)) in TAPS-DMF buffer (10 mM TAPS-NaOH, 5 mM MgCl<sub>2</sub>, 10% DMF) and incubated at 37°C for 30 min. During the reaction, the tubes were flicked gently several times, and DNA was immediately purified using the DNA Clean & Concentrator kit (Zymo Research, D4003) with a binding buffer to sample ratio of 5:1. Transposed DNA was diluted in 10  $\mu$ l DNA elution buffer, and amplified in a solution containing 0.5 mM Ad1.1 universal primer, 0.5 mM of Ad2.X indexing primer, 0.6X SYBR Green I (Lonza, 59513) and 1X NEBNext High-Fidelity 2X PCR Master Mix (NEB, M0541L) at 72°C for 5 min, 98°C for 30 s, and 5 cycles of 98°C for 10 s, 63°C for 30 s, and 72°C for 1 min. The PCR reaction was monitored to stop the amplification before saturation by sampling 10  $\mu$ l of amplified DNA and analyzing it by qPCR (Applied Biosystems, 7900HT). The number of cycles to add was determined by the time at which the fluorescence was still in the rising phase. The remaining DNA was further amplified at 98°C for 30 s, and 4-7 cycles of 98°C for 10 s, 63°C for 30 s, and 72°C for 1 min. Next, the library was purified using the DNA Clean & Concentrator kit (Zymo Research, D4003) with a binding buffer-to-sample ratio of 5:1. The purified library was further size-selected using a 0.55X and 1.2X ratio of AMPure XP beads (Beckman Coulter, A63880). Library concentrations were determined by Qubit, analyzed on a fragment analyzer, and sequenced on an Illumina NextSeq 500 using 75 nucleotide read-length paired-end sequencing.

### 2.8.6 ChIP-seq

ChIP-seq experiments for Cdt1-MD cells in eG1-1 to eG1-4 on OCT4, and eG1-1 and eG1-3 for SOX2 were acquired in biological triplicates, the experiments on 50,000 cells in one biological replicate, and for the remaining samples biological duplicates were acquired. Briefly, cells were collected after trypsinization and fixed with 2 mM DSG (Thermo Scientific, 20593) in PBS for 50 min at room temperature on a rotating platform. Subsequently, cells were pelleted for 5 min at 600 g, and fixed for 10 min with 1 % formaldehyde (Thermo Scientific, PIER28906) on a rotating platform. The reaction was stopped using 200 mM Tris-HCl pH 8.0 (PanReac AppliChem, A4577) for 10 min on a rotating platform. Tubes were filled with 1 % FBS in PBS and cells were spun for 5 min at 600 g and 4°C. Fixed cells were either directly further processed or stained for cell sorting, as described in the “Sorting of different cell cycle phases” section. Nuclei were extracted by resuspending the cell pellet twice in LB1 (50 mM HEPES-KOH pH 7.4, 140 mM NaCl, 1 mM EDTA, 0.5 mM EGTA, 10% Glycerol, 0.5% NP-40 (Thermo Scientific, 85124), 0.25% Triton X-100), incubated for 10 min at 4°C and with gentle shaking at 100 rpm, and pelleted for 5 min at 4°C and 1700 g. The nuclei were then resuspended in LB2 (10 mM Tris-HCl pH 8.0, 200 mM NaCl, 1 mM EDTA, 0.5 mM EGTA), incubated for 10 min at 4°C and with gentle shaking at 100 rpm, and spun down for 5 min at

4°C and 1700 g. To wash nuclei, SDS shearing buffer (10 mM Tris-HCl pH 8.0, 1 mM EDTA, 0.15% SDS) was added twice without disturbing the pellet, the tube was rolled to rinse the walls and spun for 5 min at 4°C and 1700 g. All buffers were supplemented with a 1:100 dilution of protease inhibitor cocktail (Sigma, P8340). Chromatin was sheared for 20 min at 5% duty, 140 W, 200 cycles, or for samples with 50,000 cells for 10 min, 10% duty, 75 W, 200 cycles in a Covaris E220 focused ultrasonicator. To remove the insoluble material, chromatin was spun for 10,000 g for 5 min at 4°C and the supernatant was transferred to a new tube. As total input control and to evaluate the sonication efficiency, a few microliters of chromatin were incubated with 1X TE buffer pH 8.0 (PanReac AppliChem, A0386) and 10 ng/μl RNase A (Qiagen, 19101) at 37°C for 30 min. Proteinase K (Qiagen, 19131) was added at 400 ng/μl and the reaction was incubated for another 30 min at 55°C and shaking at 1100 rpm. Finally, 200 mM NaCl (Sigma, 59222C) was added to reverse the crosslinks at 65°C for 16 h and shaking at 1100 rpm. The chromatin was purified using a MinElute PCR purification kit (Qiagen, 28004) and quality-checked on a 1 % agarose gel (Invitrogen, 16500500). Next steps were performed using the ChIP-IT High Sensitivity kit (Active motif, 53040) with a few modifications highlighted below. For immunoprecipitation of samples made from at least 1 million cells, 3.5 μg chromatin were used unless stated otherwise, and for samples made from 50,000 cells, all extracted chromatin was used. The following antibodies were used: anti-OCT4A (Cell Signaling Technology, 5677S) at 3.1 μl per 3.5 μg chromatin, anti-SOX2 (Cell Signaling Technology, 23064) at 3.1 μl per 3.5 μg chromatin, and anti-NANOG (Cell Signaling Technology, 8822) at 1.55 μl per 3.5 μg chromatin. To obtain quantitative ChIP-seq results, drosophila spike-in chromatin (Active motif, 53083) and spike-in antibody (Active motif, 61686) were used according to the manufacturer's recommendations. Before binding the immunoprecipitated chromatin to the beads, the beads were washed once with ChIP buffer. For cross-link reversal, 2 μl proteinase K was added, the reaction was incubated at 55°C for 30 min and the temperature increased to 65°C and shaking at 1100 rpm for 16 h. Sequencing libraries were prepared using the NEBNext Ultra II DNA Library Prep Kit (NEB, E7645L), and sequenced on a NextSeq 500 using 75-nucleotide read length paired-end sequencing.

### 2.8.7 Nuclear RNA-seq

Nuclear RNA-seq was done in biological duplicates on the four sorted temporal bins of eG1. Upon sorting, cells were spun down at 600 g for 5 min at 4°C, and nuclei were isolated following the low cell input nuclei isolation protocol of the 10x protocol for cell lines and PBMCs ([https://assets.ctfassets.net/an68im79xiti/6t5iwATCRaHB4VWOJm2Vgc/bdfd23cdc1d0a321487c8b231a448103/CG000365\\_DemonstratedProtocol\\_NucleiIsolation\\_ATAC\\_GEX\\_Sequencing\\_RevB.pdf](https://assets.ctfassets.net/an68im79xiti/6t5iwATCRaHB4VWOJm2Vgc/bdfd23cdc1d0a321487c8b231a448103/CG000365_DemonstratedProtocol_NucleiIsolation_ATAC_GEX_Sequencing_RevB.pdf)). Briefly, cells were resuspended in 500 μl lysis buffer composed of 10 mM

Tris pH 7.4, 10 mM NaCl, 3 mM MgCl<sub>2</sub>, 1% BSA (Merck, B9000S), 0.1% Tween (Fisher Scientific, 10113103), 1 mM DTT (Merck, 646563), 0.5U/μl Rnase inhibitor (Merck, 3335402001), 0.1% NP-40, and 0.01% Digitonin (Invitrogen, BN2006). After incubation for 5 min on ice, 500 μl wash buffer was added (same as lysis buffer but without NP-40 and digitonin) and nuclei were spun down at 450 g for 5 min at 4°C. The washing step was repeated for a total of three times. RNA extraction was done using the RNeasy Plus Micro Kit (Qiagen, 74034) with the following adjustments. Nuclei were resuspended in 350 μl lysis buffer comprising 40 mM DTT. Upon gDNA elimination, the samples were washed with ethanol and transferred to the RNeasy MinElute column. Next, 350 μl of RW1 buffer was added, and samples were spun at 8000 g for 30 s. The flow-through was discarded and a mix of 70 μl buffer RDD with 10 μl DNase (Qiagen, 79254) was added to the columns. 15 minutes later, 350 μl buffer RW1 was added to the columns and the manufacturer's protocol was followed. Sequencing libraries were prepared using the NEBNext Ultra II Directional RNA Library Prep Kit for Illumina (NEB, E7760S), and sequenced on a NextSeq 500 using 75-nucleotide read length paired-end sequencing.

### 2.8.8 Immunofluorescence microscopy

Cells were plated in a 96-well plate pre-coated for 2 h at 37°C with 1:10 diluted Biolamina (BioLamina, LN511-0202) in DPBS (Gibco, 14040091). The next day, 1 μg/ml doxycycline was added to ZHBTC4 or 2TS22C cells or removed from 44iN cells to deplete the corresponding TF for 24 h (ZHBTC4 and 44iN cells) or 26 h (2TS22C cells). Cells were then fixed with 2% formaldehyde in DPBS for 30 min at room temperature, washed with DPBS, and permeabilized with 0.5 % Triton X-100 in DPBS for 30 min at room temperature. After two washes with DPBS, cells were blocked for 30 min at room temperature with 1 % BSA in DPBS. The anti-Nanog antibody (CST, 8822) was added at 1:1000 dilution in a blocking solution, and the plate was incubated overnight at 4°C. After two washes with DPBS, the secondary anti-rabbit IgG AF647 antibody (Invitrogen, A-21443) was added at a dilution of 1:1000 in blocking solution for 1 h at room temperature in the dark. Cells were washed twice with 0.1 % Tween 20 in DPBS, then twice with DPBS, and Fluoromount G with DAPI (SouthernBiotech, 0100-20) was added and incubated for 10 min before imaging. The plate was imaged on an IN Cell Analyzer 2200 (GE Healthcare). Images were analyzed using CellProfiler (Carpenter et al., 2006). Nuclei were identified by area shape and size on the DAPI channel, and the integrated fluorescence intensity in the NANOG channel was measured in cell nuclei.

### 2.8.9 Time-lapse imaging

Cdt1-MD cells were plated on a 96-well plate coated for 1h at 37°C with StemAdhere (Primorigen Biosciences, S2071) diluted 1:25 in DPBS. The medium was then exchanged for phenol red-free FluoroBrite DMEM (Gibco, A1896701) supplemented with 10% inactivated ESC qualified fetal bovine serum (Gibco, 16141-079), 1% nonessential amino acids (Gibco, 11140-050), 2 mM L-glutamine (Gibco, 25030-024), 2 mM sodium pyruvate (Sigma, S8636-100ML), 100µM 2-mercaptoethanol (Sigma, M3148), 1% penicillin and streptomycin (BioConcept, 4-01F00-H), leukemia inhibitory factor (made in-house), 3 µM CHIR99021 (Merck, 361559) and 0.8 µM PD184352 (Sigma, PZ0181), and cells were imaged on an Operetta CLS (PerkinElmer) for 16 h every 15 min. To quantify YPet and mCherry signals, images were background-subtracted in Fiji (Schindelin et al., 2012) using a rolling ball radius of 50 pixels. The mean cell and background signal were tracked manually by maintaining the size of the region of interest over time. Signal measurements were started from the last timepoint before cell division, and one sister cell was followed for 5 h (21 frames). This captures the whole G1 phase in our Cdt1-MD cell line, as we determined by the average cell cycle length and the percentage of G1 cells. To obtain the integrated fluorescence intensity of individual cells, the background was subtracted from the mean fluorescence intensity multiplied by the area of the cell.

### 2.8.10 Calculation of the post-cytokinesis time in the different temporal bins of eG1

To obtain the post-cytokinesis time of the eG1 bins, we extracted all measurements of the time-lapse imaging that were measured between timepoint 0 and 2 h since these correspond to the early timepoints of G1 based on the average plots of mCherry and YPet intensity and flow cytometry. Subsequently, we used scikit-learn (Buitinck et al., 2013) to model a linear regression line to cluster the data points into four equal-sized clusters with the most equal distribution in 2D. We extracted the data points and plotted them using ggplot (Wickham, 2016).

### 2.8.11 Sequencing data analysis

Sequencing libraries were aligned to the *Mus musculus* mm10 genome (GRCm38 release M25) and to the *Drosophila Melanogaster* genome (BDGP6 release 28) using STAR 2.7.0e (Dobin et al., 2013). Duplicated reads were removed with Picard (Broad Institute), and indexed using SAMTools 1.10 (Li et al., 2009). CHIP-seq samples were spike-in-normalized based on the sample with the lowest abundance of *Drosophila* reads (Bonhoure et al., 2014; Orlando et



al., 2014) using SAMTools. For replicates, bam files were merged using SAMTools, and BigWig files were computed using the deepTools 3.5.1 (Ramírez et al., 2016) function bamCoverage with the setting "--normalizeUsing RPKM". Peaks were called using MACS 2.2.4 (Zhang et al., 2008) with settings "-f BAMPE -g mm", and merged using awk. Blacklisted peaks (Dunham et al., 2012) were removed with BEDTools (Quinlan and Hall, 2010) using the setting "-v".

The deepTools function computeMatrix with the setting "reference-point" was used to compute a matrix containing a score per genomic region. This matrix file was subsequently used together with the deepTools function plotHeatmap, and for average line plots with custom R code and the package ggplot2 (Wickham, 2016). The deepTools function multiBigWigSummary with the setting "BED-file" was used to calculate read counts per peak region and used together with ggplot2 to generate violin or box plots. BEDOPS (Neph et al., 2012) and BEDTools were used to merge and intersect different peak files, respectively. The deepTools function bigwigCompare with the setting "--operation subtract" was used to subtract BigWig files, or to obtain the quotient between two BigWig files using the setting "--operation ratio". To upscale the mitotic and anaphase-telophase enriched samples, BigWig files were multiplied by the ratio between the 1 Mio and 50,000 cell sample of the corresponding eG1-1 files using IGB (Freese et al., 2016) and the resulting bedgraph files merged using the Unix command "cat". The bedgraph files were converted to BigWig files using bedGraphToBigWig (Kent et al., 2010). To plot the subtracted tracks and multiplied BigWig files against the peaks, peaks were trimmed to 200 bp around the peak center using the HOMER2 function annotatePeaks.pl with the setting "-size 200" and the commands awk and tail. This trimming was performed to eliminate variability in peak signals emerging from differences in fragment sizes between samples. To identify the features of the OSN binding sites, target peaks were overlapped with ESC\_J1 enhancer peaks from EnhancerAtlas (Gao and Qian, 2020) using BEDTools. For promoters, all TSS from the mm10 genome were extracted and enlarged by 1 kb upstream and 500 bp downstream, and also crossed with the target peaks using BEDTools. The remaining peaks were classified as other. TF clusters were obtained by calculating the log2fold change between different temporal bins of eG1 and eG1-1, and using the R function pheatmap with the settings "clustering\_distance\_rows = "euclidean", kmeans\_k = 3". For the comparative analysis of TF binding in the presence or absence of another TF, DiffBind (Stark and Brown, 2011) was used with settings for dba.count "minOverlap = 2", and only peaks with an FDR < 0.05 were kept. To obtain intronic or exonic reads from the total RNA-seq reads, we used SAMTools view. In the clusters of the RNA-seq data (Figure 3C), we only considered genes with at least one value over 0 for the intronic or exonic reads. However, for intron and exon plots (Figure 3B), all exons or all introns, respectively, were used.

### 2.8.12 Motif and gene ontology analysis

For motif search, peak files were subjected to the HOMER2 (Heinz et al., 2010) function findMotifsGenome.pl with the setting “-size given”. We plotted the known motif and p-value of the target regions, and the background which is the mean of the estimated background frequency in all groups. Motif strength was calculated using FIMO (Grant et al., 2011) with the setting “--thresh 0.001” and motifs UN0383.1, MA1115.1, MA0142.1, and MA0143.1 were downloaded from JASPAR (Sandelin et al., 2004). For GO enrichment, the closest TSS to each peak was used for gene annotation either by using the R package ClusterProfiler (Wu et al., 2021; Yu et al., 2012) or for a functional analysis of enhancer-gene interactions from EnhancerAtlas by overlapping ESC\_J1 peaks with the target peaks. The enrichment was calculated with findGO.pl from HOMER2 with the setting “mouse”, and plotted together with the Z-transformed -logP values.

### 2.8.13 TMM normalization

For TMM normalization (Robinson and Oshlack, 2010), a peak file containing a list of all consensus peaks of OCT4, SOX2, and NANOG was generated using BEDOPS with the setting “-m”. The BED file was subsequently converted into the SAF format using awk, and a count matrix containing the information of all BAM files of interest was generated using featureCounts (Liao et al., 2014). Normalization factors were calculated using edgeR (Robinson et al., 2009), multiplied by the total library size, and divided by  $10^6$  to scale to reads per million. Normalized BigWig files were computed using the tool bamCoverage of deepTools 3.5.1 with the settings “--scaleFactor” and “-bs 1”.

### 2.8.14 Published datasets

Published data were downloaded from GEO (Edgar et al., 2002) and processed as described in the section “Data analysis for sequencing data”. ATAC-seq and ChIP-seq data from ZHBTc4 cells grown in serum/LIF conditions (GSE87822) (King and Klose, 2017), from 2TS22C cells (GSE134680) (Friman et al., 2019), and GATA6 ChIP-seq (GSE69323) (Wamaitha et al., 2015) were taken from previous studies. OCT4-, SOX2- and Co-dependent regions are coming from a previous study (Friman et al., 2019).

## 2.8 Supplementary figures

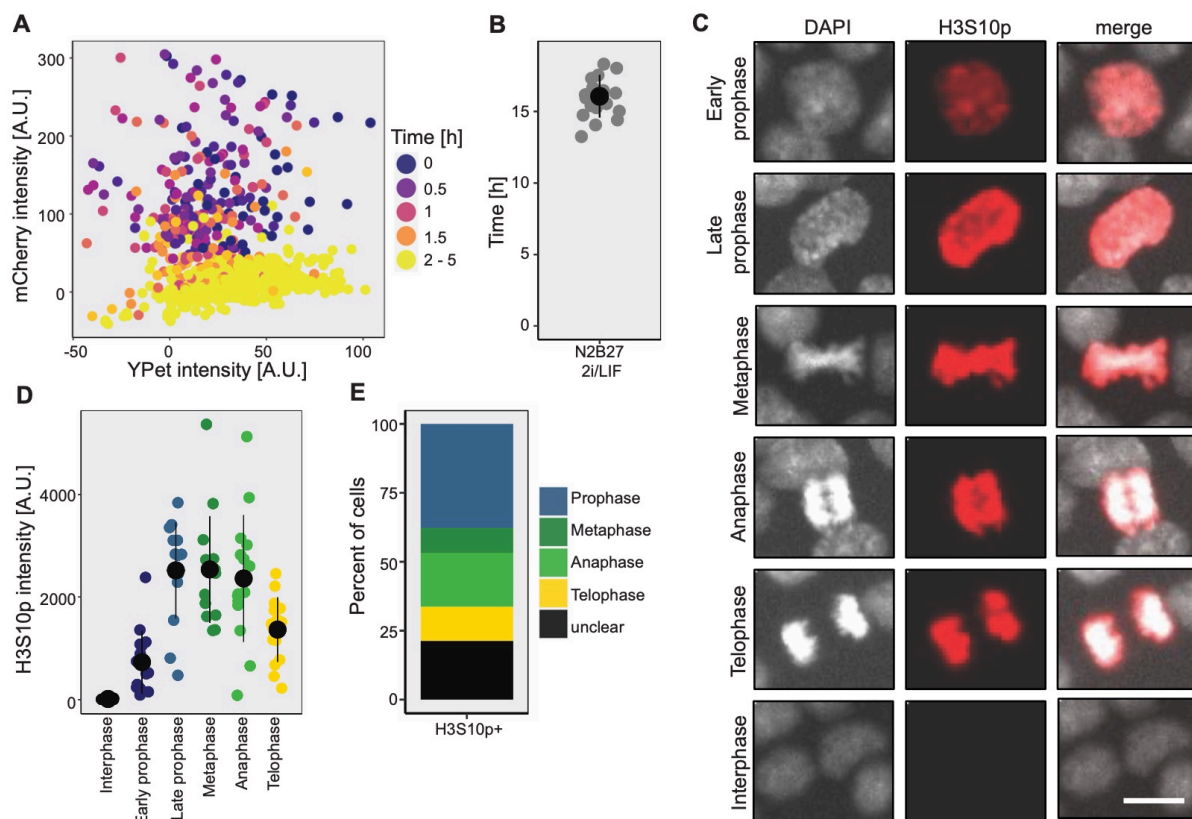


**Figure S 1 – related to Figure 2: Measurements of mESCs expressing the Cdt1-MD reporter in early G1 and quantification of the H3S10p signal in mitotic cells.**

(A) Integrated fluorescence intensities of mCherry and YPet for each of the 20 time points of 40 cells measured over 5h after cytokinesis. (B) Duration of the cell cycle for 20 mESCs grown in N2B27 2i/LIF. Black dot: mean. Error bar: SD. (C) Representative Images and (D) immunofluorescence quantification of H3S10p signal of 15 cells per mitotic phase. Prophase was subdivided based on observed changes in chromatin condensation. Black dots: mean; Error bars: SD. Scale bar: 10  $\mu$ m. (E) Cdt1-MD cells were sorted to be mCherry-high, YPet-intermediate, Hoechst-high, and H3S10p-positive, imaged, and the number of cells in each mitotic phase was counted.

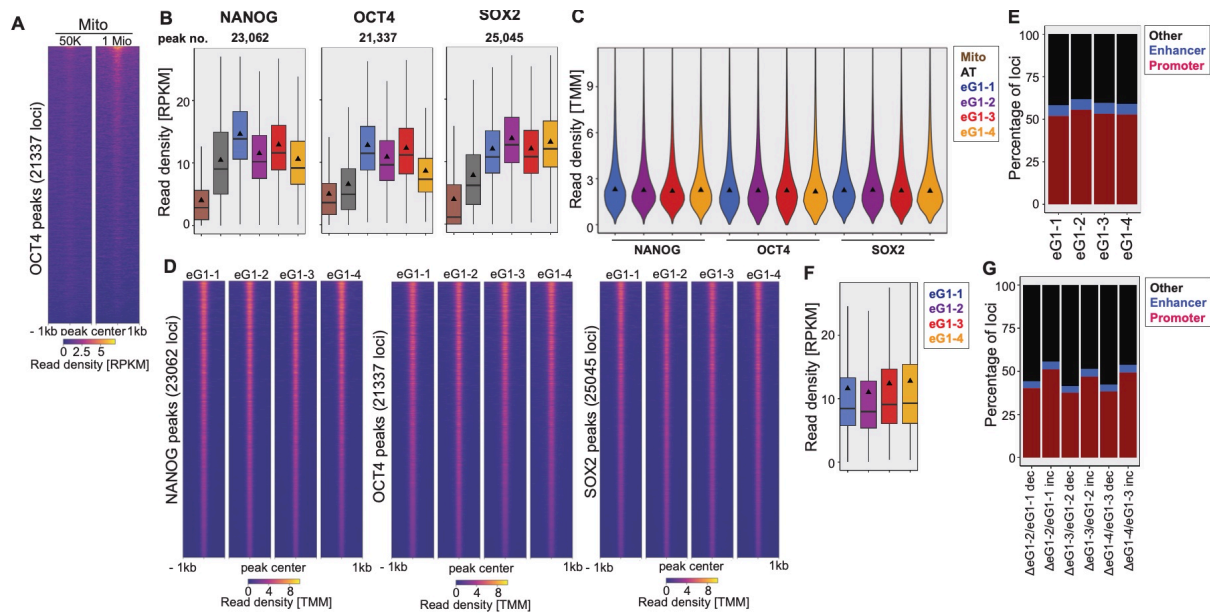


**Figure S 2 – related to Figure 4: TMM-normalization of ChIP-seq data and signal quantification of track-subtracted loci.**

(A) Heatmap of spike-in and RPKM-normalized ChIP-seq data on OCT4 in mitosis on 50,000 or 1 Mio unsynchronized cells on all consensus peaks of OCT4 from mitosis to eG1-4. Signals are ranked by intensity, and each row represents one locus. (B) Boxplots of spike-in and RPKM-normalized ChIP-seq data on OSN in mitosis (Mito), AT-enriched cells (AT), and different temporal bins of eG1. Mitotic and AT reads were scaled based on the difference between the number of reads in eG1-1 on 1 Mio and 50,000 cells (see STAR Methods). Triangles: mean. (C) Violin plots of the TMM-normalized reads of OSN in different temporal bins of eG1 after TMM-normalization on the reference peaks. Triangles: median. (D) Heatmaps of TMM-normalized ChIP-seq data on OSN in different temporal bins of eG1 1kb around all consensus peaks of each respective TF from mitosis to eG1-4. Signals are ranked by intensity, and each row represents one locus. (E) Overlap of ATAC-seq peaks with active enhancers and promoters. (F) Boxplots of RPKM-normalized ATAC-seq data in different temporal bins of eG1. (G) Overlap of  $\Delta$ RPKM track subtracted-ATAC-seq peaks with active enhancers and promoters at different time points of eG1. For boxplots: Boxes: intervals between the 25th and 75th percentile. Horizontal lines: median; Triangles: Mean; Error bars: 1.5-fold the interquartile range or the closest data point when the data point is outside this range.

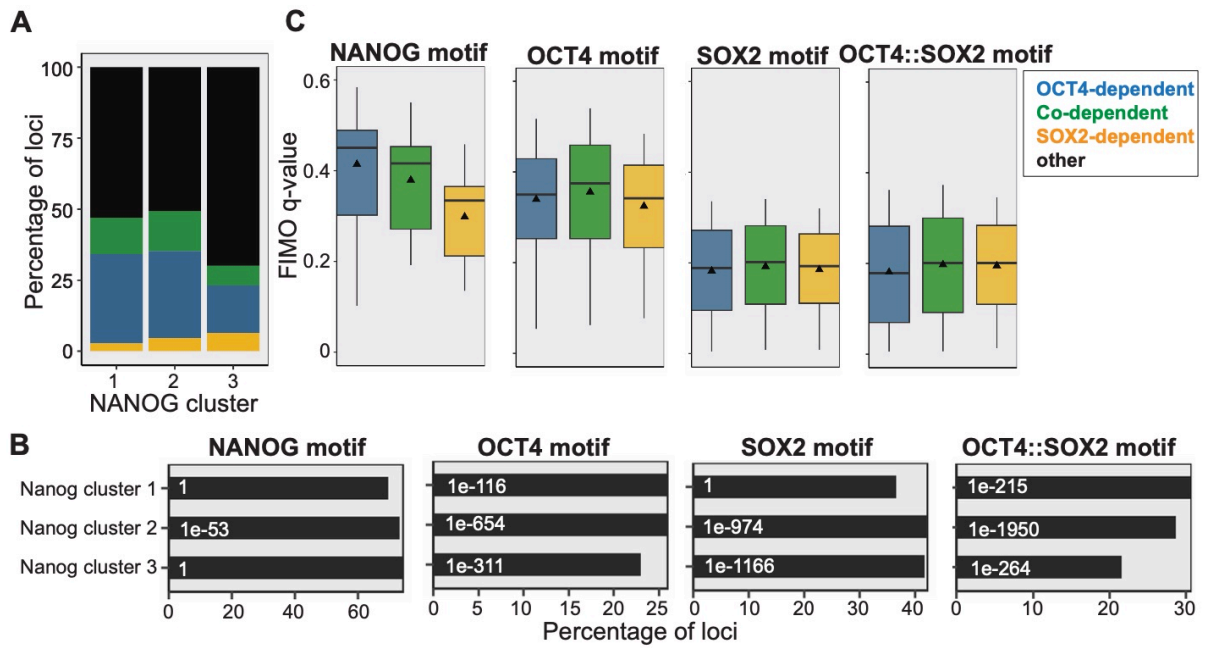


**Figure S 3 – related to Figure 5 and 6: Additional characterization of OSN binding upon mitotic exit and Nanog cluster 1-3.**

(A) Overlap between the binding sites of the different Nanog clusters with OCT4-, SOX2-, and Co-dependent loci as defined in (Friman et al., 2019). The remaining sites were classified as other. Percentages were calculated based on the total number of peaks in each cluster. (B) NANOG, OCT4, SOX2, and OCT4::SOX2 motif enrichment and p-value (white digits) in Nanog cluster 1-3. (C) NANOG, OCT4, SOX2, and OCT4::SOX2 motif quality based on FIMO q-value in Nanog cluster 1-3. Boxes: intervals between the 25th and 75th percentile. Horizontal lines: median; Triangles: mean; Error bars: 1.5-fold the interquartile range or the closest data point when the data point is outside this range.

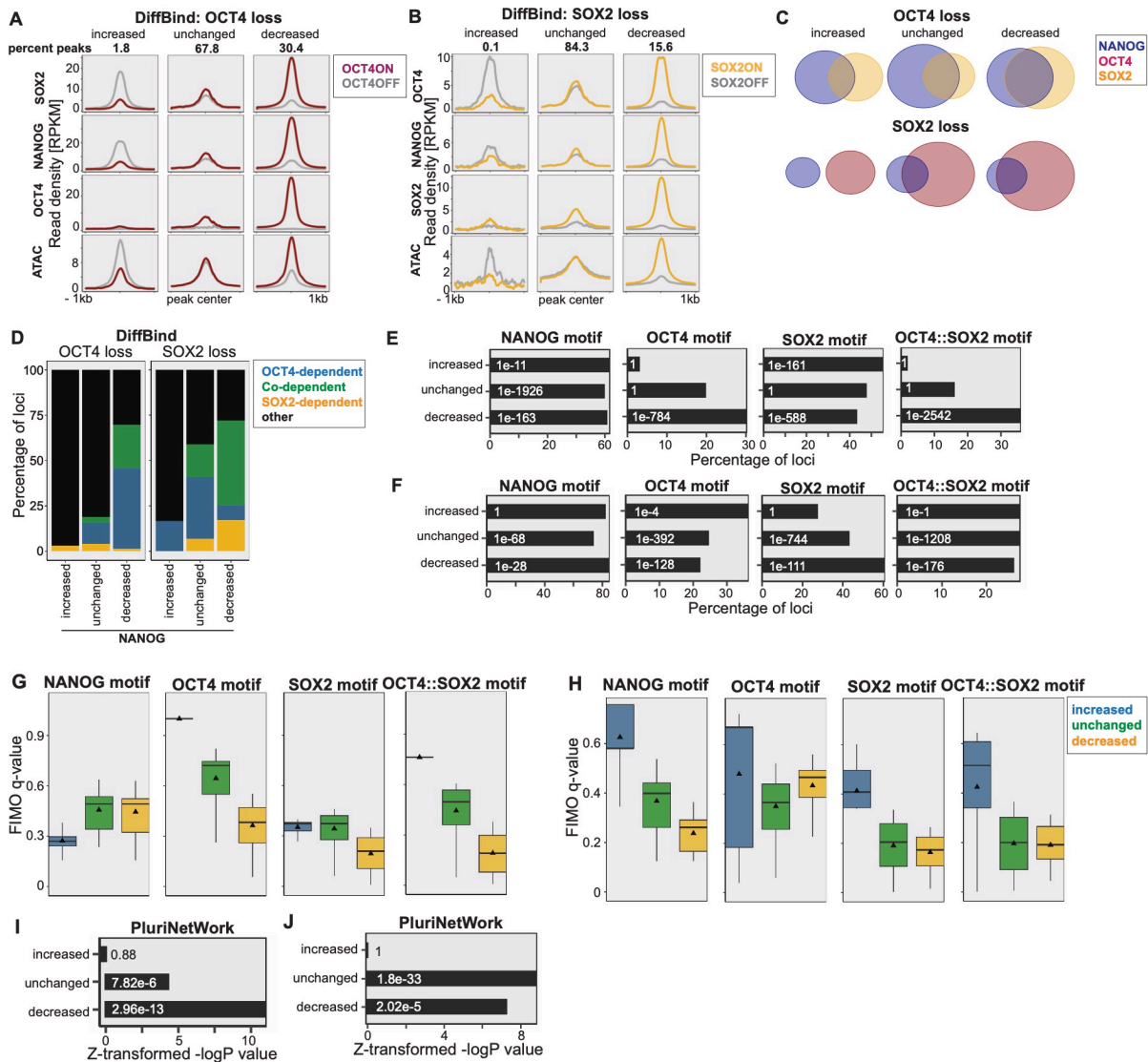


**Figure S 4 – related to Figure 6: Additional characterization of significantly affected loci in the absence of OCT4 or SOX2.**

(A-B) RPKM-normalized read density of OSN and chromatin accessibility in OCT4<sup>cond</sup> (A) or SOX2<sup>cond</sup> mESCs (B) before and after 24 h doxycycline treatment, or 26 h, respectively, centered around all SOX2 or OCT4 loci that increase, maintain or decrease SOX2 or OCT4 binding. (C) Venn diagrams show the overlap between loci that significantly change NANOG or SOX2 binding upon OCT4 loss or NANOG and OCT4 binding upon SOX2 loss, respectively. (D) Overlap of the binding loci that significantly increase, maintain, or decrease NANOG in the absence of OCT4 or SOX2 with OCT4-, SOX2-, and Co-dependent loci. (E-F) NANOG, OCT4, SOX2, and OCT4::SOX2 motif enrichment and p-value (digits) at loci that significantly increase, maintain, or decrease NANOG in the absence of OCT4 (E) or SOX2 (F). (G-H) NANOG, OCT4, SOX2, and OCT4::SOX2 motif quality based on FIMO q-value at loci that significantly increase, maintain, or decrease NANOG binding in the absence of OCT4 (G) or SOX2 (H). Boxes: intervals between the 25th and 75th percentile. Horizontal lines: median; Triangles: mean; Error bars: 1.5-fold the interquartile range or the closest data point when the data point is outside this range. (I-J) Relative enrichment values plotted as Z-transformed -logP value and p-values (digits) of the GO terms PluriNetWork and Embryo development for loci that significantly increase, maintain, or decrease NANOG in the absence of OCT4 (I) or SOX2 (J).

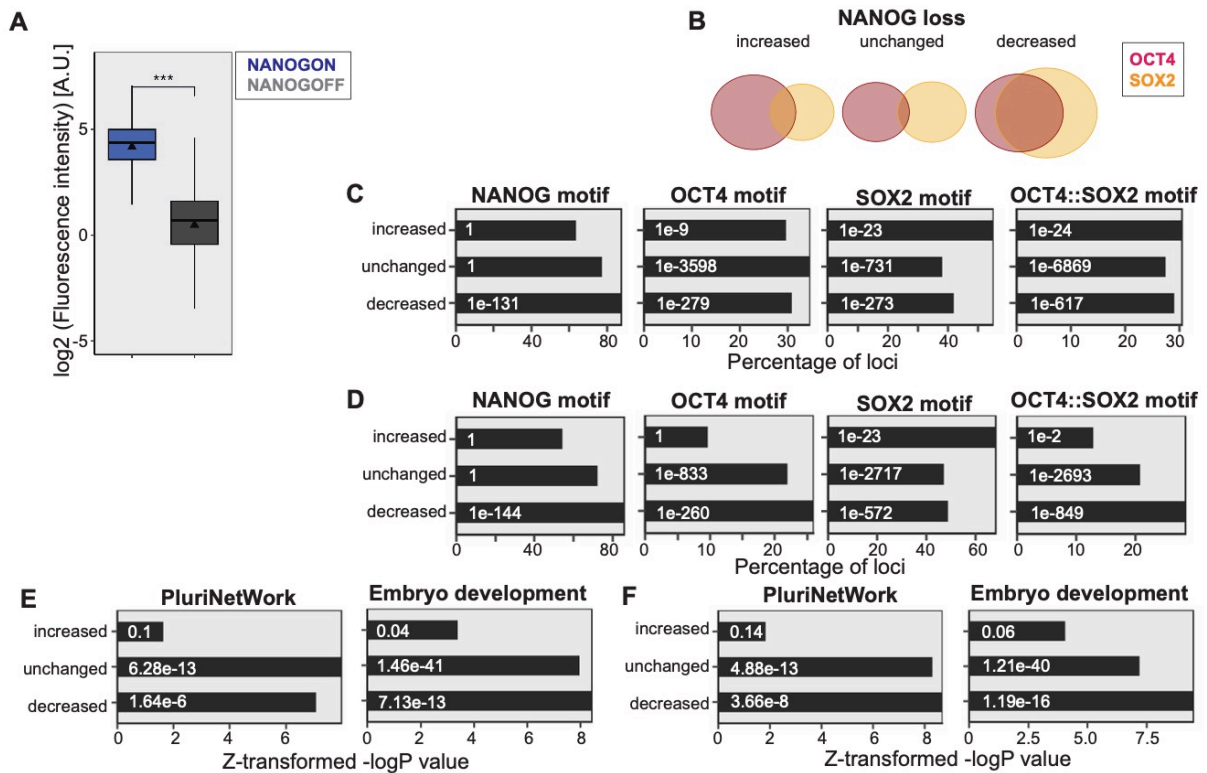


**Figure S 5 – related to Figure 7: Additional characterization of significantly affected loci in the absence of NANOG.**

(A) Quantification of the immunofluorescence on NANOG before and after doxycycline removal for 24 h. Boxes: intervals between the 25th and 75th percentile. Horizontal lines: median; Triangles: mean; Error bars: 1.5-fold the interquartile range or the closest data point when the data point is outside this range. (B) Venn diagrams showing the overlap between loci that significantly change OCT4 or SOX2 binding upon NANOG loss. (C-D) NANOG, OCT4, SOX2, and OCT4::SOX2 motif enrichment and p-values (digits) at loci that significantly increase, maintain or decrease OCT4 (C) or SOX2 (D) binding in the absence of NANOG. (E-F) Relative enrichment values plotted as Z-transformed -logP value and p-values (digits) of GO terms PluriNetWork and Embryo development for loci that significantly increase, maintain, or decrease OCT4 (E) or SOX2 (F) in the absence of NANOG.

## 2.9 Supplementary tables

**Table S 1 Genes of RNA-seq clusters 1 and 3.**

Cluster 1			Cluster 3		
ENSMUST00000131494.7	ENSMUST00000163723.7	ENSMUST00000084343.3	ENSMUST00000119612.8	ENSMUST00000228489.1	ENSMUST00000133533.7
ENSMUST00000125294.8	ENSMUST00000016768.11	ENSMUST00000147292.7	ENSMUST00000115480.7	ENSMUST00000075317.11	ENSMUST00000152159.7
ENSMUST00000170146.2	ENSMUST00000230286.1	ENSMUST00000071972.10	ENSMUST00000188454.6	ENSMUST00000226766.1	ENSMUST00000138795.7
ENSMUST00000162751.7	ENSMUST00000124011.1	ENSMUST00000000087.12	ENSMUST00000047577.6	ENSMUST00000226496.1	ENSMUST00000141883.7
ENSMUST00000027065.11	ENSMUST00000138134.7	ENSMUST00000062990.3	ENSMUST00000115367.7	ENSMUST00000183910.1	ENSMUST00000115451.7
ENSMUST00000149737.7	ENSMUST00000042818.10	ENSMUST00000199525.1	ENSMUST00000026881.10	ENSMUST00000226440.1	ENSMUST00000115421.2
ENSMUST00000162599.7	ENSMUST00000109309.8	ENSMUST00000123368.7	ENSMUST00000150457.1	ENSMUST00000226433.1	ENSMUST00000003720.4
ENSMUST00000160855.1	ENSMUST00000000109.10	ENSMUST00000030585.7	ENSMUST00000063663.5	ENSMUST00000179393.7	ENSMUST00000101581.9
ENSMUST00000194195.5	ENSMUST00000189291.6	ENSMUST00000132251.1	ENSMUST00000193138.1	ENSMUST00000170127.8	ENSMUST00000161356.7
ENSMUST00000027287.10	ENSMUST00000180852.1	ENSMUST00000052090.8	ENSMUST00000189878.1	ENSMUST00000077273.8	ENSMUST00000197992.1
ENSMUST00000041815.14	ENSMUST00000023119.14	ENSMUST00000219402.2	ENSMUST00000027298.4	ENSMUST00000025356.3	ENSMUST00000196406.1
ENSMUST00000056815.8	ENSMUST00000229471.1	ENSMUST00000121571.7	ENSMUST00000170295.7	ENSMUST00000228229.1	ENSMUST00000134633.1
ENSMUST00000181660.7	ENSMUST00000229352.1	ENSMUST00000183998.1	ENSMUST00000088072.9	ENSMUST00000110230.7	ENSMUST00000171190.1
ENSMUST00000179766.2	ENSMUST00000183449.1	ENSMUST00000105806.1	ENSMUST00000181756.2	ENSMUST00000110217.9	ENSMUST00000002708.4
ENSMUST00000027217.8	ENSMUST00000023750.8	ENSMUST00000042844.6	ENSMUST00000008280.13	ENSMUST00000182476.7	ENSMUST00000020399.1
ENSMUST00000156876.7	ENSMUST00000023754.5	ENSMUST00000038749.10	ENSMUST00000027217.8	ENSMUST00000190433.1	ENSMUST00000114747.8
ENSMUST00000009496.6	ENSMUST00000075420.5	ENSMUST00000094526.4	ENSMUST00000061421.3	ENSMUST00000023260.4	ENSMUST00000020280.1
ENSMUST00000188040.1	ENSMUST00000181034.2	ENSMUST00000154592.7	ENSMUST00000160854.7	ENSMUST00000163116.7	ENSMUST00000060049.7
ENSMUST00000042857.13	ENSMUST00000023807.6	ENSMUST00000175787.1	ENSMUST00000086430.4	ENSMUST00000229273.1	ENSMUST00000038676.6
ENSMUST00000161833.7	ENSMUST00000051341.5	ENSMUST00000105720.7	ENSMUST00000190169.1	ENSMUST00000023075.8	ENSMUST00000087629.9
ENSMUST00000027186.11	ENSMUST00000184772.1	ENSMUST00000094451.3	ENSMUST00000179030.7	ENSMUST00000044584.5	ENSMUST00000174019.1
ENSMUST00000238601.1	ENSMUST00000006136.10	ENSMUST00000133533.7	ENSMUST00000161810.1	ENSMUST00000165408.7	ENSMUST000000212997.1
ENSMUST00000127498.2	ENSMUST00000117801.7	ENSMUST00000143888.1	ENSMUST00000042857.13	ENSMUST00000109648.8	ENSMUST00000031008.12
ENSMUST00000114094.2	ENSMUST00000023352.8	ENSMUST00000124771.1	ENSMUST00000160168.1	ENSMUST00000162155.7	ENSMUST000000201422.3
ENSMUST00000027083.6	ENSMUST00000231287.1	ENSMUST00000129314.1	ENSMUST00000158468.3	ENSMUST00000023112.11	ENSMUST00000180708.2
ENSMUST00000129190.7	ENSMUST00000232419.1	ENSMUST00000097742.2	ENSMUST00000094906.3	ENSMUST00000167635.7	ENSMUST00000068110.9
ENSMUST00000027405.5	ENSMUST00000185103.1	ENSMUST00000051509.14	ENSMUST00000114017.7	ENSMUST0000018186.15	ENSMUST00000159584.2
ENSMUST000000036172.9	ENSMUST00000039492.13	ENSMUST00000184043.1	ENSMUST00000114008.2	ENSMUST0000018186.15	ENSMUST00000196121.1
ENSMUST000000035779.14	ENSMUST000000231352.1	ENSMUST00000197458.1	ENSMUST00000027146.8	ENSMUST00000156187.7	ENSMUST00000094757.8
ENSMUST00000113457.8	ENSMUST00000182573.7	ENSMUST00000104703.1	ENSMUST00000164097.3	ENSMUST00000023068.7	ENSMUST00000054095.5
ENSMUST00000175513.1	ENSMUST00000115233.1	ENSMUST00000035799.5	ENSMUST00000152855.1	ENSMUST00000109423.7	ENSMUST00000031121.9
ENSMUST00000184526.1	ENSMUST00000231293.1	ENSMUST00000048302.12	ENSMUST0000004994.15	ENSMUST00000184827.1	ENSMUST00000101121.2
ENSMUST00000180596.1	ENSMUST00000158235.1	ENSMUST00000002708.4	ENSMUST00000087050.6	ENSMUST00000109283.1	ENSMUST00000160104.2
ENSMUST00000176156.1	ENSMUST00000114706.7	ENSMUST00000088117.10	ENSMUST00000189220.6	ENSMUST00000229173.1	ENSMUST00000183797.1
ENSMUST00000097644.8	ENSMUST00000036732.8	ENSMUST00000201347.3	ENSMUST00000137643.1	ENSMUST00000229890.1	ENSMUST00000128112.7
ENSMUST00000212504.1	ENSMUST0000023336.9	ENSMUST00000201314.1	ENSMUST00000119972.3	ENSMUST00000023728.7	ENSMUST00000120827.8
ENSMUST00000189697.1	ENSMUST00000114496.2	ENSMUST00000184943.1	ENSMUST00000119972.3	ENSMUST00000064462.4	ENSMUST00000148830.1
ENSMUST00000053033.13	ENSMUST00000231832.1	ENSMUST00000150088.4	ENSMUST00000119972.3	ENSMUST00000229977.1	ENSMUST00000123393.7
ENSMUST00000160588.1	ENSMUST00000023431.7	ENSMUST00000071949.4	ENSMUST00000119972.3	ENSMUST00000187160.1	ENSMUST00000119339.7
ENSMUST00000062528.8	ENSMUST00000023434.14	ENSMUST00000094836.5	ENSMUST00000119972.3	ENSMUST00000102055.1	ENSMUST00000125462.7
ENSMUST00000181383.2	ENSMUST00000114292.7	ENSMUST00000114099.3	ENSMUST00000119972.3	ENSMUST00000177519.1	ENSMUST00000161490.7
ENSMUST00000183743.1	ENSMUST00000180991.2	ENSMUST00000087332.4	ENSMUST00000119972.3	ENSMUST00000115814.3	ENSMUST00000044125.10
ENSMUST00000038765.5	ENSMUST00000175717.1	ENSMUST00000181335.2	ENSMUST00000119972.3	ENSMUST00000232469.1	ENSMUST00000170792.8
ENSMUST00000183952.1	ENSMUST00000099548.9	ENSMUST00000181083.5	ENSMUST00000185062.1	ENSMUST00000090287.4	ENSMUST00000031239.12
ENSMUST00000052404.12	ENSMUST00000035608.9	ENSMUST00000196113.1	ENSMUST00000043336.10	ENSMUST00000146032.1	ENSMUST00000031198.10
ENSMUST00000190612.1	ENSMUST00000149172.1	ENSMUST00000031090.7	ENSMUST00000189938.1	ENSMUST00000147024.7	ENSMUST00000198960.1
ENSMUST00000188163.1	ENSMUST00000060005.14	ENSMUST00000160066.7	ENSMUST00000070699.14	ENSMUST00000167061.1	ENSMUST00000112385.7
ENSMUST00000208183.2	ENSMUST00000177648.7	ENSMUST00000196575.4	ENSMUST00000187812.1	ENSMUST00000175505.1	ENSMUST000000202603.3
ENSMUST00000189150.1	ENSMUST0000095873.11	ENSMUST00000165536.7	ENSMUST00000190105.1	ENSMUST00000149236.7	ENSMUST00000112153.5
ENSMUST00000186122.6	ENSMUST00000097425.9	ENSMUST00000031121.9	ENSMUST00000151283.1	ENSMUST00000152449.7	ENSMUST00000125738.7
ENSMUST00000007433.4	ENSMUST00000115722.7	ENSMUST00000031146.2	ENSMUST00000191207.1	ENSMUST00000023154.2	ENSMUST00000111967.7
ENSMUST00000007433.4	ENSMUST00000233654.1	ENSMUST00000053733.14	ENSMUST00000124245.2	ENSMUST00000061190.7	ENSMUST00000180430.1
ENSMUST00000195286.4	ENSMUST00000233782.1	ENSMUST00000199312.4	ENSMUST00000027682.8	ENSMUST00000140566.7	ENSMUST000000201614.1
ENSMUST00000112287.1	ENSMUST00000139347.7	ENSMUST00000148750.7	ENSMUST00000112068.9	ENSMUST00000055389.8	ENSMUST00000079368.4



ENSMUST00000185836.1	ENSMUST00000061688.10	ENSMUST00000040576.9	ENSMUST00000059825.11	ENSMUST00000151412.1	ENSMUST00000111752.9
ENSMUST00000188842.6	ENSMUST00000140134.1	ENSMUST00000059657.3	ENSMUST00000074783.11	ENSMUST00000170201.7	ENSMUST00000094327.9
ENSMUST00000159106.1	ENSMUST00000232219.1	ENSMUST00000197105.1	ENSMUST00000186444.1	ENSMUST00000158235.1	ENSMUST00000166983.2
ENSMUST00000044311.8	ENSMUST00000059906.7	ENSMUST00000161490.7	ENSMUST00000128433.7	ENSMUST00000115044.7	ENSMUST00000031347.7
ENSMUST00000111859.7	ENSMUST00000121226.7	ENSMUST00000045617.14	ENSMUST00000185356.6	ENSMUST00000023538.8	ENSMUST00000136312.1
ENSMUST00000183582.1	ENSMUST00000024958.8	ENSMUST00000144623.1	ENSMUST00000195271.4	ENSMUST00000114787.7	ENSMUST00000134780.1
ENSMUST00000187541.6	ENSMUST00000095544.5	ENSMUST00000112887.7	ENSMUST00000139387.7	ENSMUST00000159787.7	ENSMUST00000199537.4
ENSMUST00000181160.2	ENSMUST00000182621.7	ENSMUST00000044125.10	ENSMUST00000048377.10	ENSMUST00000023487.4	ENSMUST000000202466.3
ENSMUST0000015628.3	ENSMUST00000047098.6	ENSMUST00000031249.7	ENSMUST00000111439.7	ENSMUST00000142270.1	ENSMUST000000202728.1
ENSMUST00000177824.7	ENSMUST00000236165.1	ENSMUST00000031249.7	ENSMUST00000005907.11	ENSMUST00000175563.1	ENSMUST00000086023.11
ENSMUST00000166172.8	ENSMUST00000162431.1	ENSMUST00000149128.2	ENSMUST00000180995.2	ENSMUST00000231633.1	ENSMUST00000146354.7
ENSMUST00000158579.1	ENSMUST00000039113.13	ENSMUST00000031224.14	ENSMUST00000180995.2	ENSMUST00000147358.7	ENSMUST00000126232.7
ENSMUST00000133341.2	ENSMUST00000053020.7	ENSMUST00000136882.1	ENSMUST00000156025.1	ENSMUST00000201476.1	ENSMUST00000199377.1
ENSMUST00000193683.5	ENSMUST00000235532.1	ENSMUST00000112677.9	ENSMUST00000053686.8	ENSMUST00000023437.4	ENSMUST00000063635.14
ENSMUST00000027863.12	ENSMUST00000235429.1	ENSMUST00000137939.7	ENSMUST00000028003.8	ENSMUST00000053249.8	ENSMUST00000053498.12
ENSMUST00000097474.8	ENSMUST00000114863.9	ENSMUST00000031205.15	ENSMUST00000111350.9	ENSMUST00000068860.12	ENSMUST00000200314.4
ENSMUST00000193930.1	ENSMUST00000154873.8	ENSMUST00000134865.1	ENSMUST00000151340.7	ENSMUST00000114122.7	ENSMUST00000162890.1
ENSMUST00000097470.3	ENSMUST00000183777.1	ENSMUST00000200404.4	ENSMUST00000015499.13	ENSMUST00000056882.6	ENSMUST00000071421.5
ENSMUST00000046792.8	ENSMUST00000114701.9	ENSMUST00000129146.1	ENSMUST00000166137.2	ENSMUST00000056102.8	ENSMUST00000049324.12
ENSMUST00000238940.1	ENSMUST00000234305.1	ENSMUST00000137398.7	ENSMUST00000065967.13	ENSMUST00000000395.7	ENSMUST00000031653.11
ENSMUST00000111332.1	ENSMUST00000127929.7	ENSMUST00000031583.14	ENSMUST00000194528.2	ENSMUST00000092723.10	ENSMUST000000201992.1
ENSMUST00000085913.10	ENSMUST00000025192.7	ENSMUST00000124316.7	ENSMUST00000128302.7	ENSMUST00000231574.1	ENSMUST00000110483.8
ENSMUST00000055294.3	ENSMUST00000149121.7	ENSMUST00000031540.10	ENSMUST00000131716.3	ENSMUST00000167717.3	ENSMUST00000201142.3
ENSMUST00000194087.5	ENSMUST00000168533.7	ENSMUST00000139500.1	ENSMUST00000193028.1	ENSMUST00000232304.1	ENSMUST00000201142.3
ENSMUST00000195002.1	ENSMUST00000160657.7	ENSMUST00000150127.1	ENSMUST00000124358.1	ENSMUST00000097422.5	ENSMUST00000127366.1
ENSMUST00000027778.7	ENSMUST00000183497.1	ENSMUST00000031591.9	ENSMUST00000077889.7	ENSMUST00000231840.1	ENSMUST00000115537.1
ENSMUST00000162615.1	ENSMUST00000183646.1	ENSMUST00000123431.1	ENSMUST00000217573.1	ENSMUST00000181618.1	ENSMUST00000159378.7
ENSMUST00000079451.12	ENSMUST00000173115.1	ENSMUST00000031354.10	ENSMUST00000137429.1	ENSMUST00000057190.3	ENSMUST00000151060.7
ENSMUST00000194408.1	ENSMUST00000173255.1	ENSMUST00000086123.10	ENSMUST00000175319.1	ENSMUST00000160763.1	ENSMUST00000200755.1
ENSMUST00000151152.2	ENSMUST00000173122.1	ENSMUST00000031367.14	ENSMUST00000161438.1	ENSMUST00000024594.8	ENSMUST00000120965.7
ENSMUST00000082321.8	ENSMUST00000023845.6	ENSMUST00000044441.7	ENSMUST00000215232.1	ENSMUST00000053218.6	ENSMUST00000031798.13
ENSMUST00000216139.1	ENSMUST00000233163.1	ENSMUST00000118268.8	ENSMUST00000186635.1	ENSMUST00000232147.1	ENSMUST00000151777.7
ENSMUST0000019901.6	ENSMUST00000120717.7	ENSMUST00000154840.2	ENSMUST00000092672.5	ENSMUST00000181658.1	ENSMUST00000115096.3
ENSMUST00000105590.7	ENSMUST00000159478.2	ENSMUST00000065785.3	ENSMUST00000100012.2	ENSMUST00000162659.1	ENSMUST00000163047.7
ENSMUST0000019974.4	ENSMUST00000024725.4	ENSMUST00000058897.10	ENSMUST00000141350.1	ENSMUST00000095615.2	ENSMUST00000036877.9
ENSMUST00000175676.1	ENSMUST0000025036.10	ENSMUST00000049393.14	ENSMUST00000081989.7	ENSMUST00000061725.7	ENSMUST00000126621.2
ENSMUST00000037964.6	ENSMUST00000056113.4	ENSMUST00000110929.8	ENSMUST00000191234.6	ENSMUST00000158630.1	ENSMUST000000201342.3
ENSMUST00000214043.1	ENSMUST00000184453.1	ENSMUST00000071881.9	ENSMUST00000215144.1	ENSMUST00000152107.2	ENSMUST00000031902.6
ENSMUST00000020165.13	ENSMUST00000070673.8	ENSMUST0000000153.8	ENSMUST00000173494.3	ENSMUST00000114801.8	ENSMUST00000031750.13
ENSMUST00000071008.5	ENSMUST00000178545.2	ENSMUST00000212355.1	ENSMUST00000170047.1	ENSMUST00000232805.1	ENSMUST00000204095.2
ENSMUST00000178026.1	ENSMUST00000060072.11	ENSMUST00000156467.1	ENSMUST00000213330.1	ENSMUST00000114737.7	ENSMUST00000166247.7
ENSMUST00000178026.1	ENSMUST0000024847.13	ENSMUST00000238592.1	ENSMUST00000217501.1	ENSMUST00000234618.1	ENSMUST00000031840.9
ENSMUST00000159174.1	ENSMUST00000234560.1	ENSMUST00000199096.1	ENSMUST00000200401.1	ENSMUST0000024827.4	ENSMUST00000163954.7
ENSMUST00000154916.1	ENSMUST00000234640.1	ENSMUST00000174285.7	ENSMUST00000182898.7	ENSMUST0000024839.5	ENSMUST00000184470.1
ENSMUST00000105520.7	ENSMUST00000234927.1	ENSMUST00000201128.1	ENSMUST00000198998.1	ENSMUST0000024839.5	ENSMUST00000159006.1
ENSMUST00000162343.1	ENSMUST00000112389.8	ENSMUST00000118527.7	ENSMUST00000164428.2	ENSMUST00000077639.6	ENSMUST00000133723.1
ENSMUST0000019920.12	ENSMUST0000025092.4	ENSMUST00000129092.1	ENSMUST00000036304.3	ENSMUST00000025196.8	ENSMUST00000205200.2
ENSMUST00000062784.7	ENSMUST0000000687.8	ENSMUST00000201604.1	ENSMUST00000049242.8	ENSMUST00000236331.1	ENSMUST00000127748.4
ENSMUST00000092566.7	ENSMUST00000183295.1	ENSMUST00000202188.1	ENSMUST00000049242.8	ENSMUST00000236230.1	ENSMUST00000203101.2
ENSMUST00000044672.10	ENSMUST00000234189.1	ENSMUST00000115577.8	ENSMUST00000202278.5	ENSMUST00000173669.1	ENSMUST00000145111.7
ENSMUST00000160262.8	ENSMUST00000224200.2	ENSMUST00000172356.7	ENSMUST00000219687.1	ENSMUST00000097337.7	ENSMUST00000044505.13
ENSMUST00000147196.2	ENSMUST00000053917.5	ENSMUST00000129452.7	ENSMUST00000095580.2	ENSMUST00000037849.2	ENSMUST00000212375.1
ENSMUST00000216878.1	ENSMUST00000048977.15	ENSMUST00000141064.1	ENSMUST00000117086.1	ENSMUST0000025253.11	ENSMUST00000212792.1
ENSMUST00000162062.1	ENSMUST0000002549.8	ENSMUST00000031681.9	ENSMUST00000170048.1	ENSMUST00000173281.7	ENSMUST00000205269.1
ENSMUST00000217995.1	ENSMUST00000130296.1	ENSMUST00000052277.4	ENSMUST00000144740.1	ENSMUST00000095467.3	ENSMUST00000160894.7
ENSMUST0000020022.7	ENSMUST00000237662.1	ENSMUST00000115323.7	ENSMUST00000064562.13	ENSMUST00000209623.1	ENSMUST00000032122.10
ENSMUST00000219142.1	ENSMUST00000012426.2	ENSMUST00000115320.7	ENSMUST00000045628.14	ENSMUST00000087144.4	ENSMUST00000186147.6
ENSMUST00000099691.10	ENSMUST00000235404.1	ENSMUST00000124522.2	ENSMUST00000184241.1	ENSMUST00000171813.3	ENSMUST00000151508.1
ENSMUST00000155982.1	ENSMUST00000235404.1	ENSMUST00000202703.1	ENSMUST00000156260.1	ENSMUST00000113614.2	ENSMUST00000113823.7
ENSMUST00000105439.1	ENSMUST00000194544.1	ENSMUST00000101532.9	ENSMUST00000020485.9	ENSMUST00000229744.1	ENSMUST00000127459.7

ENSMUST00000145936.1	ENSMUST00000193984.1	ENSMUST00000161779.7	ENSMUST00000020234.13	ENSMUST00000233473.1	ENSMUST00000173919.1
ENSMUST00000037813.4	ENSMUST00000194691.1	ENSMUST00000180886.2	ENSMUST00000218095.1	ENSMUST00000162469.1	ENSMUST00000162547.2
ENSMUST00000184957.1	ENSMUST00000192931.1	ENSMUST00000189910.1	ENSMUST00000217747.1	ENSMUST00000162029.7	ENSMUST00000032132.8
ENSMUST00000001147.4	ENSMUST00000192931.1	ENSMUST00000031843.6	ENSMUST00000219612.1	ENSMUST00000168440.2	ENSMUST00000151699.3
ENSMUST00000075421.6	ENSMUST00000192931.1	ENSMUST00000125581.1	ENSMUST00000095360.10	ENSMUST00000071135.5	ENSMUST00000079832.2
ENSMUST00000057608.4	ENSMUST00000195624.1	ENSMUST00000127485.7	ENSMUST00000121629.7	ENSMUST00000164605.7	ENSMUST00000127199.1
ENSMUST00000005488.8	ENSMUST00000195112.1	ENSMUST00000079584.2	ENSMUST00000004473.14	ENSMUST00000166543.9	ENSMUST00000181849.1
ENSMUST00000006679.14	ENSMUST00000195363.1	ENSMUST00000204810.1	ENSMUST00000182936.7	ENSMUST00000233983.1	ENSMUST00000133321.1
ENSMUST00000154212.7	ENSMUST00000195363.1	ENSMUST00000064948.12	ENSMUST00000008542.11	ENSMUST00000086639.5	ENSMUST00000113438.7
ENSMUST00000051773.8	ENSMUST00000195363.1	ENSMUST00000168387.7	ENSMUST00000147379.2	ENSMUST00000234981.1	ENSMUST00000204224.2
ENSMUST00000220312.1	ENSMUST00000195363.1	ENSMUST00000119728.1	ENSMUST00000092213.10	ENSMUST00000235072.1	ENSMUST00000089295.5
ENSMUST00000119492.1	ENSMUST00000195069.1	ENSMUST00000159062.7	ENSMUST00000099337.4	ENSMUST00000112305.9	ENSMUST00000101120.10
ENSMUST00000105315.2	ENSMUST00000192535.1	ENSMUST00000074881.1	ENSMUST0000020217.6	ENSMUST00000055221.8	ENSMUST00000197023.1
ENSMUST00000020220.14	ENSMUST00000003599.8	ENSMUST00000183891.1	ENSMUST00000218263.1	ENSMUST00000173765.1	ENSMUST00000053559.4
ENSMUST00000099396.2	ENSMUST00000003599.8	ENSMUST00000113326.8	ENSMUST00000219698.1	ENSMUST00000234081.1	ENSMUST00000032462.8
ENSMUST00000156097.1	ENSMUST00000194928.1	ENSMUST00000203489.2	ENSMUST00000061506.8	ENSMUST00000047762.9	ENSMUST00000038234.12
ENSMUST00000182462.7	ENSMUST00000194928.1	ENSMUST00000113261.8	ENSMUST00000165067.8	ENSMUST00000209628.1	ENSMUST00000203332.1
ENSMUST00000168110.7	ENSMUST00000195764.1	ENSMUST00000059286.13	ENSMUST00000105276.7	ENSMUST00000157325.1	ENSMUST00000220845.1
ENSMUST00000181906.2	ENSMUST00000195764.1	ENSMUST00000101032.9	ENSMUST00000188776.6	ENSMUST00000092015.10	ENSMUST00000168793.7
ENSMUST00000220218.1	ENSMUST00000208907.1	ENSMUST00000186889.6	ENSMUST00000099276.3	ENSMUST00000222726.1	ENSMUST00000032233.8
ENSMUST00000175211.1	ENSMUST00000192984.5	ENSMUST0000032272.12	ENSMUST00000142617.1	ENSMUST00000132571.1	ENSMUST00000049124.9
ENSMUST00000055355.5	ENSMUST00000236889.1	ENSMUST00000129815.7	ENSMUST00000127070.1	ENSMUST00000115816.2	ENSMUST00000068797.2
ENSMUST00000006949.8	ENSMUST00000237162.1	ENSMUST00000068593.8	ENSMUST0000020381.4	ENSMUST00000234549.1	ENSMUST00000088246.5
ENSMUST0000020350.14	ENSMUST00000136118.7	ENSMUST0000032218.9	ENSMUST00000175924.1	ENSMUST00000134663.1	ENSMUST00000088246.5
ENSMUST00000020378.4	ENSMUST0000025377.13	ENSMUST00000202878.3	ENSMUST0000026476.12	ENSMUST00000234198.1	ENSMUST00000161619.7
ENSMUST00000127564.1	ENSMUST00000237797.1	ENSMUST0000000186.8	ENSMUST00000092058.3	ENSMUST00000234654.1	ENSMUST00000040751.5
ENSMUST00000175867.1	ENSMUST00000089874.8	ENSMUST0000000188.11	ENSMUST00000099139.8	ENSMUST00000237971.1	ENSMUST00000040751.5
ENSMUST00000219179.1	ENSMUST00000184994.7	ENSMUST00000112173.7	ENSMUST00000180875.1	ENSMUST00000042345.7	ENSMUST00000078521.6
ENSMUST0000020322.11	ENSMUST00000127591.1	ENSMUST00000043259.9	ENSMUST00000128666.1	ENSMUST00000236387.1	ENSMUST00000032500.8
ENSMUST00000039259.6	ENSMUST00000135688.1	ENSMUST00000135562.7	ENSMUST00000109855.7	ENSMUST00000025212.7	ENSMUST00000147106.2
ENSMUST00000079692.5	ENSMUST00000171629.2	ENSMUST00000148424.1	ENSMUST00000151522.1	ENSMUST00000237243.1	ENSMUST00000173837.5
ENSMUST00000050901.4	ENSMUST00000025477.14	ENSMUST00000068865.11	ENSMUST00000059319.7	ENSMUST00000236889.1	ENSMUST00000173837.5
ENSMUST00000184999.1	ENSMUST0000025482.9	ENSMUST00000163804.7	ENSMUST00000185114.1	ENSMUST00000235606.1	ENSMUST00000049150.7
ENSMUST00000044682.6	ENSMUST00000145081.7	ENSMUST00000167298.1	ENSMUST00000109504.7	ENSMUST00000121805.8	ENSMUST00000203352.1
ENSMUST00000102950.9	ENSMUST00000114943.10	ENSMUST00000179971.7	ENSMUST00000039900.3	ENSMUST00000082254.7	ENSMUST00000167323.2
ENSMUST00000109910.8	ENSMUST00000176435.7	ENSMUST00000131379.3	ENSMUST00000208530.1	ENSMUST00000238707.1	ENSMUST00000141548.3
ENSMUST0000011476.1	ENSMUST00000074157.12	ENSMUST00000185220.2	ENSMUST00000102842.9	ENSMUST00000237844.1	ENSMUST00000032421.3
ENSMUST00000146002.7	ENSMUST00000181913.1	ENSMUST00000210805.1	ENSMUST00000102829.3	ENSMUST00000102912.7	ENSMUST00000079573.12
ENSMUST000000403377.5	ENSMUST00000091831.12	ENSMUST00000108493.2	ENSMUST00000156571.7	ENSMUST00000238028.1	ENSMUST00000145034.2
ENSMUST00000131515.1	ENSMUST00000126153.7	ENSMUST00000174918.1	ENSMUST00000057679.9	ENSMUST00000025497.7	ENSMUST00000163574.7
ENSMUST00000118661.7	ENSMUST00000035501.10	ENSMUST00000032560.5	ENSMUST00000093142.11	ENSMUST00000056533.8	ENSMUST00000054781.6
ENSMUST00000125302.1	ENSMUST00000114741.3	ENSMUST00000005413.3	ENSMUST00000151098.1	ENSMUST00000175586.1	ENSMUST00000209833.1
ENSMUST00000159081.7	ENSMUST00000066743.10	ENSMUST00000005413.3	ENSMUST00000137096.1	ENSMUST00000067743.1	ENSMUST00000072475.8
ENSMUST00000136830.1	ENSMUST00000167977.7	ENSMUST00000080594.7	ENSMUST00000153206.7	ENSMUST00000237114.1	ENSMUST00000131379.3
ENSMUST00000129425.7	ENSMUST00000171071.8	ENSMUST00000205328.1	ENSMUST00000068853.12	ENSMUST00000117694.1	ENSMUST00000098799.4
ENSMUST00000109363.7	ENSMUST00000161429.2	ENSMUST00000184632.1	ENSMUST00000108848.1	ENSMUST00000080050.5	ENSMUST00000181501.2
ENSMUST00000102815.9	ENSMUST00000237521.1	ENSMUST00000137414.1	ENSMUST00000064786.11	ENSMUST00000066532.4	ENSMUST00000205716.1
ENSMUST00000020362.2	ENSMUST00000237320.1	ENSMUST00000183983.1	ENSMUST00000073924.9	ENSMUST00000079618.10	ENSMUST00000206487.2
ENSMUST00000146198.1	ENSMUST00000051803.7	ENSMUST00000207858.1	ENSMUST00000101148.8	ENSMUST0000026494.13	ENSMUST00000208685.1
ENSMUST00000020672.4	ENSMUST00000184641.1	ENSMUST00000170371.1	ENSMUST00000150954.7	ENSMUST00000180530.2	ENSMUST00000208685.1
ENSMUST00000149997.7	ENSMUST00000041827.7	ENSMUST00000054427.12	ENSMUST00000202178.3	ENSMUST00000171071.8	ENSMUST00000208198.1
ENSMUST00000049038.3	ENSMUST00000134821.1	ENSMUST00000189673.6	ENSMUST0000018651.13	ENSMUST00000097495.4	ENSMUST00000014830.7
ENSMUST00000020679.2	ENSMUST00000184812.1	ENSMUST00000053156.9	ENSMUST00000150336.7	ENSMUST00000210766.1	ENSMUST00000052605.7
ENSMUST00000109220.7	ENSMUST00000040772.8	ENSMUST00000167369.7	ENSMUST00000047463.14	ENSMUST00000235763.1	ENSMUST00000137342.1
ENSMUST00000139484.1	ENSMUST00000032557.14	ENSMUST000000206388.1	ENSMUST00000046963.9	ENSMUST00000237815.1	ENSMUST00000206705.2
ENSMUST00000108853.7	ENSMUST00000035444.9	ENSMUST00000042985.10	ENSMUST00000080665.9	ENSMUST00000237815.1	ENSMUST0000003207.10
ENSMUST00000138587.8	ENSMUST00000025563.7	ENSMUST00000032585.7	ENSMUST00000123454.7	ENSMUST00000236364.1	ENSMUST00000041845.13
ENSMUST00000108783.3	ENSMUST00000055115.8	ENSMUST00000108015.3	ENSMUST00000021288.9	ENSMUST00000025834.14	ENSMUST00000108341.1
ENSMUST00000146033.7	ENSMUST00000238167.1	ENSMUST00000205995.1	ENSMUST00000153671.7	ENSMUST00000170010.2	ENSMUST00000056589.13
ENSMUST00000049091.8	ENSMUST00000025646.2	ENSMUST00000075162.4	ENSMUST00000024543.2	ENSMUST00000124478.7	ENSMUST00000178767.2

ENSMUST00000144922.1	ENSMUST00000025581.6	ENSMUST00000179443.2	ENSMUST00000181810.7	ENSMUST00000184789.1	ENSMUST00000208238.1
ENSMUST00000170942.1	ENSMUST00000061235.2	ENSMUST00000211150.1	ENSMUST0000018896.13	ENSMUST00000236564.1	ENSMUST00000208318.1
ENSMUST00000154220.7	ENSMUST00000052011.14	ENSMUST00000211220.1	ENSMUST00000157075.7	ENSMUST00000049948.5	ENSMUST00000164589.8
ENSMUST00000021259.8	ENSMUST00000235722.1	ENSMUST00000210655.1	ENSMUST00000108527.7	ENSMUST00000169159.2	ENSMUST00000182067.7
ENSMUST00000035539.11	ENSMUST00000048935.5	ENSMUST00000119710.2	ENSMUST00000092938.4	ENSMUST00000139270.7	ENSMUST00000182067.7
ENSMUST00000108508.2	ENSMUST00000053068.6	ENSMUST00000176734.1	ENSMUST00000049676.2	ENSMUST00000025601.7	ENSMUST00000182634.7
ENSMUST00000045303.9	ENSMUST00000064393.5	ENSMUST00000036372.7	ENSMUST00000102514.3	ENSMUST00000052737.1	ENSMUST00000080518.13
ENSMUST00000155774.1	ENSMUST00000043610.12	ENSMUST00000181631.1	ENSMUST00000000769.13	ENSMUST00000237350.1	ENSMUST00000032709.2
ENSMUST00000021207.6	ENSMUST00000065067.13	ENSMUST00000156690.7	ENSMUST00000108437.7	ENSMUST00000074770.12	ENSMUST00000070191.9
ENSMUST00000108400.7	ENSMUST00000236290.1	ENSMUST00000165175.7	ENSMUST00000142542.7	ENSMUST00000237688.1	ENSMUST00000206581.1
ENSMUST00000136011.1	ENSMUST00000073391.4	ENSMUST00000206092.1	ENSMUST00000060539.12	ENSMUST00000025797.6	ENSMUST00000165308.7
ENSMUST0000001122.5	ENSMUST00000130039.2	ENSMUST00000128154.7	ENSMUST00000108294.1	ENSMUST00000124012.7	ENSMUST00000165029.2
ENSMUST00000108189.8	ENSMUST0000025983.12	ENSMUST00000042318.5	ENSMUST00000208783.1	ENSMUST00000225920.1	ENSMUST00000233771.1
ENSMUST00000132477.1	ENSMUST0000025986.14	ENSMUST00000056728.4	ENSMUST00000018478.10	ENSMUST00000079754.10	ENSMUST00000233266.1
ENSMUST00000021016.9	ENSMUST00000059672.8	ENSMUST00000165388.1	ENSMUST00000083555.1	ENSMUST00000025966.4	ENSMUST00000239023.1
ENSMUST0000018522.12	ENSMUST00000026211.9	ENSMUST00000171397.1	ENSMUST00000214041.1	ENSMUST0000025979.12	ENSMUST00000206839.1
ENSMUST00000175244.1	ENSMUST00000026221.6	ENSMUST0000001792.11	ENSMUST00000142709.1	ENSMUST00000160286.1	ENSMUST00000032955.6
ENSMUST00000061938.13	ENSMUST00000184584.1	ENSMUST00000208409.1	ENSMUST00000175848.7	ENSMUST00000169141.7	ENSMUST00000197423.1
ENSMUST00000062709.3	ENSMUST00000026240.13	ENSMUST00000041761.6	ENSMUST00000175537.1	ENSMUST00000099428.4	ENSMUST00000209617.1
ENSMUST00000100519.10	ENSMUST00000160247.2	ENSMUST00000208720.1	ENSMUST00000044423.3	ENSMUST00000225254.1	ENSMUST00000210602.1
ENSMUST00000107622.1	ENSMUST00000237029.1	ENSMUST00000118157.7	ENSMUST00000060360.6	ENSMUST00000063632.13	ENSMUST00000211066.1
ENSMUST00000093942.4	ENSMUST00000237480.1	ENSMUST00000208646.1	ENSMUST00000060360.6	ENSMUST00000026012.7	ENSMUST00000104493.1
ENSMUST00000093939.3	ENSMUST00000069183.7	ENSMUST00000127492.1	ENSMUST00000093956.3	ENSMUST00000237869.1	ENSMUST00000205613.1
ENSMUST00000144720.1	ENSMUST00000038949.5	ENSMUST00000032958.13	ENSMUST00000107717.7	ENSMUST00000167239.7	ENSMUST00000107478.8
ENSMUST00000103132.9	ENSMUST00000079360.11	ENSMUST00000033341.11	ENSMUST00000013559.2	ENSMUST00000038949.5	ENSMUST00000169922.8
ENSMUST00000007280.8	ENSMUST00000235987.1	ENSMUST00000106739.7	ENSMUST00000184494.1	ENSMUST00000234346.1	ENSMUST00000107456.3
ENSMUST00000139424.1	ENSMUST00000002176.12	ENSMUST00000118571.1	ENSMUST00000103141.3	ENSMUST00000176631.1	ENSMUST00000107394.2
ENSMUST00000067444.9	ENSMUST00000155530.7	ENSMUST00000170374.7	ENSMUST00000017741.3	ENSMUST00000163821.2	ENSMUST00000142678.1
ENSMUST00000021329.13	ENSMUST00000028059.8	ENSMUST00000084696.5	ENSMUST00000140543.1	ENSMUST00000115022.7	ENSMUST00000098331.9
ENSMUST00000137086.7	ENSMUST00000091436.6	ENSMUST00000069449.6	ENSMUST00000170056.1	ENSMUST00000127282.1	ENSMUST00000173287.7
ENSMUST00000001965.13	ENSMUST00000114723.8	ENSMUST00000170430.2	ENSMUST00000057054.7	ENSMUST00000044009.13	ENSMUST00000064174.11
ENSMUST0000018516.10	ENSMUST00000146205.2	ENSMUST00000153518.7	ENSMUST00000055409.5	ENSMUST00000195480.1	ENSMUST00000232924.1
ENSMUST00000106767.2	ENSMUST00000150788.5	ENSMUST00000084640.2	ENSMUST0000006749.9	ENSMUST00000151782.1	ENSMUST00000206791.1
ENSMUST00000021066.3	ENSMUST00000077257.11	ENSMUST00000171880.2	ENSMUST00000154798.7	ENSMUST00000114853.7	ENSMUST00000107128.7
ENSMUST00000041627.13	ENSMUST00000183583.7	ENSMUST00000073935.6	ENSMUST00000021323.10	ENSMUST00000028106.10	ENSMUST00000207617.1
ENSMUST00000106532.3	ENSMUST00000028187.6	ENSMUST00000060783.6	ENSMUST00000138384.7	ENSMUST00000061545.6	ENSMUST00000032995.14
ENSMUST00000148484.8	ENSMUST00000050000.15	ENSMUST00000076091.3	ENSMUST0000002048.7	ENSMUST00000061545.6	ENSMUST00000032977.10
ENSMUST00000017610.9	ENSMUST00000041730.10	ENSMUST00000123666.7	ENSMUST00000044462.3	ENSMUST00000114791.8	ENSMUST00000207405.1
ENSMUST00000142751.1	ENSMUST00000131534.7	ENSMUST00000043138.12	ENSMUST0000001059.8	ENSMUST00000148248.2	ENSMUST00000175555.1
ENSMUST00000139014.1	ENSMUST00000062069.5	ENSMUST00000206551.1	ENSMUST00000021065.5	ENSMUST00000184784.1	ENSMUST00000060174.5
ENSMUST00000056781.4	ENSMUST00000057279.5	ENSMUST00000165457.1	ENSMUST00000084368.11	ENSMUST00000114505.1	ENSMUST00000211368.1
ENSMUST00000039146.3	ENSMUST00000153422.7	ENSMUST00000209747.1	ENSMUST00000092404.12	ENSMUST00000114259.2	ENSMUST00000061482.5
ENSMUST00000218169.1	ENSMUST00000128451.7	ENSMUST0000026550.13	ENSMUST00000196236.1	ENSMUST00000076989.6	ENSMUST00000051201.6
ENSMUST00000111178.1	ENSMUST00000036934.11	ENSMUST00000084436.9	ENSMUST00000106354.8	ENSMUST00000114159.8	ENSMUST00000211384.1
ENSMUST00000217677.1	ENSMUST00000178799.7	ENSMUST00000189314.6	ENSMUST00000119455.1	ENSMUST00000104004.3	ENSMUST00000128388.1
ENSMUST00000218402.1	ENSMUST0000028347.12	ENSMUST00000131791.1	ENSMUST00000033230.7	ENSMUST0000028280.13	ENSMUST00000078482.12
ENSMUST00000046207.8	ENSMUST00000202653.1	ENSMUST00000132167.7	ENSMUST00000100181.10	ENSMUST00000164290.7	ENSMUST00000052438.7
ENSMUST00000163627.2	ENSMUST00000200839.3	ENSMUST0000000219.9	ENSMUST00000144529.1	ENSMUST00000126784.1	ENSMUST00000055745.4
ENSMUST00000218277.1	ENSMUST00000238989.1	ENSMUST00000207792.1	ENSMUST00000141795.1	ENSMUST0000028135.14	ENSMUST00000079282.7
ENSMUST00000220545.1	ENSMUST00000100050.3	ENSMUST00000211027.1	ENSMUST00000147877.7	ENSMUST00000113132.8	ENSMUST000002126011.1
ENSMUST00000177778.8	ENSMUST00000149421.7	ENSMUST00000066258.7	ENSMUST00000184435.1	ENSMUST00000102800.7	ENSMUST00000209597.1
ENSMUST00000149246.7	ENSMUST00000028515.3	ENSMUST00000098909.4	ENSMUST00000092302.10	ENSMUST00000028248.10	ENSMUST00000154848.1
ENSMUST00000149246.7	ENSMUST00000147235.1	ENSMUST0000006742.10	ENSMUST00000036690.6	ENSMUST00000039165.14	ENSMUST00000084705.11
ENSMUST00000220998.1	ENSMUST00000001872.4	ENSMUST00000211747.1	ENSMUST00000021001.9	ENSMUST00000183581.1	ENSMUST00000163996.1
ENSMUST00000221643.1	ENSMUST00000125119.1	ENSMUST00000210148.1	ENSMUST00000220210.1	ENSMUST00000226455.1	ENSMUST00000206034.1
ENSMUST00000219899.1	ENSMUST00000151799.7	ENSMUST00000084031.5	ENSMUST0000020958.8	ENSMUST00000112525.4	ENSMUST00000140689.7
ENSMUST0000021005.14	ENSMUST00000111466.2	ENSMUST00000210273.1	ENSMUST0000020911.13	ENSMUST00000129133.1	ENSMUST00000121744.8
ENSMUST00000220951.1	ENSMUST0000005643.13	ENSMUST00000170705.7	ENSMUST00000220506.1	ENSMUST00000184202.1	ENSMUST00000129334.7
ENSMUST00000085412.6	ENSMUST00000067663.13	ENSMUST00000135764.7	ENSMUST00000043396.14	ENSMUST00000130618.7	ENSMUST00000084650.5
ENSMUST00000056228.7	ENSMUST00000129118.1	ENSMUST00000183849.1	ENSMUST00000095820.11	ENSMUST00000123858.7	ENSMUST00000213149.1

ENSMUST00000219809.1	ENSMUST00000158014.1	ENSMUST00000095328.5	ENSMUST00000175296.1	ENSMUST00000146970.1	ENSMUST00000056042.5
ENSMUST00000072631.5	ENSMUST00000065797.6	ENSMUST00000125295.7	ENSMUST00000177778.8	ENSMUST00000124825.1	ENSMUST00000149535.1
ENSMUST00000150292.7	ENSMUST00000111274.8	ENSMUST00000170416.7	ENSMUST00000221952.1	ENSMUST00000146495.7	ENSMUST00000206198.1
ENSMUST00000044380.7	ENSMUST00000197461.1	ENSMUST00000208508.2	ENSMUST0000020970.9	ENSMUST00000041099.4	ENSMUST00000106437.1
ENSMUST00000021494.5	ENSMUST00000138580.1	ENSMUST00000208507.1	ENSMUST00000219672.1	ENSMUST00000041099.4	ENSMUST00000117762.7
ENSMUST00000110451.3	ENSMUST00000135153.7	ENSMUST00000048967.8	ENSMUST0000003079.11	ENSMUST00000148184.1	ENSMUST00000033049.8
ENSMUST00000220238.1	ENSMUST00000131063.1	ENSMUST00000048565.8	ENSMUST00000049089.6	ENSMUST00000136058.7	ENSMUST00000033044.15
ENSMUST00000182077.1	ENSMUST00000194826.2	ENSMUST00000098713.4	ENSMUST00000078481.13	ENSMUST00000140248.1	ENSMUST00000067680.10
ENSMUST00000065536.8	ENSMUST00000130634.1	ENSMUST00000207684.1	ENSMUST00000043884.5	ENSMUST00000148314.2	ENSMUST00000157516.1
ENSMUST00000223220.1	ENSMUST00000150183.8	ENSMUST00000052072.7	ENSMUST00000159708.7	ENSMUST00000137973.1	ENSMUST00000209297.2
ENSMUST00000054565.7	ENSMUST00000043970.1	ENSMUST00000184793.1	ENSMUST00000044634.11	ENSMUST00000143559.1	ENSMUST00000196540.4
ENSMUST00000222543.1	ENSMUST00000024005.7	ENSMUST00000161557.7	ENSMUST00000094291.2	ENSMUST00000152584.1	ENSMUST00000121839.1
ENSMUST00000221216.1	ENSMUST00000148587.7	ENSMUST00000117845.7	ENSMUST00000063445.12	ENSMUST00000141047.1	ENSMUST00000055353.8
ENSMUST00000162221.2	ENSMUST00000037547.8	ENSMUST00000034133.13	ENSMUST00000182123.1	ENSMUST00000039160.2	ENSMUST00000209398.1
ENSMUST00000127300.1	ENSMUST00000028780.3	ENSMUST00000034074.7	ENSMUST00000110560.2	ENSMUST00000102524.7	ENSMUST00000026561.9
ENSMUST00000021603.8	ENSMUST00000123656.1	ENSMUST00000209208.1	ENSMUST00000110522.9	ENSMUST00000184907.1	ENSMUST00000186288.6
ENSMUST00000123655.7	ENSMUST00000028683.13	ENSMUST00000137202.7	ENSMUST00000057859.8	ENSMUST00000110674.3	ENSMUST00000208124.1
ENSMUST00000070659.6	ENSMUST00000133898.7	ENSMUST00000119870.8	ENSMUST00000061273.11	ENSMUST00000225087.1	ENSMUST00000175480.1
ENSMUST00000021706.10	ENSMUST00000142747.1	ENSMUST00000064576.7	ENSMUST00000221750.1	ENSMUST00000140221.1	ENSMUST00000121758.7
ENSMUST00000180698.2	ENSMUST00000147095.1	ENSMUST00000212318.1	ENSMUST00000042299.3	ENSMUST00000110286.7	ENSMUST00000117718.1
ENSMUST00000084953.12	ENSMUST00000039978.12	ENSMUST00000164884.8	ENSMUST00000021459.13	ENSMUST00000055421.5	ENSMUST00000161680.1
ENSMUST00000160576.1	ENSMUST00000028855.13	ENSMUST00000093622.1	ENSMUST00000079533.11	ENSMUST00000120631.1	ENSMUST00000044857.3
ENSMUST00000189759.6	ENSMUST00000138751.1	ENSMUST00000043141.6	ENSMUST00000219642.1	ENSMUST00000143453.1	ENSMUST00000044857.3
ENSMUST00000169593.1	ENSMUST00000028826.3	ENSMUST00000154803.1	ENSMUST00000218943.1	ENSMUST00000110157.8	ENSMUST00000152698.1
ENSMUST00000058491.7	ENSMUST00000028836.6	ENSMUST00000049509.6	ENSMUST00000073251.7	ENSMUST00000148271.7	ENSMUST00000207477.1
ENSMUST00000222459.1	ENSMUST00000035264.8	ENSMUST00000109104.1	ENSMUST00000163402.7	ENSMUST00000134937.1	ENSMUST00000180353.1
ENSMUST00000035515.4	ENSMUST00000125486.1	ENSMUST00000212052.1	ENSMUST00000186848.4	ENSMUST00000124751.1	ENSMUST00000211363.1
ENSMUST00000222098.1	ENSMUST00000110083.7	ENSMUST00000212454.1	ENSMUST00000147469.7	ENSMUST00000099296.3	ENSMUST00000185110.1
ENSMUST00000064204.13	ENSMUST00000099307.3	ENSMUST00000052580.9	ENSMUST00000021649.7	ENSMUST00000210482.1	ENSMUST00000204916.2
ENSMUST00000220758.1	ENSMUST00000140124.1	ENSMUST00000238386.1	ENSMUST00000171853.1	ENSMUST00000137929.1	ENSMUST00000133298.7
ENSMUST00000222482.1	ENSMUST00000150913.1	ENSMUST00000063508.14	ENSMUST00000040766.8	ENSMUST00000109970.4	ENSMUST00000169834.1
ENSMUST00000130585.1	ENSMUST00000072997.9	ENSMUST00000086580.11	ENSMUST00000177587.8	ENSMUST00000109935.7	ENSMUST00000190830.1
ENSMUST00000072044.1	ENSMUST00000099178.9	ENSMUST00000217187.1	ENSMUST00000146292.7	ENSMUST00000035346.13	ENSMUST00000140417.8
ENSMUST00000041674.13	ENSMUST00000029143.5	ENSMUST00000034692.8	ENSMUST00000221468.1	ENSMUST00000028981.8	ENSMUST00000121438.8
ENSMUST00000074067.3	ENSMUST00000124676.1	ENSMUST00000122714.1	ENSMUST00000183118.1	ENSMUST00000144827.1	ENSMUST00000095345.4
ENSMUST00000057866.12	ENSMUST00000126767.1	ENSMUST00000067646.11	ENSMUST00000101168.3	ENSMUST00000129137.7	ENSMUST00000207505.1
ENSMUST00000057428.12	ENSMUST00000103116.9	ENSMUST00000173769.2	ENSMUST00000221929.1	ENSMUST00000143169.1	ENSMUST00000124544.7
ENSMUST00000167163.7	ENSMUST00000109454.7	ENSMUST00000115336.9	ENSMUST00000221356.1	ENSMUST00000135945.1	ENSMUST00000095323.7
ENSMUST00000053265.7	ENSMUST00000133322.1	ENSMUST0000003501.8	ENSMUST0000021605.13	ENSMUST00000136933.7	ENSMUST00000053558.9
ENSMUST00000021860.6	ENSMUST0000018353.13	ENSMUST00000152480.1	ENSMUST00000101114.10	ENSMUST00000109811.7	ENSMUST00000038738.6
ENSMUST00000021787.6	ENSMUST00000063251.2	ENSMUST00000183580.2	ENSMUST00000090990.5	ENSMUST00000069600.12	ENSMUST00000033918.3
ENSMUST00000055341.6	ENSMUST00000109358.7	ENSMUST00000178236.2	ENSMUST00000220629.1	ENSMUST00000186977.1	ENSMUST00000144711.8
ENSMUST00000221359.1	ENSMUST00000029208.14	ENSMUST00000115068.9	ENSMUST00000222310.1	ENSMUST00000103122.9	ENSMUST00000226075.1
ENSMUST00000159595.1	ENSMUST00000109157.1	ENSMUST00000051004.4	ENSMUST00000221787.1	ENSMUST00000065039.2	ENSMUST00000223675.1
ENSMUST00000035540.8	ENSMUST00000131346.1	ENSMUST00000044155.14	ENSMUST00000056110.14	ENSMUST00000146600.1	ENSMUST00000211284.1
ENSMUST00000071065.7	ENSMUST00000059452.5	ENSMUST00000114840.1	ENSMUST00000056110.14	ENSMUST00000135838.1	ENSMUST00000210210.1
ENSMUST00000201658.3	ENSMUST00000109066.1	ENSMUST00000159385.7	ENSMUST00000122586.1	ENSMUST00000109443.7	ENSMUST00000038959.15
ENSMUST00000223430.1	ENSMUST00000134982.7	ENSMUST00000139389.7	ENSMUST00000082687.1	ENSMUST0000017961.10	ENSMUST00000078350.12
ENSMUST00000135343.1	ENSMUST00000108916.7	ENSMUST00000098827.2	ENSMUST00000116706.1	ENSMUST00000103096.9	ENSMUST00000052437.5
ENSMUST00000036825.13	ENSMUST00000081134.9	ENSMUST00000060125.6	ENSMUST00000221897.1	ENSMUST00000200215.1	ENSMUST00000212436.1
ENSMUST00000021968.6	ENSMUST00000108878.1	ENSMUST00000132155.1	ENSMUST0000022262.1	ENSMUST00000131931.1	ENSMUST00000131544.7
ENSMUST00000187852.6	ENSMUST00000054491.5	ENSMUST00000159565.7	ENSMUST00000162316.1	ENSMUST00000029075.4	ENSMUST00000165324.1
ENSMUST00000104769.1	ENSMUST00000054491.5	ENSMUST00000093852.4	ENSMUST00000221314.1	ENSMUST00000072895.9	ENSMUST00000034029.7
ENSMUST00000225119.1	ENSMUST00000194279.5	ENSMUST00000215416.1	ENSMUST00000223266.1	ENSMUST00000109020.8	ENSMUST00000209490.1
ENSMUST00000181700.1	ENSMUST00000161949.7	ENSMUST00000213937.1	ENSMUST00000220826.1	ENSMUST00000108981.8	ENSMUST00000126174.1
ENSMUST00000091569.6	ENSMUST00000047630.6	ENSMUST00000213681.1	ENSMUST00000083604.1	ENSMUST00000108934.8	ENSMUST00000061923.4
ENSMUST00000225732.1	ENSMUST00000091259.8	ENSMUST00000176884.1	ENSMUST00000186183.1	ENSMUST00000041998.1	ENSMUST00000212722.1
ENSMUST00000222604.1	ENSMUST00000108228.7	ENSMUST00000139261.7	ENSMUST00000139438.1	ENSMUST00000108911.1	ENSMUST00000125695.2
ENSMUST00000022013.7	ENSMUST00000122581.2	ENSMUST00000034869.10	ENSMUST00000169960.9	ENSMUST00000103053.9	ENSMUST00000212810.1
ENSMUST00000036208.6	ENSMUST00000124606.2	ENSMUST00000215269.1	ENSMUST00000220727.1	ENSMUST00000193117.2	ENSMUST00000212558.1

ENSMUST00000091458.12	ENSMUST00000138563.8	ENSMUST00000055036.6	ENSMUST00000110516.2	ENSMUST00000202747.3	ENSMUST00000212986.1
ENSMUST00000091458.12	ENSMUST00000200585.4	ENSMUST00000050916.6	ENSMUST00000141194.7	ENSMUST00000057186.1	ENSMUST00000109410.3
ENSMUST00000083490.2	ENSMUST00000026866.14	ENSMUST00000034860.4	ENSMUST00000139064.9	ENSMUST00000169047.1	ENSMUST00000034375.10
ENSMUST00000159199.7	ENSMUST00000139771.2	ENSMUST00000041477.14	ENSMUST00000122926.1	ENSMUST00000172694.7	ENSMUST00000067512.7
ENSMUST00000151408.7	ENSMUST00000054387.7	ENSMUST000000217578.1	ENSMUST00000102972.5	ENSMUST00000172754.7	ENSMUST00000183365.1
ENSMUST00000165225.7	ENSMUST00000053764.6	ENSMUST000000217578.1	ENSMUST00000110383.7	ENSMUST00000108262.9	ENSMUST000000212764.1
ENSMUST00000225299.1	ENSMUST00000198510.4	ENSMUST00000175792.7	ENSMUST00000128315.1	ENSMUST00000164954.2	ENSMUST000000212003.1
ENSMUST00000133461.1	ENSMUST00000122210.1	ENSMUST00000128944.7	ENSMUST00000184136.1	ENSMUST00000198751.4	ENSMUST00000150680.1
ENSMUST00000054425.6	ENSMUST00000041115.6	ENSMUST00000130831.7	ENSMUST00000110273.8	ENSMUST00000108182.9	ENSMUST00000056157.13
ENSMUST00000022228.12	ENSMUST00000079300.12	ENSMUST00000056949.4	ENSMUST00000053265.7	ENSMUST00000040148.10	ENSMUST00000152420.7
ENSMUST00000223674.1	ENSMUST00000163008.7	ENSMUST00000098651.5	ENSMUST00000021870.11	ENSMUST00000203919.2	ENSMUST00000142578.7
ENSMUST00000092089.5	ENSMUST00000195685.1	ENSMUST00000042322.10	ENSMUST00000145810.1	ENSMUST00000181047.6	ENSMUST00000142578.7
ENSMUST00000099147.4	ENSMUST00000162098.8	ENSMUST00000041029.5	ENSMUST00000221359.1	ENSMUST00000118075.6	ENSMUST000000211867.1
ENSMUST00000190512.1	ENSMUST00000195708.1	ENSMUST00000145011.1	ENSMUST00000119341.1	ENSMUST00000059562.13	ENSMUST00000188193.1
ENSMUST00000187530.2	ENSMUST00000164216.5	ENSMUST00000122091.7	ENSMUST00000052747.3	ENSMUST00000198745.1	ENSMUST000000212914.1
ENSMUST00000225683.1	ENSMUST00000156457.7	ENSMUST00000217144.1	ENSMUST00000110111.3	ENSMUST00000197841.1	ENSMUST00000195989.1
ENSMUST00000170104.2	ENSMUST00000098990.9	ENSMUST00000041139.8	ENSMUST00000089798.4	ENSMUST00000029325.4	ENSMUST00000034413.7
ENSMUST00000170104.2	ENSMUST00000146862.1	ENSMUST00000054500.6	ENSMUST00000021898.5	ENSMUST00000176481.8	ENSMUST00000115592.7
ENSMUST00000170104.2	ENSMUST00000029709.6	ENSMUST00000093823.7	ENSMUST000000220691.1	ENSMUST00000029421.5	ENSMUST000000215255.1
ENSMUST00000170104.2	ENSMUST00000107543.7	ENSMUST00000184036.7	ENSMUST00000222580.1	ENSMUST00000190602.1	ENSMUST00000074986.6
ENSMUST00000170104.2	ENSMUST00000076048.4	ENSMUST00000184851.1	ENSMUST00000139184.7	ENSMUST00000078527.12	ENSMUST000000217461.1
ENSMUST00000163850.7	ENSMUST00000200410.1	ENSMUST0000008052.12	ENSMUST00000149858.1	ENSMUST00000135043.7	ENSMUST00000150395.7
ENSMUST00000224392.1	ENSMUST00000047660.4	ENSMUST00000183636.1	ENSMUST00000183653.1	ENSMUST00000029635.13	ENSMUST00000008573.8
ENSMUST00000055211.5	ENSMUST00000029521.4	ENSMUST00000024104.8	ENSMUST00000225488.1	ENSMUST00000047876.6	ENSMUST000000216649.1
ENSMUST00000096121.11	ENSMUST00000238714.1	ENSMUST00000125615.1	ENSMUST00000071703.5	ENSMUST00000047368.7	ENSMUST00000133904.1
ENSMUST00000059666.5	ENSMUST00000132256.7	ENSMUST00000057067.9	ENSMUST00000080766.7	ENSMUST00000029712.4	ENSMUST00000117389.7
ENSMUST00000225327.1	ENSMUST00000090746.2	ENSMUST00000216802.1	ENSMUST00000107989.6	ENSMUST00000107464.7	ENSMUST00000063782.11
ENSMUST00000145596.2	ENSMUST00000029462.9	ENSMUST00000098495.9	ENSMUST00000107989.6	ENSMUST00000124584.3	ENSMUST000000213706.1
ENSMUST00000102956.7	ENSMUST00000135812.2	ENSMUST00000034991.7	ENSMUST000000201563.3	ENSMUST00000239156.1	ENSMUST00000183422.1
ENSMUST00000225717.1	ENSMUST00000198712.4	ENSMUST00000034991.7	ENSMUST00000178651.1	ENSMUST00000013851.3	ENSMUST00000074740.4
ENSMUST00000048603.7	ENSMUST00000106860.5	ENSMUST00000165315.7	ENSMUST00000220595.1	ENSMUST00000183853.1	ENSMUST00000159603.1
ENSMUST00000022480.7	ENSMUST00000141694.1	ENSMUST00000215498.1	ENSMUST00000238355.1	ENSMUST00000141579.1	ENSMUST000000217418.1
ENSMUST00000061753.14	ENSMUST00000090678.10	ENSMUST00000113110.4	ENSMUST00000238355.1	ENSMUST00000127607.1	ENSMUST00000180670.2
ENSMUST00000178178.1	ENSMUST00000232302.1	ENSMUST00000035142.7	ENSMUST00000174606.1	ENSMUST00000197696.1	ENSMUST00000052686.3
ENSMUST00000123879.7	ENSMUST00000141387.3	ENSMUST00000038648.10	ENSMUST00000099412.2	ENSMUST00000152731.1	ENSMUST00000220303.1
ENSMUST00000022386.14	ENSMUST00000106625.9	ENSMUST00000085114.7	ENSMUST00000077337.8	ENSMUST00000179429.5	ENSMUST000000215293.1
ENSMUST00000227404.1	ENSMUST00000180063.7	ENSMUST00000074617.6	ENSMUST00000022100.6	ENSMUST00000029453.12	ENSMUST00000170489.1
ENSMUST00000022398.14	ENSMUST00000059946.10	ENSMUST00000146794.3	ENSMUST00000208418.1	ENSMUST00000090697.10	ENSMUST000000217538.1
ENSMUST00000061614.7	ENSMUST00000198335.1	ENSMUST00000220102.1	ENSMUST00000126960.7	ENSMUST00000106822.1	ENSMUST00000114548.7
ENSMUST00000180397.2	ENSMUST00000132199.7	ENSMUST00000220102.1	ENSMUST00000128120.1	ENSMUST00000190356.1	ENSMUST00000171217.1
ENSMUST00000022496.8	ENSMUST00000196051.1	ENSMUST00000111820.3	ENSMUST00000199450.4	ENSMUST0000004134.10	ENSMUST000000214117.1
ENSMUST00000160745.1	ENSMUST00000137404.7	ENSMUST00000111773.9	ENSMUST00000022119.5	ENSMUST00000004140.10	ENSMUST00000146509.7
ENSMUST00000022620.10	ENSMUST00000198955.4	ENSMUST00000039610.9	ENSMUST00000022213.7	ENSMUST00000040097.13	ENSMUST00000132410.1
ENSMUST00000138160.7	ENSMUST00000143830.2	ENSMUST00000065196.12	ENSMUST00000222948.1	ENSMUST00000141135.4	ENSMUST00000098760.4
ENSMUST00000159144.1	ENSMUST00000072271.12	ENSMUST00000177637.1	ENSMUST00000077672.11	ENSMUST00000083479.2	ENSMUST00000034822.11
ENSMUST00000022592.7	ENSMUST00000043937.8	ENSMUST00000169931.7	ENSMUST00000180396.1	ENSMUST00000136147.7	ENSMUST00000053568.1
ENSMUST00000183564.1	ENSMUST00000079085.10	ENSMUST00000077706.9	ENSMUST00000238746.1	ENSMUST00000197793.4	ENSMUST00000135050.1
ENSMUST00000071546.13	ENSMUST00000056758.8	ENSMUST00000213272.1	ENSMUST00000054425.6	ENSMUST00000147041.9	ENSMUST00000159012.1
ENSMUST00000228115.1	ENSMUST00000029805.12	ENSMUST00000214074.1	ENSMUST00000221034.1	ENSMUST00000197118.4	ENSMUST00000034920.10
ENSMUST00000032898.8	ENSMUST00000090171.6	ENSMUST00000145302.1	ENSMUST00000022145.14	ENSMUST00000122615.1	ENSMUST00000148449.7
ENSMUST00000227372.1	ENSMUST0000004232.9	ENSMUST00000123120.1	ENSMUST00000191312.1	ENSMUST00000090127.6	ENSMUST00000034955.7
ENSMUST00000144926.1	ENSMUST00000161312.7	ENSMUST00000069763.2	ENSMUST00000231096.1	ENSMUST00000043325.8	ENSMUST000000215724.1
ENSMUST00000069451.10	ENSMUST00000200020.4	ENSMUST00000123014.1	ENSMUST00000168684.1	ENSMUST00000120310.1	ENSMUST00000152570.1
ENSMUST00000180518.1	ENSMUST00000029948.14	ENSMUST00000153345.1	ENSMUST00000183663.7	ENSMUST00000039450.4	ENSMUST000000215370.1
ENSMUST00000110689.4	ENSMUST00000029941.15	ENSMUST00000039026.7	ENSMUST00000223819.1	ENSMUST00000106134.3	ENSMUST00000183878.1
ENSMUST00000118365.2	ENSMUST00000029929.11	ENSMUST00000033450.2	ENSMUST00000146674.1	ENSMUST00000046614.9	ENSMUST00000150850.1
ENSMUST00000159046.1	ENSMUST00000039164.3	ENSMUST00000074861.8	ENSMUST00000223268.1	ENSMUST00000134701.1	ENSMUST00000151676.1
ENSMUST00000145428.7	ENSMUST00000005630.10	ENSMUST00000067782.7	ENSMUST00000178142.1	ENSMUST00000196791.1	ENSMUST00000239133.1
ENSMUST00000110540.7	ENSMUST00000128362.1	ENSMUST00000069926.13	ENSMUST00000096171.11	ENSMUST00000118539.1	ENSMUST00000189777.1
ENSMUST00000188888.6	ENSMUST00000143410.6	ENSMUST00000080035.10	ENSMUST00000096171.11	ENSMUST00000142297.1	ENSMUST00000034909.10

ENSMUST00000166873.8	ENSMUST00000192383.5	ENSMUST00000131554.2	ENSMUST00000096171.11	ENSMUST00000029908.7	ENSMUST00000129771.2
ENSMUST00000176801.1	ENSMUST00000103010.3	ENSMUST00000086470.2	ENSMUST00000096171.11	ENSMUST00000132173.7	ENSMUST00000035048.11
ENSMUST00000110408.2	ENSMUST00000119374.7	ENSMUST00000033738.7	ENSMUST00000096171.11	ENSMUST00000107942.8	ENSMUST00000185719.1
ENSMUST00000042702.6	ENSMUST00000029922.13	ENSMUST00000156959.1	ENSMUST00000096171.11	ENSMUST00000107884.2	ENSMUST00000035155.7
ENSMUST00000022871.6	ENSMUST00000037416.12	ENSMUST00000033539.12	ENSMUST00000100895.9	ENSMUST00000175020.1	ENSMUST00000035163.9
ENSMUST00000227018.1	ENSMUST00000155691.1	ENSMUST00000036333.13	ENSMUST00000100895.9	ENSMUST00000055028.8	ENSMUST00000157006.7
ENSMUST00000228684.1	ENSMUST00000135323.1	ENSMUST00000197180.5	ENSMUST00000184251.1	ENSMUST00000044773.11	ENSMUST00000098441.9
ENSMUST00000227582.1	ENSMUST00000108055.8	ENSMUST00000197180.5	ENSMUST00000163392.2	ENSMUST00000156200.7	ENSMUST00000148440.7
ENSMUST0000013755.11	ENSMUST00000107958.7	ENSMUST00000049420.3	ENSMUST00000112669.9	ENSMUST00000095097.2	ENSMUST00000194079.1
ENSMUST00000226257.1	ENSMUST00000107824.8	ENSMUST00000046565.12	ENSMUST00000022296.6	ENSMUST00000043056.8	ENSMUST00000197248.4
ENSMUST00000140044.7	ENSMUST00000107749.3	ENSMUST00000096368.3	ENSMUST00000176555.7	ENSMUST00000029987.9	ENSMUST00000184024.1
ENSMUST00000228416.1	ENSMUST00000029991.2	ENSMUST00000079322.11	ENSMUST00000223558.1	ENSMUST00000141473.1	ENSMUST00000197321.4
ENSMUST0000022921.6	ENSMUST00000030036.5	ENSMUST00000156473.7	ENSMUST00000073870.6	ENSMUST00000151481.7	ENSMUST00000149308.3
ENSMUST00000022921.6	ENSMUST00000107359.8	ENSMUST00000033689.2	ENSMUST00000199094.1	ENSMUST00000142837.2	ENSMUST00000220102.1
ENSMUST00000227081.1	ENSMUST00000102819.9	ENSMUST00000042664.9	ENSMUST00000161766.7	ENSMUST00000107157.8	ENSMUST00000135338.2
ENSMUST00000081361.2	ENSMUST00000084433.4	ENSMUST00000118314.7	ENSMUST00000073309.4	ENSMUST00000233522.1	ENSMUST00000047013.3
ENSMUST00000022925.9	ENSMUST00000078090.11	ENSMUST00000055497.14	ENSMUST00000037739.7	ENSMUST00000107094.1	ENSMUST00000044220.10
ENSMUST00000050544.7	ENSMUST00000094992.1	ENSMUST00000149154.7	ENSMUST00000226565.1	ENSMUST00000176162.7	ENSMUST00000048121.12
ENSMUST00000182075.7	ENSMUST00000129908.1	ENSMUST00000033617.12	ENSMUST00000228429.1	ENSMUST00000124547.1	ENSMUST00000035110.10
ENSMUST00000230569.1	ENSMUST00000183406.1	ENSMUST00000113185.8	ENSMUST00000070125.5	ENSMUST00000124547.1	ENSMUST00000215872.1
ENSMUST00000202826.1	ENSMUST00000075448.12	ENSMUST00000078605.6	ENSMUST00000111956.8	ENSMUST00000173119.7	ENSMUST00000026890.5
ENSMUST00000186014.1	ENSMUST00000041284.9	ENSMUST00000153742.1	ENSMUST00000022327.12	ENSMUST00000106804.1	ENSMUST00000150541.1
ENSMUST00000166694.1	ENSMUST00000087285.4	ENSMUST00000101205.2	ENSMUST00000227253.1	ENSMUST00000238584.1	ENSMUST00000151112.1
ENSMUST00000229055.1	ENSMUST00000051043.3	ENSMUST00000067841.7	ENSMUST00000191317.1	ENSMUST00000043616.6	ENSMUST00000050434.5
ENSMUST00000017086.4	ENSMUST00000126324.6	ENSMUST00000117991.1	ENSMUST00000228505.1	ENSMUST00000053157.6	ENSMUST00000140106.7
ENSMUST00000053239.3	ENSMUST00000106770.7	ENSMUST00000165760.1	ENSMUST00000100691.3	ENSMUST00000103245.1	ENSMUST00000046557.5
ENSMUST00000023061.6	ENSMUST00000030367.14	ENSMUST00000079945.10	ENSMUST00000096899.2	ENSMUST00000063531.4	ENSMUST00000152730.3
ENSMUST00000096347.3	ENSMUST00000030361.10	ENSMUST00000112401.7	ENSMUST00000184478.1	ENSMUST00000094894.3	ENSMUST00000115058.7
ENSMUST00000230612.1	ENSMUST00000069271.4	ENSMUST00000071204.11	ENSMUST00000159611.8	ENSMUST00000106521.1	ENSMUST00000114904.9
ENSMUST00000230860.1	ENSMUST00000183919.1	ENSMUST00000154424.7	ENSMUST00000199271.1	ENSMUST00000106459.7	ENSMUST00000069509.3
ENSMUST00000057236.4	ENSMUST00000106658.7	ENSMUST00000134085.1	ENSMUST00000128231.1	ENSMUST00000044823.3	ENSMUST00000151768.1
ENSMUST00000089178.10	ENSMUST00000106651.8	ENSMUST00000238211.1	ENSMUST00000022826.6	ENSMUST00000150148.1	ENSMUST00000114629.3
ENSMUST00000229387.1	ENSMUST00000030274.6		ENSMUST00000225698.1	ENSMUST00000030263.8	ENSMUST00000104655.1
			ENSMUST00000160334.7	ENSMUST00000153968.1	ENSMUST00000114517.1
			ENSMUST00000022517.8	ENSMUST00000052876.2	ENSMUST00000114109.7
			ENSMUST00000193208.1	ENSMUST00000185054.1	ENSMUST00000033545.5
			ENSMUST00000225355.1	ENSMUST00000144298.1	ENSMUST00000135237.8
			ENSMUST00000022623.12	ENSMUST00000030575.14	ENSMUST00000009814.9
			ENSMUST00000176161.7	ENSMUST00000147634.7	ENSMUST00000138614.1
			ENSMUST00000228911.1	ENSMUST00000139884.1	ENSMUST00000181020.8
			ENSMUST00000161082.1	ENSMUST00000094666.3	ENSMUST00000150434.7
			ENSMUST00000036653.4	ENSMUST00000105951.7	ENSMUST00000113379.7
			ENSMUST00000228470.1	ENSMUST00000185007.1	ENSMUST00000113154.7
			ENSMUST00000190818.6	ENSMUST00000068830.3	ENSMUST00000087316.5
			ENSMUST00000095625.10	ENSMUST00000153505.1	ENSMUST00000112740.1
			ENSMUST00000228576.1	ENSMUST00000238480.1	ENSMUST00000112604.7
			ENSMUST00000069334.7	ENSMUST00000030539.9	ENSMUST00000026383.3
			ENSMUST00000226784.1	ENSMUST00000183998.1	ENSMUST00000127673.1
			ENSMUST00000228216.1	ENSMUST00000105032.3	ENSMUST00000039424.13
			ENSMUST00000188582.1	ENSMUST00000105032.3	ENSMUST00000038665.5
			ENSMUST00000154206.7	ENSMUST00000077582.13	ENSMUST00000141356.1
			ENSMUST00000022746.12	ENSMUST00000030508.13	ENSMUST00000150433.7
			ENSMUST00000058593.9	ENSMUST00000122051.1	ENSMUST00000033665.8
			ENSMUST00000226928.1	ENSMUST00000131932.1	ENSMUST00000006154.7
			ENSMUST00000166524.8	ENSMUST00000175787.1	ENSMUST00000000412.2
			ENSMUST00000160236.7	ENSMUST00000152323.1	ENSMUST00000112161.7
			ENSMUST00000227861.1	ENSMUST00000105683.8	ENSMUST00000036753.11
			ENSMUST00000061318.8	ENSMUST00000105646.2	

**Table S 2 GO term enrichment results of the DICE analysis of RNA-seq clusters 1, 2, and 3.**

Cluster 1 (p-value threshold <= 0e0)	Cluster 2 (p-value threshold <= 0e0)	Cluster 3 (p-value threshold <= 4e-10)
anatomical structure development	animal organ morphogenesis	anatomical structure development
animal development	brain development	cell differentiation
cell development	carbohydrate derivative biosynthetic process	developmental process
cell differentiation	cardiovascular system development	multicellular organism development
cellular developmental process	cell cycle phase transition	regulation of multicellular organismal process
developmental process	cell morphogenesis involved in neuron differentiation	regulation of response to stimulus
localization	cell projection assembly	system development
multicellular organism development	cell projection morphogenesis	
regulation of biological quality	cellular amide metabolic process	
regulation of multicellular organismal process	cellular component disassembly	
system development	cellular lipid metabolic process	
	cellular response to starvation	
	central nervous system development	
	chromosome segregation	
	cofactor metabolic process	
	covalent chromatin modification	
	cytoskeleton-dependent intracellular transport	
	DNA recombination	
	double-strand break repair	
	embryonic morphogenesis	
	embryonic organ development	
	endoplasmic reticulum to Golgi vesicle-mediated transport	
	endosomal transport	
	energy derivation by oxidation of organic compounds	
	enzyme linked receptor protein signaling pathway	
	establishment of protein localization to organelle	
	establishment of RNA localization	
	generation of precursor metabolites and energy	
	glycerophospholipid metabolic process	
	head development	
	heart development	
	heart morphogenesis	
	histone modification	
	ion transport	
	locomotion	
	methylation	
	microtubule-based movement	
	microtubule-based transport	
	morphogenesis of an epithelium	
	mRNA splicing	
	negative regulation of cell differentiation	
	negative regulation of cell population proliferation	
	negative regulation of intracellular signal transduction	
	negative regulation of multicellular organismal process	
	negative regulation of organelle organization	
	negative regulation of phosphorylation	
	negative regulation of protein phosphorylation	
	neuron projection morphogenesis	
	nuclear chromosome segregation	

	nuclear division	
	nucleic acid transport	
	nucleobase-containing compound transport	
	nucleobase-containing small molecule metabolic process	
	organelle assembly	
	organelle transport along microtubule	
	organophosphate biosynthetic process	
	phospholipid metabolic process	
	plasma membrane bounded cell projection assembly	
	plasma membrane bounded cell projection morphogenesis	
	positive regulation of apoptotic signaling pathway	
	positive regulation of binding	
	positive regulation of catabolic process	
	positive regulation of cell communication	
	positive regulation of cell cycle	
	positive regulation of cell cycle process	
	positive regulation of cell development	
	positive regulation of cell migration	
	positive regulation of cell motility	
	positive regulation of cell population proliferation	
	positive regulation of cell projection organization	
	positive regulation of cellular amide metabolic process	
	positive regulation of cellular catabolic process	
	positive regulation of cellular component biogenesis	
	positive regulation of cellular component movement	
	positive regulation of cellular protein localization	
	positive regulation of chromosome organization	
	positive regulation of DNA metabolic process	
	positive regulation of hydrolase activity	
	positive regulation of kinase activity	
	positive regulation of locomotion	
	positive regulation of nervous system development	
	positive regulation of neurogenesis	
	positive regulation of phosphorylation	
	positive regulation of protein binding	
	positive regulation of protein kinase activity	
	positive regulation of protein phosphorylation	
	positive regulation of response to stimulus	
	positive regulation of signaling	
	positive regulation of transport	
	posttranscriptional regulation of gene expression	
	proteasomal protein catabolic process	
	proteasome-mediated ubiquitin-dependent protein catabolic process	
	protein acylation	
	protein folding	
	protein homooligomerization	
	protein localization to membrane	
	protein localization to nucleus	
	protein modification by small protein conjugation	
	protein modification by small protein conjugation or removal	
	protein ubiquitination	
	protein-containing complex localization	



	proteolysis	
	regulation of actin cytoskeleton organization	
	regulation of actin filament-based process	
	regulation of anatomical structure size	
	regulation of apoptotic signaling pathway	
	regulation of autophagy	
	regulation of cell adhesion	
	regulation of cell cycle phase transition	
	regulation of cell migration	
	regulation of cell morphogenesis	
	regulation of cell motility	
	regulation of DNA replication	
	regulation of DNA-binding transcription factor activity	
	regulation of establishment of protein localization	
	regulation of growth	
	regulation of intracellular transport	
	regulation of mitotic cell cycle phase transition	
	regulation of mRNA catabolic process	
	regulation of mRNA stability	
	regulation of nuclear division	
	regulation of peptide transport	
	regulation of protein binding	
	regulation of protein complex assembly	
	regulation of protein stability	
	regulation of protein transport	
	regulation of response to DNA damage stimulus	
	regulation of RNA stability	
	regulation of supramolecular fiber organization	
	reproduction	
	reproductive process	
	reproductive structure development	
	reproductive system development	
	response to abiotic stimulus	
	response to chemical	
	response to endoplasmic reticulum stress	
	response to oxidative stress	
	response to radiation	
	response to starvation	
	ribonucleoprotein complex subunit organization	
	RNA localization	
	RNA splicing	
	RNA transport	
	sister chromatid segregation	
	supramolecular fiber organization	
	tissue morphogenesis	
	transmembrane transport	
	transport along microtubule	
	tRNA metabolic process	
	tube morphogenesis	
	vasculature development	
	vesicle organization	

**Table S 3 Overview of total peak numbers, assignment to regulatory elements and number of peaks containing one of the indicated motifs.**

Time point	TF	Rep	Peak no. from total						
			Total	Enhancer	Promoter	NANOG motif	OCT4 motif	SOX2 motif	OCT4::SOX2 motif
Mito	NANOG	1	193	39	47	111	26	53	29
AT	NANOG	1	8012	1349	1588	5122	1805	3065	2183
eG1-1 50K	NANOG	1	1602	268	290	1121	403	708	530
eG1-1	NANOG	2	17610	2610	2843	12813	4450	7366	5051
eG1-2	NANOG	2	10936	1453	1864	7858	2834	4702	3505
eG1-3	NANOG	2	21974	3392	3910	15646	5472	8853	6012
eG1-4	NANOG	2	9611	1397	1857	5482	2111	3301	2708
Mito	OCT4	1	116	36	66	14	4	5	0
AT	OCT4	1	425	64	148	264	134	150	169
eG1-1 50K	OCT4	1	797	124	196	561	271	364	346
eG1-1	OCT4	3	20702	3160	3857	14423	6795	6966	7815
eG1-2	OCT4	3	11041	1647	1974	7315	3731	4224	4370
eG1-3	OCT4	3	13751	2071	2602	5877	2840	3163	3106
eG1-4	OCT4	3	10372	1735	2087	2983	1564	1809	1908
Mito	SOX2	1	47	1	36	20	3	10	2
AT	SOX2	1	1117	234	305	788	290	576	402
eG1-1 50K	SOX2	1	2038	265	445	1360	481	1058	685
eG1-1	SOX2	3	21303	3766	4374	13771	4814	9604	5942
eG1-2	SOX2	2	18610	2757	3408	12154	4846	8517	6048
eG1-3	SOX2	3	15923	2282	2818	10603	4317	7344	5486
eG1-4	SOX2	2	18438	3237	3595	12076	4635	8416	5780

**Table S 4 Total number of peaks in each classified region based on differential binding analysis.**

Cell line	Depletion	TF	Medium	Classification	Peak number	Percent total
ZHBTc4	OCT4	NANOG	S2iL	increased	576	1.4
ZHBTc4	OCT4	NANOG	S2iL	unchanged	33935	81.6
ZHBTc4	OCT4	NANOG	S2iL	decreased	7059	17.0
ZHBTc4	OCT4	NANOG	SL	increased	8236	24.6
ZHBTc4	OCT4	NANOG	SL	unchanged	22559	67.3
ZHBTc4	OCT4	NANOG	SL	decreased	2742	8.2
2TS22C	SOX2	NANOG	S2iL	increased	12	0.1
2TS22C	SOX2	NANOG	S2iL	unchanged	7869	86.9
2TS22C	SOX2	NANOG	S2iL	decreased	1178	13.0
ZHBTc4	OCT4	SOX2	S2iL	increased	469	1.8
ZHBTc4	OCT4	SOX2	S2iL	unchanged	17527	67.8
ZHBTc4	OCT4	SOX2	S2iL	decreased	7851	30.4
ZHBTc4	OCT4	SOX2	SL	increased	2007	7.0
ZHBTc4	OCT4	SOX2	SL	unchanged	24225	84.5
ZHBTc4	OCT4	SOX2	SL	decreased	2449	8.5
44iN	NANOG	SOX2	S2iL	increased	95	0.2
44iN	NANOG	SOX2	S2iL	unchanged	38721	86.9
44iN	NANOG	SOX2	S2iL	decreased	5732	12.9
2TS22C	SOX2	OCT4	S2iL	increased	25	0.1
2TS22C	SOX2	OCT4	S2iL	unchanged	24142	84.3
2TS22C	SOX2	OCT4	S2iL	decreased	4472	15.6
44iN	NANOG	OCT4	S2iL	increased	167	0.4
44iN	NANOG	OCT4	S2iL	unchanged	37130	89.3
44iN	NANOG	OCT4	S2iL	decreased	4293	10.3

**Table S 5 Total number of peaks on the Venn diagrams in each classified region based on differential binding analysis and the area crossed between the indicated samples.**

Figure	Panel	Sample	Element	Class	TF loss	Color	Area	Peak number
3	G	$\Delta$ eG12/eG11	Enhancer	decrease	NA	steelblue4	1	1059
3	G	$\Delta$ eG13/eG12	Enhancer	decrease	NA	forestgreen	2	424
3	G	$\Delta$ eG14/eG13	Enhancer	decrease	NA	gold	3	761
3	G	cross_area	Enhancer	decrease	NA	NA	12	169
3	G	cross_area	Enhancer	decrease	NA	NA	13	464
3	G	cross_area	Enhancer	decrease	NA	NA	23	136
3	G	cross_area	Enhancer	decrease	NA	NA	123	50
3	G	$\Delta$ eG12/eG11	Enhancer	increase	NA	steelblue4	1	810
3	G	$\Delta$ eG13/eG12	Enhancer	increase	NA	forestgreen	2	1430
3	G	$\Delta$ eG14/eG13	Enhancer	increase	NA	gold	3	1107
3	G	cross_area	Enhancer	increase	NA	NA	12	570
3	G	cross_area	Enhancer	increase	NA	NA	13	519
3	G	cross_area	Enhancer	increase	NA	NA	23	837
3	G	cross_area	Enhancer	increase	NA	NA	123	355
3	G	$\Delta$ eG12/eG11	Promoter	decrease	NA	steelblue4	1	10323
3	G	$\Delta$ eG13/eG12	Promoter	decrease	NA	forestgreen	2	4071
3	G	$\Delta$ eG14/eG13	Promoter	decrease	NA	gold	3	7085
3	G	cross_area	Promoter	decrease	NA	NA	12	1455
3	G	cross_area	Promoter	decrease	NA	NA	13	3834
3	G	cross_area	Promoter	decrease	NA	NA	23	1143
3	G	cross_area	Promoter	decrease	NA	NA	123	368
3	G	$\Delta$ eG12/eG11	Promoter	increase	NA	steelblue4	1	9103
3	G	$\Delta$ eG13/eG12	Promoter	increase	NA	forestgreen	2	15355
3	G	$\Delta$ eG14/eG13	Promoter	increase	NA	gold	3	12341
3	G	cross_area	Promoter	increase	NA	NA	12	6487
3	G	cross_area	Promoter	increase	NA	NA	13	5852
3	G	cross_area	Promoter	increase	NA	NA	23	9413
3	G	cross_area	Promoter	increase	NA	NA	123	4011
7	B	NANOG_S2iL	NA	increased	OCT4	darkblue	1	576
7	B	NANOG_SL	NA	increased	OCT4	lightblue	2	8236
7	B	cross_area	NA	increased	OCT4	NA	12	402
7	B	NANOG_S2iL	NA	unchanged	OCT4	darkblue	1	33935
7	B	NANOG_SL	NA	unchanged	OCT4	lightblue	2	22559
7	B	cross_area	NA	unchanged	OCT4	NA	12	8659
7	B	NANOG_S2iL	NA	decreased	OCT4	darkblue	1	7059
7	B	NANOG_SL	NA	decreased	OCT4	lightblue	2	2742
7	B	cross_area	NA	decreased	OCT4	NA	12	2117
7	C	NANOG_SL	NA	increased	OCT4	lightblue	1	8236

7	C	SOX2_SL	NA	increased	OCT4	gold	2	2007
7	C	cross_area	NA	increased	OCT4	NA	12	1591
7	C	NANOG_SL	NA	unchanged	OCT4	lightblue	1	22559
7	C	SOX2_SL	NA	unchanged	OCT4	gold	2	24225
7	C	cross_area	NA	unchanged	OCT4	NA	12	8509
7	C	NANOG_SL	NA	decreased	OCT4	lightblue	1	2742
7	C	SOX2_SL	NA	decreased	OCT4	gold	2	4600
7	C	cross_area	NA	decreased	OCT4	NA	12	1564
7	F	NANOG_SL	NA	increased	OCT4	lightblue	1	8236
7	F	GATA6	NA	increased	NA	forestgreen	2	23735
7	F	cross_area	NA	increased	NA	NA	12	1052
7	F	NANOG_SL	NA	unchanged	OCT4	lightblue	1	22559
7	F	GATA6	NA	unchanged	NA	forestgreen	2	23735
7	F	cross_area	NA	unchanged	NA	NA	12	1918
7	F	NANOG_SL	NA	decreased	OCT4	lightblue	1	2742
7	F	GATA6	NA	decreased	NA	forestgreen	2	23735
7	F	cross_area	NA	decreased	NA	NA	12	168
S4	C	NANOG	NA	increased	OCT4	darkblue	1	576
S4	C	SOX2	NA	increased	OCT4	darkgoldenrod2	2	469
S4	C	cross_area	NA	increased	OCT4	NA	12	180
S4	C	NANOG	NA	unchanged	OCT4	darkblue	1	33935
S4	C	SOX2	NA	unchanged	OCT4	darkgoldenrod2	2	17527
S4	C	cross_area	NA	unchanged	OCT4	NA	12	11789
S4	C	NANOG	NA	decreased	OCT4	darkblue	1	7059
S4	C	SOX2	NA	decreased	OCT4	darkgoldenrod2	2	7851
S4	C	cross_area	NA	decreased	OCT4	NA	12	4787
S4	C	NANOG	NA	increased	SOX2	darkblue	1	12
S4	C	OCT4	NA	increased	SOX2	darkred	2	25
S4	C	cross_area	NA	increased	SOX2	NA	12	0
S4	C	NANOG	NA	unchanged	SOX2	darkblue	1	7869
S4	C	OCT4	NA	unchanged	SOX2	darkred	2	24142
S4	C	cross_area	NA	unchanged	SOX2	NA	12	4781
S4	C	NANOG	NA	decreased	SOX2	darkblue	1	1178
S4	C	OCT4	NA	decreased	SOX2	darkred	2	4472
S4	C	cross_area	NA	decreased	SOX2	NA	12	913
S5	A	OCT4	NA	increased	NANOG	darkred	1	167
S5	A	SOX2	NA	increased	NANOG	darkgoldenrod2	2	95
S5	A	cross_area	NA	increased	NANOG	NA	12	29
S5	A	OCT4	NA	unchanged	NANOG	darkred	1	37130
S5	A	SOX2	NA	unchanged	NANOG	darkgoldenrod2	2	38721
S5	A	cross_area	NA	unchanged	NANOG	NA	12	3164
S5	A	OCT4	NA	decreased	NANOG	darkred	1	4293

S5	A	SOX2	NA	decreased	NANOG	darkgoldenrod2	2	5732
S5	A	cross_area	NA	decreased	NANOG	NA	12	3164

## Chapter 3: Conclusion

### 3.1 Discussion of the results

In this project, we introduced a novel fluorescent reporter system that allowed us to sort AT-enriched cells and different temporal bins of eG1 without drug synchronization. The Cdt1-MD reporter is especially useful for studying the transition between mitosis and the G1 phase with a higher temporal resolution than previous reporter systems (Kadauke et al., 2012; Sakaue-Sawano et al., 2017, 2008). Furthermore, since we avoid the usage of drugs, we circumvent artificial changes in gene expression, chromatin accessibility, TF binding (C-S Hsiung et al., 2016; Palozola et al., 2017), and different lag times upon drug release (Sarnataro et al., 2021). However, as for other reporter systems that rely on constitutive active promoter expression, there is substantial variability in the fluorescence intensities of individual cells (Wang et al., 2008). Furthermore, we calculated the time in the different temporal bins based on the average G1 time measured with flow cytometry and linear regression on the microscopy data. Both factors contribute to blurring the absolute time represented in the temporal bins. Hence, it would be important to calculate a more accurate average time upon cytokinesis in the temporal bins, for example using machine learning approaches that can combine both datasets.

Using our reporter system, we identified anaphase-telophase as the first timepoint of TF rebinding during mitotic exit, which is in line with the restoration of gene expression (C-S Hsiung et al., 2016; Palozola et al., 2017) and reformation of enhancer-loops in anaphase-telophase (Zhang et al., 2019). However, our AT-enriched population contained only roughly 30 % of anaphase-telophase cells. Thus, we expect that a higher enrichment of AT cells and a larger cell quantity would yield a higher enrichment and a better signal-to-noise ratio for TF binding, respectively. This would allow us to dissect the primary binding events from later ones in the different temporal eG1 bins more precisely. To obtain a purer population, high-speed image-enabled cell sorting could be used, which would facilitate the specific collection of anaphase and telophase cells (Schraivogel et al., 2022). However, sorting a high enough cell number of different mitotic phases to do ChIP-seq in bulk would take several days. Nonetheless, with recent advances in the genomics field, such as CUT&RUN (Skene and Henikoff, 2017) and CUT&Tag (Kaya-Okur et al., 2019), or even single-cell ChIP-seq (Grosselin et al., 2019), it could be possible to study the TF binding events throughout mitosis on a small and pure mitotic cell population.

Moreover, we performed ChIP-seq on OSN on unsynchronized mitotic cells, and we confirmed that all three TFs are largely excluded from the mitotic chromatin. We found that the sites that remain occupied by OS are mainly non-specifically bound, while NANOG is bound specifically

to its motif. However, the abundance of the NANOG motif was overall higher in different temporal bins compared to OS, suggesting that it has a higher preference for site-specific binding. NANOG depletion from mitotic chromatin is in agreement with previous studies that looked into mitotic chromatin association with IF (Festuccia et al., 2019), live cell imaging (Deluz et al., 2016; Festuccia et al., 2019; Liu et al., 2017; Raccaud et al., 2019), or mitotic chromatin binding using ChIP-seq (Festuccia et al., 2019). Our results for the loss of OCT4 and SOX2 binding to mitotic chromatin are in accordance with two previous studies (Deluz et al., 2016; Festuccia et al., 2019). However, another study reported that a high number of binding sites remain occupied in a site-specific manner by OS in mitosis (Liu et al., 2017). This discrepancy might be due to a much harsher synchronization of cells with nocodazole (200 µg/ml vs. 50-200 ng/µl) compared to the other studies (Deluz et al., 2016; Festuccia et al., 2019) and to unsynchronized mitotic cells (this thesis). Additional factors, such as differences in chromatin fixation (Festuccia et al., 2019) and cell culture medium conditions, might contribute to the strong deviation of peak numbers between the studies. Since nocodazole synchronization strongly interferes with gene expression and chromatin accessibility (Shlyueva et al., 2022), we anticipate that our results acquired without cell cycle synchronization are more physiologically relevant.

We found that most loci are occupied by OSN already in eG1-1. To decipher different TF binding redistributions through eG1, we used TMM-normalization to account for technical variation. It is important to note that upon TMM-normalization, the quantitative aspect of the ChIP-seq signal based on spike-in normalization is masked. Therefore, we cannot exclude that some true temporal changes in global signal enrichment are lost. However, we chose TMM for normalization as we observed that the change between different eG1 bins for each TF is similar, thus assuming that their overall binding does not quantitatively differ between samples (Robinson and Oshlack, 2010). Hence, to further corroborate that OSN has different preferences of chromatin accessibility and dynamics through eG1, it would be useful to use complementary methods such as single-molecule imaging and ATAC-seq (Chen et al., 2016). We combined our analysis of TF redistribution through mitotic exit with acute depletion of OCT4, SOX2, or NANOG using a doxycycline-inducible system (Festuccia et al., 2012; Masui et al., 2007; Niwa et al., 2000). We found that OCT4 and SOX2 coordinate NANOG occupancy genome-wide, while NANOG in return stabilizes the binding of OCT4 and SOX2. Furthermore, during the progression of naïve ESCs towards a more advanced developmental stage, OCT4 is required to maintain NANOG and SOX2 at pluripotency loci, as its loss results in increased binding of NANOG and SOX2 to sites involved in further differentiation. These results were obtained employing a differential binding analysis of OCT4, SOX2, or NANOG in the presence or absence of one of the TFs. While we identified only a small number of loci that significantly increased in TF binding, through visual inspection, we concluded that they were indeed



affected and not noisy signal enrichment. Another point to keep into account, the depletion data was acquired upon doxycycline addition or removal, which takes 24-26 h to remove the target protein. Thus, we cannot exclude that some significant binding changes are the result of secondary effects. Therefore, it would be important to confirm the significantly affected loci through the use of a quicker degradation system, such as the auxin-inducible system (Nishimura et al., 2009). Furthermore, we combined cells grown in various medium conditions (2iL, S2iL, SL) in this analysis. As we could observe from our differential binding analysis, the interaction between OSN varied quite drastically upon the depletion of OCT4 in different cell culture media. Hence, when comparing the effects of OS depletion in the NANOG clusters, it would be best to have the exact same medium conditions. Another interesting experiment would be to deplete two TFs at the same time in the same cell line. This would allow to study whether the new NANOG binding sites in the absence of OCT4 are indeed result of NANOG redirection by SOX2. If this is the case, we would expect that similar to our results, upon loss of OCT4 and SOX2, NANOG would not bind anymore to these loci, and we could exclude eventual differences between stem cell lines.

## 3.2 Future research

We identified three NANOG clusters that either increased, decreased, or maintained NANOG binding through eG1 and depend to different extents on OS as confirmed by OS depletion in asynchronous cells. To more specifically decipher the functional roles of OSN during mitotic exit, it would be necessary to transiently deplete the TFs during this time window. Previous studies depleted OCT4 (Friman et al., 2019; Liu et al., 2017) or SOX2 (Deluz et al., 2016) during the metaphase-anaphase transition using the MD strategy (Kadauke et al., 2012). However, the addition of the MD does not fully deplete the fusion protein (Deluz et al., 2016; Liu et al., 2017) and most importantly, TFs remain depleted during the first 2 hours of G1. Thus, future studies of protein depletion during mitotic exit would require other approaches to allow both rapid TF depletion and recovery, such as the optogenetics-based inducible relocation system (Farrants et al., 2020). However, this would still imply the use of drug synchronization to specifically relocate the fusion protein during mitosis and mitotic exit. Although nocodazole has been widely used, we already stressed the disadvantages of the drug. Since it was proposed that using a CDK1 inhibitor results in less drastic changes in gene expression and chromatin accessibility (Shlyueva et al., 2022), this would already represent an improvement over nocodazole-based cell cycle synchronization. The drawback of this system is that cells would be inhibited already in G2, thus, depleting the fusion protein from chromatin already before mitotic entry. Therefore, combining the results of OSN depletion

using the MD strategy and chromatin depletion with relocation systems would allow us to obtain more meaningful results.

We also found that the interaction between OSN changed significantly when OCT4 was depleted in naïve or at a more advanced developmental stage. Thus, we expect a similar change in the interaction between OSN upon depletion of SOX2 or NANOG at an advanced developmental stage and even stronger in cells that display more restricted pluripotency stages. It would be interesting to study the interaction between OSN throughout different pluripotency stages and during cell differentiation to shed further light on mechanisms underlying the maintenance of cell identity. This could provide a target point for the manipulation of induced pluripotent stem cell cultures and cancers driven by cancer stem cells. Although we tracked TF binding through mitotic exit with an unprecedentedly high temporal resolution using ChIP-seq, it is limited to averaged time points upon cytokinesis. Thus, a complementary analysis using single-molecule imaging of TF binding in live cells would further shed light on the genome-wide binding events through mitotic exit. Two-color single-molecule imaging allows tracking of colocalization events of two different TFs and can be combined with imaging of the chromatin density (Gebhardt et al., 2013). However, if single-molecule imaging could be combined with ATAC-seq (Chen et al., 2016), it would be especially interesting to decipher if the binding of NANOG to inaccessible loci and the interaction with OS at those sites hold from our ChIP-seq and ATAC-seq analysis. Moreover, it would be interesting to study how the transient loss of either of the TFs during mitotic exit influences their interaction with the chromatin landscape. Overall, this study would be valuable in supporting our results and to further increase our understanding of the different roles of OSN in stabilizing or coordinating each other's binding to target loci.

Another interesting topic to investigate would be the interaction of OSN with the BAF complex during mitotic exit. BAF is an ATP-dependent chromatin remodeler that can remove histones, thereby opening the chromatin for the binding of TFs (King and Klose, 2017). Previously, it was demonstrated that OCT4 (King and Klose, 2017) and SOX2 (Friman et al., 2019) rely on BAF at a majority of binding sites to render the chromatin accessible. However, a subset of OCT4 binding sites was found to be BAF-independent, activated earlier during reprogramming and early during embryo differentiation (King and Klose, 2017). Thus, we could reason that during mitotic exit, OS relies less on BAF for chromatin accessibility compared to later stages during the cell cycle. It would be interesting to acquire this data to further explain the NANOG clusters and to distinguish different binding behaviors of OSN by the dependency on BAF.

## References

- Alberts, B., Johnson, A., Lewis, J., Raff, M., Roberts, K., Walter, P., 2002. *Molecular Biology of the Cell*, 4th ed. Garland Science, New York.
- Biddle, J.W., Nguyen, M., Gunawardena, J., 2019. Negative reciprocity, not ordered assembly, underlies the interaction of Sox2 and Oct4 on DNA. *Elife* 8, e41017.
- Bonhoure, N., Bounova, G., Bernasconi, D., Praz, V., Lammers, F., Canella, D., Willis, I.M., Herr, W., Hernandez, N., Delorenzi, M., Deplancke, B., Desvergne, B., Guex, N., Naef, F., Rougemont, J., Schibler, U., Andersin, T., Cousin, P., Gilardi, F., Gos, P., Raghav, S., Villeneuve, D., Fabbretti, R., Vlegel, V., Xenarios, I., Migliavacca, E., David, F., Jarosz, Y., Kuznetsov, D., Liechti, R., Martin, O., Delafontaine, J., Cajan, J., Gustafson, K., Krier, I., Leleu, M., Molina, N., Naldi, A., Rib, L., Symul, L., 2014. Quantifying ChIP-seq data: A spiking method providing an internal reference for sample-to-sample normalization. *Genome Res* 24, 1157–1168.
- Buenrostro, J.D., Giresi, P.G., Zaba, L.C., Chang, H.Y., Greenleaf, W.J., 2013. Transposition of native chromatin for fast and sensitive epigenomic profiling of open chromatin, DNA-binding proteins and nucleosome position. *Nat Methods* 10, 1213–1218.
- Buitinck, L., Louppe, G., Blondel, M., Pedregosa, F., Mueller, A., Grisel, O., Niculae, V., Prettenhofer, P., Gramfort, A., Grobler, J., Layton, R., Vanderplas, J., Joly, A., Holt, B., Varoquaux, G., 2013. API design for machine learning software: experiences from the scikit-learn project. *ArXiv* 1309.0238.
- Burke, L.J., Zhang, R., Bartkuhn, M., Tiwari, V.K., Tavoosidana, G., Kurukuti, S., Weth, C., Leers, J., Galjart, N., Ohlsson, R., Renkawitz, R., 2005. CTCF binding and higher order chromatin structure of the H19 locus are maintained in mitotic chromatin. *EMBO Journal* 24, 3291–3300.
- Caravaca, J.M., Donahue, G., Becker, J.S., He, X., Vinson, C., Zaret, K.S., 2013. Bookmarking by specific and nonspecific binding of FoxA1 pioneer factor to mitotic chromosomes. *Genes Dev* 27, 251–260.
- Carpenter, A.E., Jones, T.R., Lamprecht, M.R., Clarke, C., Kang, I.H., Friman, O., Guertin, D.A., Chang, J.H., Lindquist, R.A., Moffat, J., Golland, P., Sabatini, D.M., 2006. CellProfiler: Image analysis software for identifying and quantifying cell phenotypes. *Genome Biol* 7, R100.
- Cecchini, M.J., Amiri, M., Dick, F.A., 2012. Analysis of cell cycle position in mammalian cells. *Journal of Visualized Experiments* 3491.

- Chambers, I., Silva, J., Colby, D., Nichols, J., Nijmeijer, B., Robertson, M., Vrana, J., Jones, K., Grotewold, L., Smith, A., 2007. Nanog safeguards pluripotency and mediates germline development. *Nature* 450, 1230–1234.
- Chambers, I., Tomlinson, S.R., 2009. The transcriptional foundation of pluripotency. *Development* 136, 2311–2322.
- Chen, J., Zhang, Z., Li, L., Chen, B.C., Revyakin, A., Hajj, B., Legant, W., Dahan, M., Lionnet, T., Betzig, E., Tjian, R., Liu, Z., 2014. Single-molecule dynamics of enhanceosome assembly in embryonic stem cells. *Cell* 156, 1274–1285.
- Chen, W., Gardeux, V., Meireles-Filho, A., Deplancke, B., 2017. Profiling of Single cell transcriptome. *Curr Protoc Mouse Biol* 7, 145–175.
- Chen, X., Shen, Y., Draper, W., Buenrostro, J.D., Litzenburger, U., Cho, S.W., Satpathy, A.T., Carter, A.C., Ghosh, R.P., East-Seletsky, A., Doudna, J.A., Greenleaf, W.J., Liphardt, J.T., Chang, H.Y., 2016. ATAC-se reveals the accessible genome by transposase-mediated imaging and sequencing. *Nat Methods* 13, 1013–1020.
- Chen, X., Xu, H., Yuan, P., Fang, F., Huss, M., Vega, V.B., Wong, E., Orlov, Y.L., Zhang, W., Jiang, J., Loh, Y.H., Yeo, H.C., Yeo, Z.X., Narang, V., Govindarajan, K.R., Leong, B., Shahab, A., Ruan, Y., Bourque, G., Sung, W.K., Clarke, N.D., Wei, C.L., Ng, H.H., 2008. Integration of External Signaling Pathways with the Core Transcriptional Network in Embryonic Stem Cells. *Cell* 133, 1106–1117.
- Chervova, A., Festuccia, N., Altamirano-Pacheco, L., Dubois, A., Navarro, P., 2023. A gene subset requires CTCF bookmarking during the fast post-mitotic reactivation of mouse ES cells. *EMBO Rep* 24, e56075.
- Chickarmane, V., Troein, C., Nuber, U., Sauro, H.M., Peterson, C., 2005. Transcriptional Dynamics of the Embryonic Stem Cell Switch. *PLoS Comput Biol* 2, e123.
- Cinghu, S., Yellaboina, S., Freudenberg, J.M., Ghosh, S., Zheng, X., Oldfield, A.J., Lackford, B.L., Zaykin, D. V., Hu, G., Jothi, R., 2014. Integrative framework for identification of key cell identity genes uncovers determinants of ES cell identity and homeostasis. *Proc Natl Acad Sci U S A* 111, E1581–E1590.
- Cirillo, L.A., Lin, F.R., Cuesta, I., Friedman, D., Jarnik, M., Zaret, K.S., 2002. Opening of Compacted Chromatin by Early Developmental Transcription Factors HNF3 (FoxA) and GATA-4. *Mol Cell* 9, 279–289.
- Coronado, D., Godet, M., Bourillot, P.Y., Tapponnier, Y., Bernat, A., Petit, M., Afanassieff, M., Markossian, S., Malashicheva, A., Iacone, R., Anastassiadis, K., Savatier, P., 2013. A short G1 phase is an intrinsic determinant of naïve embryonic stem cell pluripotency. *Stem Cell Res* 10, 118–131.
- C-S Hsiung, C., Bartman, C.R., Huang, P., Ginart, P., Stonestrom, A.J., Keller, C.A., Face, C., Jahn, K.S., Evans, P., Sankaranarayanan, L., Giardine, B., Hardison, R.C., Raj, A.,

- Blobel, G.A., 2016. A hyperactive transcriptional state marks genome reactivation at the mitosis-G1 transition. *Genes Dev* 30, 1423–1439.
- Darzynkiewicz, Z., Halicka, H.D., Zhao, H., 2010. Analysis of Cellular DNA Content by Flow and Laser Scanning Cytometry. *Advances in Experimental Medicine and Biology* 676, 137–147.
- Deluz, C., Friman, E.T., Strebinger, D., Benke, A., Raccaud, M., Callegari, A., Leleu, M., Manley, S., Suter, D.M., 2016. A role for mitotic bookmarking of SOX2 in pluripotency and differentiation. *Genes Dev* 30, 2538–2550.
- Dhaliwal, N.K., Miri, K., Davidson, S., Tamim El Jarkass, H., Mitchell, J.A., 2018. KLF4 Nuclear Export Requires ERK Activation and Initiates Exit from Naive Pluripotency. *Stem Cell Reports* 10, 1308–1323.
- Dobin, A., Davis, C.A., Schlesinger, F., Drenkow, J., Zaleski, C., Jha, S., Batut, P., Chaisson, M., Gingeras, T.R., 2013. STAR: Ultrafast universal RNA-seq aligner. *Bioinformatics* 29, 15–21.
- Dull, T., Zufferey, R., Kelly, M., Mandel, R.J., Nguyen, M., Trono, D., Naldini, L., 1998. A Third-Generation Lentivirus Vector with a Conditional Packaging System. *J Virol* 72, 8463–8471.
- Dunham, I., Kundaje, A., Aldred, S.F., Collins, P.J., Davis, C.A., Doyle, F., Epstein, C.B., Frietze, S., Harrow, J., Kaul, R., Khatun, J., Lajoie, B.R., Landt, S.G., Lee, B.K., Pauli, F., Rosenbloom, K.R., Sabo, P., Safi, A., Sanyal, A., Shores, N., Simon, J.M., Song, L., Trinklein, N.D., Altshuler, R.C., Birney, E., Brown, J.B., Cheng, C., Djebali, S., Dong, X., Ernst, J., Furey, T.S., Gerstein, M., Giardine, B., Greven, M., Hardison, R.C., Harris, R.S., Herrero, J., Hoffman, M.M., Iyer, S., Kellis, M., Kheradpour, P., Lassmann, T., Li, Q., Lin, X., Marinov, G.K., Merkel, A., Mortazavi, A., Parker, S.C.J., Reddy, T.E., Rozowsky, J., Schlesinger, F., Thurman, R.E., Wang, J., Ward, L.D., Whitfield, T.W., Wilder, S.P., Wu, W., Xi, H.S., Yip, K.Y., Zhuang, J., Bernstein, B.E., Green, E.D., Gunter, C., Snyder, M., Pazin, M.J., Lowdon, R.F., Dillon, L.A.L., Adams, L.B., Kelly, C.J., Zhang, J., Wexler, J.R., Good, P.J., Feingold, E.A., Crawford, G.E., Dekker, J., Elnitski, L., Farnham, P.J., Giddings, M.C., Gingeras, T.R., Guigó, R., Hubbard, T.J., Kent, W.J., Lieb, J.D., Margulies, E.H., Myers, R.M., Stamatoyannopoulos, J.A., Tenenbaum, S.A., Weng, Z., White, K.P., Wold, B., Yu, Y., Wrobel, J., Risk, B.A., Gunawardena, H.P., Kuiper, H.C., Maier, C.W., Xie, L., Chen, X., Mikkelsen, T.S., Gillespie, S., Goren, A., Ram, O., Zhang, X., Wang, L., Issner, R., Coyne, M.J., Durham, T., Ku, M., Truong, T., Eaton, M.L., Dobin, A., Tanzer, A., Lagarde, J., Lin, W., Xue, C., Williams, B.A., Zaleski, C., Röder, M., Kokocinski, F., Abdelhamid, R.F., Alioto, T., Antoshechkin, I., Baer, M.T., Batut, P., Bell, I., Bell, K., Chakraborty, S., Chrast, J., Curado, J., Derrien, T., Drenkow, J., Dumais, E., Dumais, J., Duttagupta, R., Fastuca, M., Fejes-Toth, K., Ferreira, P., Foissac, S.,

Fullwood, M.J., Gao, H., Gonzalez, D., Gordon, A., Howald, C., Jha, S., Johnson, R., Kapranov, P., King, B., Kingswood, C., Li, G., Luo, O.J., Park, E., Preall, J.B., Presaud, K., Ribeca, P., Robyr, D., Ruan, X., Sammeth, M., Sandhu, K.S., Schaeffer, L., See, L.H., Shahab, A., Skancke, J., Suzuki, A.M., Takahashi, H., Tilgner, H., Trout, D., Walters, N., Wang, Huaien, Hayashizaki, Y., Reymond, A., Antonarakis, S.E., Hannon, G.J., Ruan, Y., Carninci, P., Sloan, C.A., Learned, K., Malladi, V.S., Wong, M.C., Barber, G.P., Cline, M.S., Dreszer, T.R., Heitner, S.G., Karolchik, D., Kirkup, V.M., Meyer, L.R., Long, J.C., Maddren, M., Raney, B.J., Grasfeder, L.L., Giresi, P.G., Battenhouse, A., Sheffield, N.C., Showers, K.A., London, D., Bhinge, A.A., Shestak, C., Schaner, M.R., Kim, S.K., Zhang, Z.Z., Mieczkowski, P.A., Mieczkowska, J.O., Liu, Z., McDaniell, R.M., Ni, Y., Rashid, N.U., Kim, M.J., Adar, S., Zhang, Zhancheng, Wang, T., Winter, D., Keefe, D., Iyer, V.R., Zheng, M., Wang, P., Gertz, J., Vielmetter, J., Partridge, E.C., Varley, K.E., Gasper, C., Bansal, A., Pepke, S., Jain, P., Amrhein, H., Bowling, K.M., Anaya, M., Cross, M.K., Muratet, M.A., Newberry, K.M., McCue, K., Nesmith, A.S., Fisher-Aylor, K.I., Pusey, B., DeSalvo, G., Parker, S.L., Balasubramanian, Sreeram, Davis, N.S., Meadows, S.K., Eggleston, T., Newberry, J.S., Levy, S.E., Absher, D.M., Wong, W.H., Blow, M.J., Visel, A., Pennachio, L.A., Petrykowska, H.M., Abyzov, A., Aken, B., Barrell, D., Barson, G., Berry, A., Bignell, A., Boychenko, V., Bussotti, G., Davidson, C., Despacio-Reyes, G., Diekhans, M., Ezkurdia, I., Frankish, A., Gilbert, J., Gonzalez, J.M., Griffiths, E., Harte, R., Hendrix, D.A., Hunt, T., Jungreis, I., Kay, M., Khurana, E., Leng, J., Lin, M.F., Loveland, J., Lu, Z., Manthravadi, D., Mariotti, M., Mudge, J., Mukherjee, G., Notredame, C., Pei, B., Rodriguez, J.M., Saunders, G., Sboner, A., Searle, S., Sisu, C., Snow, C., Steward, C., Tapanari, E., Tress, M.L., Van Baren, M.J., Washietl, S., Wilming, L., Zadissa, A., Zhang, Zhengdong, Brent, M., Haussler, D., Valencia, A., Addleman, N., Alexander, R.P., Auerbach, R.K., Balasubramanian, Suganthi, Bettinger, K., Bhardwaj, N., Boyle, A.P., Cao, A.R., Cayting, P., Charos, A., Cheng, Y., Eastman, C., Euskirchen, G., Fleming, J.D., Grubert, F., Habegger, L., Hariharan, M., Harmanci, A., Iyengar, S., Jin, V.X., Karczewski, K.J., Kasowski, M., Lacroute, P., Lam, H., Lamarre-Vincent, N., Lian, J., Lindahl-Allen, M., Min, R., Miotto, B., Monahan, H., Moqtaderi, Z., Mu, X.J., O'Geen, H., Ouyang, Z., Patacsil, D., Raha, D., Ramirez, L., Reed, B., Shi, M., Slifer, T., Witt, H., Wu, L., Xu, X., Yan, K.K., Yang, X., Struhl, K., Weissman, S.M., Penalva, L.O., Karmakar, S., Bhanvadia, R.R., Choudhury, A., Domanus, M., Ma, L., Moran, J., Victorsen, A., Auer, T., Centanin, L., Eichenlaub, M., Gruhl, F., Heermann, S., Hoekendorf, B., Inoue, D., Kellner, T., Kirchmaier, S., Mueller, C., Reinhardt, R., Schertel, L., Schneider, S., Sinn, R., Wittbrodt, B., Wittbrodt, J., Jain, G., Balasundaram, G., Bates, D.L., Byron, R., Canfield, T.K., Diegel, M.J., Dunn, D., Ebersol, A.K., Frum, T., Garg, K., Gist, E., Hansen, R.S., Boatman, L., Haugen, E., Humbert, R., Johnson, A.K.,

- Johnson, E.M., Kutayavin, T. V., Lee, K., Lotakis, D., Maurano, M.T., Neph, S.J., Neri, F. V., Nguyen, E.D., Qu, H., Reynolds, A.P., Roach, V., Rynes, E., Sanchez, M.E., Sandstrom, R.S., Shafer, A.O., Stergachis, A.B., Thomas, S., Vernot, B., Vierstra, J., Vong, S., Wang, Hao, Weaver, M.A., Yan, Y., Zhang, M., Akey, J.M., Bender, M., Dorschner, M.O., Groudine, M., MacCoss, M.J., Navas, P., Stamatoyannopoulos, G., Beal, K., Brazma, A., Flicek, P., Johnson, N., Lukk, M., Luscombe, N.M., Sobral, D., Vaquerizas, J.M., Batzoglou, S., Sidow, A., Hussami, N., Kyriazopoulou-Panagiotopoulou, S., Libbrecht, M.W., Schaub, M.A., Miller, W., Bickel, P.J., Banfai, B., Boley, N.P., Huang, H., Li, J.J., Noble, W.S., Bilmes, J.A., Buske, O.J., Sahu, A.D., Kharchenko, P. V., Park, P.J., Baker, D., Taylor, J., Lochovsky, L., 2012. An integrated encyclopedia of DNA elements in the human genome. *Nature* 489, 57–74.
- Dunn, S.J., Martello, G., Yordanov, B., Emmott, S., Smith, A.G., 2014. Defining an essential transcription factor program for naïve pluripotency. *Science* (1979) 344, 1156–1160.
- Edgar, R., Domrachev, M., Lash, A.E., 2002. Gene Expression Omnibus: NCBI gene expression and hybridization array data repository. *Nucleic Acids Res* 30, 207–210.
- Farrants, H., Tarnawski, M., Müller, T.G., Otsuka, S., Hiblot, J., Koch, B., Kueblbeck, M., Kräusslich, H.G., Ellenberg, J., Johnsson, K., 2020. Chemogenetic Control of Nanobodies. *Nat Methods* 17, 279–282.
- Festuccia, N., Dubois, A., Vandormael-Pournin, S., Gallego Tejada, E., Mouren, A., Bessonard, S., Mueller, F., Proux, C., Cohen-Tannoudji, M., Navarro, P., 2016. Mitotic binding of Esrrb marks key regulatory regions of the pluripotency network. *Nat Cell Biol* 18, 1139–1148.
- Festuccia, N., Osorno, R., Halbritter, F., Karwacki-Neisius, V., Navarro, P., Colby, D., Wong, F., Yates, A., Tomlinson, S.R., Chambers, I., 2012. Esrrb is a direct Nanog target gene that can substitute for Nanog function in pluripotent cells. *Cell Stem Cell* 11, 477–490.
- Festuccia, N., Owens, N., Papadopoulou, T., Gonzalez, I., Tachtsidi, A., Vandoermel-Pournin, S., Gallego, E., Gutierrez, N., Dubois, A., Cohen-Tannoudji, M., Navarro, P., 2019. Transcription factor activity and nucleosome organization in mitosis. *Genome Res* 29, 250–260.
- Freese, N.H., Norris, D.C., Loraine, A.E., 2016. Integrated genome browser: Visual analytics platform for genomics. *Bioinformatics* 32, 2089–2095.
- Friman, Elias T., Deluz, C., Meireles-Filho, A.C.A., Govindan, S., Gardeux, V., Deplancke, B., Suter, D.M., 2019. Dynamic regulation of chromatin accessibility by pluripotency transcription factors across the cell cycle. *Elife* 8, e50087.
- Frum, T., Halbisen, M.A., Wang, C., Amiri, H., Robson, P., Ralston, A., 2013. Oct4 Cell-autonomously promotes primitive endoderm development in the mouse blastocyst. *Dev Cell* 25, 610–622.

- Gagliardi, A., Mullin, N.P., Ying Tan, Z., Colby, D., Kousa, A.I., Halbritter, F., Weiss, J.T., Felker, A., Bezstarosti, K., Favaro, R., Demmers, J., Nicolis, S.K., Tomlinson, S.R., Poot, R.A., Chambers, I., 2013. A direct physical interaction between Nanog and Sox2 regulates embryonic stem cell self-renewal. *EMBO Journal* 32, 2231–2247.
- Gao, T., Qian, J., 2020. EnhancerAtlas 2.0: An updated resource with enhancer annotation in 586 tissue/cell types across nine species. *Nucleic Acids Res* 48, D58–D64.
- Gebhardt, J.C.M., Suter, D.M., Roy, R., Zhao, Z.W., Chapman, A.R., Basu, S., Maniatis, T., Xie, X.S., 2013. Single-molecule imaging of transcription factor binding to DNA in live mammalian cells. *Nat Methods* 10, 421–426.
- Gibcus, J.H., Samejima, K., Goloborodko, A., Samejima, I., Naumova, N., Nuebler, J., Kanemaki, M.T., Xie, L., Paulson, J.R., Earnshaw, W.C., Mirny, L.A., Dekker, J., 2018. A pathway for mitotic chromosome formation. *Science (1979)* 359, eaao6135.
- Graf, U., Casanova, E.A., Cinelli, P., 2011. The role of the leukemia inhibitory factor (LIF) - Pathway in derivation and maintenance of murine pluripotent stem cells. *Genes (Basel)*.
- Grant, C.E., Bailey, T.L., Noble, W.S., 2011. FIMO: Scanning for occurrences of a given motif. *Bioinformatics* 27, 1017–1018.
- Grosselin, K., Durand, A., Marsolier, J., Poitou, A., Marangoni, E., Nemati, F., Dahmani, A., Lameiras, S., Reyat, F., Frenoy, O., Pousse, Y., Reichen, M., Woolfe, A., Brenan, C., Griffiths, A.D., Vallot, C., Gérard, A., 2019. High-throughput single-cell ChIP-seq identifies heterogeneity of chromatin states in breast cancer. *Nat Genet* 51, 1060–1066.
- Halley-Stott, R.P., Jullien, J., Pasque, V., Gurdon, J., 2014. Mitosis Gives a Brief Window of Opportunity for a Change in Gene Transcription. *PLoS Biol* 12, e1001914.
- Heinz, S., Benner, C., Spann, N., Bertolino, E., Lin, Y.C., Laslo, P., Cheng, J.X., Murre, C., Singh, H., Glass, C.K., 2010. Simple Combinations of Lineage-Determining Transcription Factors Prime cis-Regulatory Elements Required for Macrophage and B Cell Identities. *Mol Cell* 38, 576–589.
- Heurtier, V., Owens, N., Gonzalez, I., Mueller, F., Proux, C., Mornico, D., Clerc, P., Dubois, A., Navarro, P., 2019. The molecular logic of Nanog-induced self-renewal in mouse embryonic stem cells. *Nat Commun* 10, 1109.
- Iwafuchi-Doi, M., Donahue, G., Kakumanu, A., Watts, J.A., Mahony, S., Pugh, B.F., Lee, D., Kaestner, K.H., Zaret, K.S., 2016. The Pioneer Transcription Factor FoxA Maintains an Accessible Nucleosome Configuration at Enhancers for Tissue-Specific Gene Activation. *Mol Cell* 62, 79–91.
- Jordan, M.A., Thrower, D., Wilson, L., 1992. Effects of vinblastine, podophyllotoxin and nocodazole on mitotic spindles Implications for the role of microtubule dynamics in mitosis. *J Cell Sci* 102, 401–416.



- Kadauke, S., Udugama, M.I., Pawlicki, J.M., Achtman, J.C., Jain, D.P., Cheng, Y., Hardison, R.C., Blobel, G.A., 2012b. Tissue-specific mitotic bookmarking by hematopoietic transcription factor GATA1. *Cell* 150, 725–737.
- Karwacki-Neisius, V., Göke, J., Osorno, R., Halbritter, F., Ng, J.H., Weiße, A.Y., Wong, F.C.K., Gagliardi, A., Mullin, N.P., Festuccia, N., Colby, D., Tomlinson, S.R., Ng, H.H., Chambers, I., 2013. Reduced Oct4 expression directs a robust pluripotent state with distinct signaling activity and increased enhancer occupancy by Oct4 and Nanog. *Cell Stem Cell* 12, 531–545.
- Kaya-Okur, H.S., Wu, S.J., Codomo, C.A., Pledger, E.S., Bryson, T.D., Henikoff, J.G., Ahmad, K., Henikoff, S., 2019. CUT&Tag for efficient epigenomic profiling of small samples and single cells. *Nat Commun* 10, 1930.
- Kent, W.J., Zweig, A.S., Barber, G., Hinrichs, A.S., Karolchik, D., 2010. BigWig and BigBed: Enabling browsing of large distributed datasets. *Bioinformatics* 26, 2204–2207.
- King, H.W., Klose, R.J., 2017. The pioneer factor OCT4 requires the chromatin remodeller BRG1 to support gene regulatory element function in mouse embryonic stem cells. *Elife* 6, e22631.
- Krenning, L., Sonneveld, S., Tanenbaum, M., 2022. Time-resolved single-cell sequencing identifies multiple waves of mRNA decay during the mitosis-to-G1 phase transition. *Elife* 11, e71356.
- Kunath, T., Strumpf, D., Rossant, J., 2004. Early trophoblast determination and stem cell maintenance in the mouse - A review. *Placenta* 25, S32–S38.
- Lai, X., Verhage, L., Hugouvieux, V., Zubieta, C., 2018. Pioneer factors in animals and plants—colonizing chromatin for gene regulation. *Molecules* 23, 1914.
- Lam, C.S., Mistri, T.K., Foo, Y.H., Sudhakaran, T., Gan, H.T., Rodda, D., Lim, L.H., Chou, C., Robson, P., Wohland, T., Ahmed, S., 2012. DNA-dependent Oct4-Sox2 interaction and diffusion properties characteristic of the pluripotent cell state revealed by fluorescence spectroscopy. *Biochemical Journal* 448, 21–33.
- Lee, M.T., Bonneau, A.R., Takacs, C.M., Bazzini, A.A., Divito, K.R., Fleming, E.S., Giraldez, A.J., 2013. Nanog, Pou5f1 and SoxB1 activate zygotic gene expression during the maternal-to-zygotic transition. *Nature* 503, 360–364.
- Li, H., Handsaker, B., Wysoker, A., Fennell, T., Ruan, J., Homer, N., Marth, G., Abecasis, G., Durbin, R., 2009. The Sequence Alignment/Map format and SAMtools. *Bioinformatics* 25, 2078–2079.
- Li, S., Zheng, E.B., Zhao, L., Liu, S., 2019. Nonreciprocal and Conditional Cooperativity Directs the Pioneer Activity of Pluripotency Transcription Factors. *Cell Rep* 28, 2689-2703.e4.

- Li, V.C., Ballabeni, A., Kirschner, M.W., 2012. Gap 1 phase length and mouse embryonic stem cell self-renewal. *Proc Natl Acad Sci U S A* 109, 12550–12555.
- Liao, Y., Smyth, G.K., Shi, W., 2014. FeatureCounts: An efficient general purpose program for assigning sequence reads to genomic features. *Bioinformatics* 30, 923–930.
- Liu, Y., Pelham-Webb, B., Di Giammartino, D.C., Li, J., Kim, D., Kita, K., Saiz, N., Garg, V., Doane, A., Giannakakou, P., Hadjantonakis, A.K., Elemento, O., Apostolou, E., 2017. Widespread Mitotic Bookmarking by Histone Marks and Transcription Factors in Pluripotent Stem Cells. *Cell Rep* 19, 1283–1293.
- Lundberg, A.S., Weinberg, R.A., 1998. Functional Inactivation of the Retinoblastoma Protein Requires Sequential Modification by at Least Two Distinct Cyclin-cdk Complexes. *Mol Cell Biol* 18, 753–761.
- Mallon, B.S., Chenoweth, J.G., Johnson, K.R., Hamilton, R.S., Tesar, P.J., Yavatkar, A.S., Tyson, L.J., Park, K., Chen, K.G., Fann, Y.C., McKay, R.D.G., 2013. StemCellDB: The Human Pluripotent Stem Cell Database at the National Institutes of Health. *Stem Cell Res* 10, 57–66.
- Martin, R.M., Cardoso, M.C., 2010. Chromatin condensation modulates access and binding of nuclear proteins. *The FASEB Journal* 24, 1066–1072.
- Masui, S., Nakatake, Y., Toyooka, Y., Shimosato, D., Yagi, R., Takahashi, K., Okochi, H., Okuda, A., Matoba, R., Sharov, A.A., Ko, M.S.H., Niwa, H., 2007. Pluripotency governed by Sox2 via regulation of Oct3/4 expression in mouse embryonic stem cells. *Nat Cell Biol* 9, 625–635.
- Matsui, Y., Nakayama, Y., Okamoto, M., Fukumoto, Y., Yamaguchi, N., 2012. Enrichment of cell populations in metaphase, anaphase, and telophase by synchronization using nocodazole and blebbistatin: A novel method suitable for examining dynamic changes in proteins during mitotic progression. *Eur J Cell Biol* 91, 413–419.
- Mayran, A., Drouin, J., 2018. Pioneer transcription factors shape the epigenetic landscape. *Journal of Biological Chemistry* 293, 13795–13804.
- Michael, A.K., Grand, R.S., Isbel, L., Cavadini, S., Kozicka, Z., Kempf, G., Bunker, R.D., Schenk, A.D., Graff-Meyer, A., Pathare, G.R., Weiss, J., Matsumoto, S., Burger, L., Schübeler, D., Thomä, N.H., 2020. Mechanisms of OCT4-SOX2 motif readout on nucleosomes. *Science (1979)* 368, 1460–1465.
- Mistri, T.K., Kelly, D., Mak, J., Colby, D., Mullin, N., Chambers, I., Mistri, T.K., 2022. Single molecular binding dynamics of Nanog with Sox2 and Oct4 Analysis of pluripotency transcription factor interactions reveals preferential binding of NANOG to SOX2 rather than NANOG or OCT4. *bioRxiv* 2020.06.24.169185.

- Moretto-Zita, M., Jin, H., Shen, Z., Zhao, T., Briggs, S.P., Xu, Y., 2010. Phosphorylation stabilizes Nanog by promoting its interaction with Pin1. *Proc Natl Acad Sci U S A* 107, 13312–13317.
- Moshe, A., Kaplan, T., 2017. Genome-wide search for Zelda-like chromatin signatures identifies GAF as a pioneer factor in early fly development. *Epigenetics Chromatin* 10, 33.
- Neph, S., Kuehn, M.S., Reynolds, A.P., Haugen, E., Thurman, R.E., Johnson, A.K., Rynes, E., Maurano, M.T., Vierstra, J., Thomas, S., Sandstrom, R., Humbert, R., Stamatoyannopoulos, J.A., 2012. BEDOPS: High-performance genomic feature operations. *Bioinformatics* 28, 1919–1920.
- Nishimura, K., Fukagawa, T., Takisawa, H., Kakimoto, T., Kanemaki, M., 2009. An auxin-based degron system for the rapid depletion of proteins in nonplant cells. *Nat Methods* 6, 917–922.
- Nishitani, H., Sugimoto, N., Roukos, V., Nakanishi, Y., Saijo, M., Obuse, C., Tsurimoto, T., Nakayama, K.I., Nakayama, K., Fujita, M., Lygerou, Z., Nishimoto, T., 2006. Two E3 ubiquitin ligases, SCF-Skp2 and DDB1-Cul4, target human Cdt1 for proteolysis. *EMBO Journal* 25, 1126–1136.
- Niwa, H., Miyazaki, J.-I., Smith, A.G., 2000. Quantitative expression of Oct-3/4 defines differentiation, dedifferentiation or self-renewal of ES cells. *Nat Genet* 24, 372–376.
- Oh, E., Mark, K.G., Mocchiari, A., Watson, E.R., Prabu, J.R., Cha, D.D., Kampmann, M., Gamarra, N., Zhou, C.Y., Rape, M., 2020. Gene expression and cell identity controlled by anaphase-promoting complex. *Nature* 579, 136–140.
- Ohtsuka, S., Nakai-Futatsugi, Y., Niwa, H., 2015. LIF signal in mouse embryonic stem cells. *JAKSTAT* 4, e1086520.
- Orlando, D.A., Chen, M.W., Brown, V.E., Solanki, S., Choi, Y.J., Olson, E.R., Fritz, C.C., Bradner, J.E., Guenther, M.G., 2014. Quantitative ChIP-Seq normalization reveals global modulation of the epigenome. *Cell Rep* 9, 1163–1170.
- Owens, N., Papadopoulou, T., Festuccia, N., Tachtsidi, A., Gonzalez, I., Dubois, A., Vandormael-Pournin, S., Nora, P., Bruneau, B.G., Cohen-Tannoudji, M., Navarro, P., 2019. CTCF confers local nucleosome resiliency after DNA replication and during mitosis. *Elife* 8, e47898.
- Palozola, K.C., Donahue, G., Liu, H., Grant, G.R., Becker, J.S., Cote, A., Yu, H., Raj, A., Zaret, K.S., 2017. Mitotic transcription and waves of gene reactivation during mitotic exit. *Science (1979)* 358, 119–122.
- Pauklin, S., Vallier, L., 2013. The cell-cycle state of stem cells determines cell fate propensity. *Cell* 155, 135–147.

- Pelham-Webb, B., Polyzos, A., Wojenski, L., Kloetgen, A., Li, J., Di Giammartino, D.C., Sakellaropoulos, T., Tsirigos, A., Core, L., Apostolou, E., 2021. H3K27ac bookmarking promotes rapid post-mitotic activation of the pluripotent stem cell program without impacting 3D chromatin reorganization. *Mol Cell* 81, 1732-1748.e8.
- Phillips, N.E., Mandic, A., Omid, S., Naef, F., Suter, D.M., 2019. Memory and relatedness of transcriptional activity in mammalian cell lineages. *Nat Commun* 10, 1208.
- Qi, D., Wang, Q., Yu, M., Lan, R., Li, S., Lu, F., 2016. Mitotic phosphorylation of SOX2 mediated by Aurora kinase A is critical for the stem-cell like cell maintenance in PA-1 cells. *Cell Cycle* 15, 2009–2018.
- Quinlan, A.R., Hall, I.M., 2010. BEDTools: A flexible suite of utilities for comparing genomic features. *Bioinformatics* 26, 841–842.
- Raccaud, M., Friman, E.T., Alber, A.B., Agarwal, H., Deluz, C., Kuhn, T., Gebhardt, J.C.M., Suter, D.M., 2019. Mitotic chromosome binding predicts transcription factor properties in interphase. *Nat Commun* 10, 487.
- Raccaud, M., Suter, D.M., 2018. Transcription factor retention on mitotic chromosomes: regulatory mechanisms and impact on cell fate decisions. *FEBS Lett* 592, 878–887.
- Ramírez, F., Ryan, D.P., Grüning, B., Bhardwaj, V., Kilpert, F., Richter, A.S., Heyne, S., Dündar, F., Manke, T., 2016. deepTools2: a next generation web server for deep-sequencing data analysis. *Nucleic Acids Res* 44, W160–W165.
- Rizkallah, R., Alexander, K.E., Hurt, M.M., 2011. Global mitotic phosphorylation of C2H2 zinc finger protein linker peptides. *Cell Cycle* 10, 3327–3336.
- Robinson, M.D., McCarthy, D.J., Smyth, G.K., 2009. edgeR: A Bioconductor package for differential expression analysis of digital gene expression data. *Bioinformatics* 26, 139–140.
- Robinson, M.D., Oshlack, A., 2010. A scaling normalization method for differential expression analysis of RNA-seq data. *Genome Biol* 11, R25.
- Roccio, M., Schmitter, D., Knobloch, M., Okawa, Y., Sage, D., Lutolf, M.P., 2013. Predicting stem cell fate changes by differential cell cycle progression patterns. *Development (Cambridge)* 140, 459–470.
- Rodda, D.J., Chew, J.L., Lim, L.H., Loh, Y.H., Wang, B., Ng, H.H., Robson, P., 2005. Transcriptional regulation of Nanog by OCT4 and SOX2. *Journal of Biological Chemistry* 280, 24731–24737.
- Sakaue-Sawano, A., Kurokawa, H., Morimura, T., Hanyu, A., Hama, H., Osawa, H., Kashiwagi, S., Fukami, K., Miyata, T., Miyoshi, H., Imamura, T., Ogawa, M., Masai, H., Miyawaki, A., 2008. Visualizing Spatiotemporal Dynamics of Multicellular Cell-Cycle Progression. *Cell* 132, 487–498.

- Sakaue-Sawano, A., Yo, M., Komatsu, N., Hiratsuka, T., Kogure, T., Hoshida, T., Goshima, N., Matsuda, M., Miyoshi, H., Miyawaki, A., 2017. Genetically Encoded Tools for Optical Dissection of the Mammalian Cell Cycle. *Mol Cell* 68, 626-640.e5.
- Sandelin, A., Alkema, W., Engström, P., Wasserman, W.W., Lenhard, B., 2004. JASPAR: An open-access database for eukaryotic transcription factor binding profiles. *Nucleic Acids Res* 32, D91–D94.
- Sarnataro, S., Riba, A., Molina, N., 2021. Regulation of transcription reactivation dynamics exiting mitosis. *PLoS Comput Biol* 17, e1009354.
- Savatie P, Huang S, Szekely L, Wiman KG, Samarut J, 1994. Contrasting patterns of retinoblastoma protein expression in mouse embryonic stem cells and embryonic fibroblasts. *Oncogene* 9, 809–818.
- Schindelin, J., Arganda-Carreras, I., Frise, E., Kaynig, V., Longair, M., Pietzsch, T., Preibisch, S., Rueden, C., Saalfeld, S., Schmid, B., Tinevez, J.Y., White, D.J., Hartenstein, V., Eliceiri, K., Tomancak, P., Cardona, A., 2012. Fiji: An open-source platform for biological-image analysis. *Nat Methods* 9, 676–682.
- Schraivogel, D., Kuhn, T.M., Rauscher, B., Rodríguez-Martínez, M., Paulsen, M., Owsley, K., Middlebrook, A., Tischer, C., Ramasz, B., Ordoñez-Rueda, D., Dees, M., Cuylen-Haering, S., Diebold, E., Steinmetz, L.M., 2022. High-speed fluorescence image-enabled cell sorting. *Science (1979)* 375, 315–320.
- Shahbazi, M.N., 2020. Mechanisms of human embryo development: From cell fate to tissue shape and back. *Development (Cambridge)* 147, dev190629.
- Shin, J., Wan Kim, T., Kim, H., Ji Kim, H., Young Suh, M., Lee, S., Lee, H.-T., Kwak, S., Lee, S.-E., Lee, J.-H., Jang, H., Cho, E.-J., Youn, H.-D., 2016. Aurkb/PP1-mediated resetting of Oct4 during the cell cycle determines the identity of embryonic stem cells. *Elife* 5, e10877.
- Shlyueva, D., Teed-Singer, S., Zhan, Y., Koche, R., Helin, K., 2022. An integrated approach to study chromatin and transcriptional dynamics throughout the cell cycle without pharmacological inhibition. *bioRxiv* 2022.06.18.496661.
- Skene, P.J., Henikoff, S., 2017. An efficient targeted nuclease strategy for high-resolution mapping of DNA binding sites. *Elife* 6, e21856-resolution mapping of DNA binding sites.
- Soufi, A., Donahue, G., Zaret, K.S., 2012. Facilitators and impediments of the pluripotency reprogramming factors' initial engagement with the genome. *Cell* 151, 994–1004.
- Soufi, A., Garcia, M.F., Jaroszewicz, A., Osman, N., Pellegrini, M., Zaret, K.S., 2015. Pioneer transcription factors target partial DNA motifs on nucleosomes to initiate reprogramming. *Cell* 161, 555–568.
- Stark, R., Brown, G., 2011. DiffBind: Differential binding analysis of ChIP-Seq peak data, Bioconductor.

- Strebinger, D., Deluz, C., Friman, E.T., Govindan, S., Alber, A.B., Suter, D.M., 2019. Endogenous fluctuations of OCT 4 and SOX 2 bias pluripotent cell fate decisions . *Mol Syst Biol* 15, e9002.
- Suter, D.M., Cartier, L., Bettiol, E., Tirefort, D., Jaconi, M.E., Dubois-Dauphin, M., Krause, K.-H., 2006. Rapid Generation of Stable Transgenic Embryonic Stem Cell Lines Using Modular Lentivectors. *Stem Cells* 24, 615–623.
- Takahashi, K., Yamanaka, S., 2006. Induction of Pluripotent Stem Cells from Mouse Embryonic and Adult Fibroblast Cultures by Defined Factors. *Cell* 126, 663–676.
- Takahashi, S., Kobayashi, S., Hiratani, I., 2018. Epigenetic differences between naïve and primed pluripotent stem cells. *Cellular and Molecular Life Sciences* 75, 1191–1203.
- ter Huurne, M., Chappell, J., Dalton, S., Stunnenberg, H.G., 2017. Distinct Cell-Cycle Control in Two Different States of Mouse Pluripotency. *Cell Stem Cell* 21, 449-455.e4.
- Teves, S.S., An, L., Bhargava-Shah, A., Xie, L., Darzacq, X., Tjian, R., 2018. A stable mode of bookmarking by TBP recruits RNA polymerase II to mitotic chromosomes. *Elife* 7, e35621.
- Thompson, J.J., Lee, D.J., Mitra, A., Frail, S., Dale, R.K., Rocha, P.P., 2022. Extensive co-binding and rapid redistribution of NANOG and GATA6 during emergence of divergent lineages. *Nat Commun* 13, 4257.
- Thomson, M., Liu, S.J., Zou, L.N., Smith, Z., Meissner, A., Ramanathan, S., 2011. Pluripotency factors in embryonic stem cells regulate differentiation into germ layers. *Cell* 145, 875–889.
- Tremble, K.C., Stirparo, G.G., Bates, L.E., Maskalenka, K., Stuart, H.T., Jones, K., Andersson-Rolf, A., Radzishchanskaya, A., Koo, B.K., Bertone, P., Silva, J.C.R., 2021. Sox2 modulation increases naïve pluripotency plasticity. *iScience* 24, 102153.
- Trouillas, M., Saucourt, C., Guillotin, B., Gauthereau, X., Ding, L., Buchholz, F., Doss, M.X., Sachinidis, A., Hescheler, J., Hummel, O., Huebner, N., Kolde, R., Vilo, J., Schulz, H., Bœuf, H., 2009. Three LIF-dependent signatures and gene clusters with atypical expression profiles, identified by transcriptome studies in mouse ES cells and early derivatives. *BMC Genomics* 10, 73.
- Vagnarelli, P., 2012. Mitotic chromosome condensation in vertebrates. *Exp Cell Res* 318, 1435–1441.
- Wamaitha, S.E., Del Valle, I., Cho, L.T.Y., Wei, Y., Fogarty, N.M.E., Blakeley, P., Sherwood, R.I., Ji, H., Niakan, K.K., 2015. Gata6 potently initiates reprogramming of pluripotent and differentiated cells to extraembryonic endoderm stem cells. *Genes Dev* 29, 1239–1255.
- Wang, R., Liang, J., Jiang, H., Qin, L.J., Yang, H.T., 2008. Promoter-dependent enhanced green fluorescent protein expression during embryonic stem cell propagation and differentiation. *Stem Cells Dev* 17, 279–289.

- Weinberg, R.A., 1995. The Retinoblastoma Protein and Cell Cycle Control Review. *Cell* 81, 323–330.
- Wen, D.L., Yang, Q., Tong CHEN, J., Zhou, H., Ming LIU, R., Tai HUANG, X., 2005. Dynamic distribution of Ser-10 phosphorylated histone H3 in cytoplasm of MCF-7 and CHO cells during mitosis. *Cell Res* 15, 120–126.
- Wickham, H., 2016. *ggplot2: Elegant Graphics for Data Analysis*, ggplot2. Springer New York.
- Wu, T., Hu, E., Xu, S., Chen, M., Guo, P., Dai, Z., Feng, T., Zhou, L., Tang, W., Zhan, L., Fu, X., Liu, S., Bo, X., Yu, G., 2021. clusterProfiler 4.0: A universal enrichment tool for interpreting omics data. *Innovation* 2, 100141.
- Xing, H., Vanderford, N.L., Sarge, K.D., 2008. The TBP-PP2A mitotic complex bookmarks genes by preventing condensin action. *Nat Cell Biol* 10, 1318–1323.
- Yu, G., Wang, L.G., Han, Y., He, Q.Y., 2012. ClusterProfiler: An R package for comparing biological themes among gene clusters. *OMICS* 16, 284–287.
- Zaret, K.S., Carroll, J.S., 2011. Pioneer transcription factors: Establishing competence for gene expression. *Genes Dev* 25, 2227–2241.
- Zaveri, L., Dhawan, J., 2018. Cycling to meet fate: Connecting pluripotency to the cell cycle. *Front Cell Dev Biol* 6, 57.
- Zhang, H., Emerson, D.J., Gilgenast, T.G., Titus, K.R., Lan, Y., Huang, P., Zhang, D., Wang, H., Keller, C.A., Giardine, B., Hardison, R.C., Phillips-Cremins, J.E., Blobel, G.A., 2019. Chromatin structure dynamics during the mitosis-to-G1 phase transition. *Nature* 576, 158–162.
- Zhang, Y., Liu, T., Meyer, C.A., Eeckhoute, J., Johnson, D.S., Bernstein, B.E., Nussbaum, C., Myers, R.M., Brown, M., Li, W., Shirley, X.S., 2008. Model-based analysis of ChIP-Seq (MACS). *Genome Biol* 9, R137.
- Zhou, Z., He, M., Shah, A.A., Wan, Y., 2016. Insights into APC/C: From cellular function to diseases and therapeutics. *Cell Div* 11, 9.

# Curriculum vitae – Silja Placzek

**Molecular Biologist | Bioinformatician**

## CONTACT INFORMATION

---

silja.placzek@gmx.de    ☎ +41767214356    📍 Avenue du Galicien 7, 1008 Prilly (CH)

## PERSONAL DETAILS

---

Date of Birth: 28.01.1995

Nationality: German

## EXPERIENCE

---

### Doctoral thesis in Life Sciences

Institute of Bioengineering, École Polytechnique Fédérale de Lausanne, Switzerland

📅 April 2019 – September 2023 (Full-time)

Laboratory of gene regulation and cell identity led by Prof. David M. Suter

---

### Teaching assistant

Institute of Bioengineering, École Polytechnique Fédérale de Lausanne, Switzerland

📅 September 2020 – July 2021

I taught bachelor students how to conduct experiments and helped with their exercises in the courses integrated laboratory in life sciences I and II, cellular and molecular biology I, immunology.

---

### Teaching assistant

Interfaculty Institute for Cell Biology, University of Tübingen, Germany

📅 January 2017; December 2015 – January 2016 (Part-time)

Assisting bachelor students in biology with their experiments for the course molecular cell biology I.

---

## EDUCATION

---

### Doctoral thesis in Life Sciences

Institute of Bioengineering, École Polytechnique Fédérale de Lausanne, Switzerland

📅 April 2019 – September 2023

In the lab of Prof. David Suter, I studied the molecular events leading to the global restoration of the chromatin landscape during mitotic exit in mouse embryonic stem cells.

---



## Master thesis

Institute for Molecular Health Sciences, Eidgenössische Technische Hochschule Zürich, Switzerland

📅 January 2018 – July 2018

In the lab of Prof. Gerald Schwank, I studied adult stem cell-derived organoid cultures in defined hydrogels.

---

## Master of Molecular Cell Biology and Immunology

Interfaculty Institute for Cell Biology, University of Tübingen, Germany

📅 October 2016 – July 2018

In addition to the general courses, I specialized on parasitology and oncology.

---

## Bachelor of Biology

University of Tübingen, Germany

📅 October 2013 – August 2016

In the lab of Prof. Günther Muth, I studied the role of type IV-like secretion systems during the conjugative DNA transfer of *Streptomyces lividans*.

---

## SKILLS

---

**Experimental skills:** genomics (ChIP-, ATAC-, nucRNA-seq, CUT&RUN), qPCR, time-lapse imaging (wide-field microscopy), lentiviral transduction, transfection, molecular cloning, flow cytometry, mammalian cell culture (HEK cells, mESCs, organoid cultures), immunofluorescence, CRISPR-Cas9 knock-in

---

**Computational skills:** Image processing (Fiji, CellProfiler), analysis of my own omics datasets using cluster computing, R, Python, UNIX/Bash, Office suite

---

## PUBLICATIONS

---

Broguiere, N; Isenmann, L; Hirt, C; Ringel, T; Placzek, S; et al. (2018) Growth of epithelial organoids in a defined hydrogel. *Adv. Mater.* 1801621: 1-12.

---

## CONFERENCES

---

### Gordon Research Conference

Chromatin Structure and Function, Barcelona, Spain

📅 Mai 2022 (Poster presentation)

---

## **Bioengineering Day**

Institute of Bioengineering, École Polytechnique Fédérale de Lausanne, Switzerland

 Mai 2022 (Poster presentation)

## **SCHOLARSHIP**

---

### **Partial scholarship PROMOS for study abroad**

German Academic Exchange Service (DAAD)


 January 2018 – July 2018

## **VOLUNTEERING**

---

### **Fundraising manager**

Association of Doctoral Students in Life Sciences, École Polytechnique Fédérale de Lausanne, Switzerland


 June 2019 – May 2022

Finding sponsors for events that are planned from the PhD students of this association for PhD students in life sciences at EPFL.

---

### **Snowboard teacher**


TG Biberach, Biberach an der Riß, Germany

 January 2011 – January 2012

---

### **Holiday carer**

Paradiesle, Biberach an der Riß, Germany

 August 2010 – August 2012

---

## **LANGUAGES**

---

German: Mother tongue

English: Fluent C2

French: Intermediate B1

Spanish: Elementary A2

## **HOBBIES**

---

(Snowshoe) Hiking, bouldering, cycling, running, swimming, cooking